Development of Cryogenic Semiconductor Microcalorimeters for Spectroscopic x-ray Astronomy

James H Rochford, BSc

PhD thesis

Mullard Space Science Laboratory
University College London

2002

ProQuest Number: 10011310

All rights reserved

INFORMATION TO ALL USERS
The quality of this reproduction is dependent upon the quality of the copy submitted.

In the unlikely event that the author did not send a complete manuscript
and there are missing pages, these will be noted. Also, if material had to be removed,
a note will indicate the deletion.

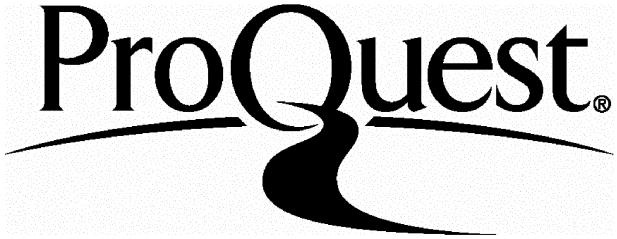

ProQuest 10011310

Published by ProQuest LLC(2016). Copyright of the Dissertation is held by the Author.

All rights reserved.
This work is protected against unauthorized copying under Title 17, United States Code.
Microform Edition © ProQuest LLC.

ProQuest LLC
789 East Eisenhower Parkway
P.O. Box 1346
Ann Arbor, MI 48106-1346

To my mother Ellen and all my family
for their encouragement and support
and in memory of my father Thomas.

Abstract

This thesis assesses the feasibility of using Neutron Transmutation Doped Germanium (NTD Ge) as the thermistor element of a microcalorimeter that has the potential to be used to create a very large high spectral resolution x-ray imaging array. A number of numerical simulations of a single microcalorimeter system have been created. These models are capable of estimating the overall system performance of the complete microcalorimeter system. The models include the non-ideal effects incurred by the system bandwidth, non-linearity of the detector response during an x-ray event, the electric field across the detector and electron-phonon decoupling. The inclusion of these effects accounts for the observed poor performance of current experimental NTD Ge detectors. The model predictions have been experimentally verified down to 50mK. The models predict that an energy resolution comparable to that required by future spectroscopic arrays can be achieved using a small highly doped NTD Ge thermistor operating at 10mK. The construction of new thermal link schemes for individual detectors that simplify the creation of an array is investigated. It is shown that it is potentially feasible to use the boundary resistance of the thermistor bonded directly to the heat sink as a thermal link. Two novel array readout methods are presented; both of these significantly reduce the number of channels required to readout an array. One scheme uses diodes to constrain the voltage pulses produces by a pixel to remain in its own row and column of the array. The second scheme uses two thermistors to readout each pixel, this is shown to greatly reduce the number of wires into the array itself, thus reducing the thermal load to levels compatible with future space borne adiabatic demagnetisation refrigerators. It is shown that these detectors can be formed into moderately sized arrays. It is ultimately concluded that the construction of very large arrays using these particular detectors may prove impractical due to their monolithic nature.

CONTENTS

List of Figures and Tables

1 X-ray astronomy

1.1 Introduction

In this chapter x-ray astronomy, x-ray detectors and x-ray microcalorimetery, are reviewed to place the thesis within its wider context.

1.2 x-ray astronomy

The development of x-ray microcalorimetery is ultimately driven by the needs of the observational x-ray astronomers. This section reviews the history of x-ray astronomy, its future requirements and its relationship to x-ray microcalorimeters. Detailed reviews can be found in references [1,2,3].

1.2.1 History of x ray astronomy

X-ray astronomy is by necessity a space based observational discipline as x-rays are absorbed by the earth's atmosphere. For this reason, it did not begin until the advent of rockets powerful enough to lift the required instrumentation into orbit. The first identified celestial source SCO-X1 was discovered on a sounding rocket experiment in June 1962. By the end of the sixties ~400 x-ray sources had been detected in further sounding rocket experiments. The low fluxes from astronomical sources, the limited collection time on sounding rocket experiments (typically 5 minutes) and the small collecting areas of the initial limited the size of the x-ray source population.

This changed in the 1970's with the advent of dedicated x-ray observing satellites. The first such observatory was UHURU launched in 1970. The extended observation time improved the mission sensitivity to lower source fluxes. Following UHURU the next major advance in x-ray astronomy commenced with the launch of the EINSTEIN Observatory. This observatory used a focusing x-ray telescope, which greatly improved the collection efficiency increasing the signal to noise ratio and giving the observatory a factor of 100 improvement in sensitivity over previous missions. After the EINSTEIN mission several thousand x-ray sources had been catalogued and precisely located. These were associated with many classes of astronomical objects

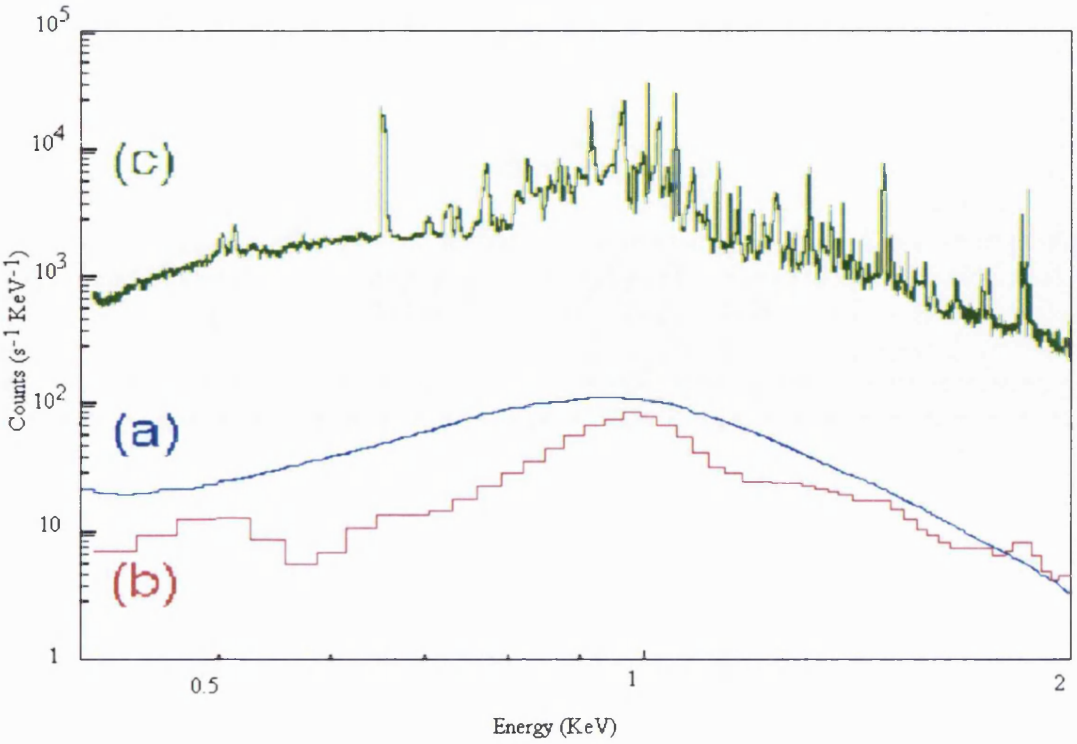

Figure 1.1 Simulations showing the comparative energy resolution achieved with older type, non cryogenic, x-ray spectrometers currently used in x-ray astronomy when viewing a ~10^7K plasma. (a) a proportional counter, (b) a CCD detector and (c) a grating spectrometer. Note the plots are not normalized to the same total count (Adapted from [3]).

Following the EINSTEIN mission, there has been a series of x-ray observatories. The Roentgen Satellite (ROSAT), which ended its mission on 12 February 1999[4], was the first x-ray and XUV all-sky survey using an imaging telescope with x-ray sensitivity. It had about 1000 times greater sensitivity than UHURU and has catalogued $1.5x10^4$ x-ray sources. The Advanced Satellite for Cosmology and Astrophysics (ASCA)[5] satellite was launched in Feb 1993 and was operational until July 2000. Notably it measured x-rays which are thought to come from close to the event horizons of super massive black holes. ASCA was the first mission to use x-ray Charge Coupled Detector arrays (CCD) capable of providing x-ray spectrographic imaging. The resolution of CCD's (~100eV over the 0.4-10keV band) was a considerable improvement over proportional counter detectors used on preivous x-ray missions: a comparison of the spectral detail obtained from these devices is shown in figure 1.1 and compared to the fine spectral detail obtainable from a grating.

Mirror Characteristic	Einstein	EXOSAT	ROSAT	BBXRT ASCA	Newton	Chandra	Astro E XRS
Aperture Diameter	58 cm	28 cm	83 cm	40 cm 1 module	70 cm 1 module	1.2 m	400mm
Mirrors	4 nested 1 module	2 nested	4 nested	118 nested 1 module	58 nested	4 nested	168 nested
Geometric area (mm^2)	350	80	1140	1400	6000	1100	88700
Grazing angle (arcmin)	40-70	90-110	83-135	21-45	18-40	27-51	0.19-0.63
Focal length (m)	3.45	1.09	2.4	3.8	7.5	10	4.5
Mirror coating	Ni	Au	Au	Au	Au	Ir	Pt
Highest energy focused (keV)	5	2	2	12	10	10	12
On axis resolution (arcsec)	4	18	4	75	20	0.5	~1.5

Table 1.1Comparison of the mirror characteristics of past and present x-ray missions (Adapted from [6]).

Since ASCA three major x-ray missions have been developed. All of these have been launched; the Japanese mission Astro-E was launched in Feb 2000 unfortunately the mission failed during launch and the satellite was lost. A re-flight of the mission is currently been planned called Astro-E2 with an expected launch date in 2005. The European X-ray Multi Mirror XMM [7] telescope was launched in Dec 1999 and renamed the Newton Observatory after launch it is currently operational. The NASA mission Chandra[8] was launched in July 1999 and is also operational. All these missions are characterised by greatly improved x-ray optics, as seen in table 1.1, they allow for an unparalleled spatial resolution, which is coupled to greatly improved throughputs because of the larger collecting areas of the x-ray telescopes. All these observatories have x-ray CCD arrays capable of similar imaging spectroscopy to the ASCA array. But with a larger throughput and improved angular resolution they will be capable of gathering tens of thousands more x-ray spectra than ASCA and are thus able to reach much fainter source populations.

For high-resolution spectroscopy the Newton observatory and Chandra use gratings, this method is dispersive and needs a high x-ray flux to work, because of this they can only obtain spectra from the brighter sources. In additional problem with gratings is they are intrinsically

non-imaging. Of the three missions only Astro–E had a high resolution imaging spectrometer which consisted of an array of Semiconductor Microcalorimeters (SM). These had a 10eV resolution and would have allowed Astro–E to perform limited spectroscopy on extended x-ray sources and obtain spectra from fainter objects than Newton observatory or Chandra. The 10eV resolution, which would have been available on Astro-E, is a great improvement on previous detectors, but would still be insufficient to provide detailed spectroscopy of the kind available with grating spectrometers. In future, a resolution comparable to that of a grating will be required to allow many of essential line complexes observed in astronomical spectra to be fully resolved. Additionally it needs to be in an array format to allow the study of extended x-ray emitting objects. The microcalorimeter array on Astro-E, although of limited size (6x6 elements), may be seen as a precursor of these future spectroscopic arrays.

1.2.2 The future for x-ray astronomy

It is clear that there have been major advances in x-ray astronomy. In the 1960's the original missions merely catalogued x-ray sources. With today's observatories it is beginning to mature into a fully fledged observational science, capable of performing extensive source diagnostics. The current missions still have limitations and a new generation of orbiting x-ray telescopes will soon be developed which will take x-ray astronomy well into the 21st century. These observatories will allow the detailed physics of the large source populations so far discovered to be fully investigated. They will also allow new fainter source populations to be accessed and transform the study of all x-ray emitting objects e.g. supernovae remnants, Active Galactic Nuclei (AGN), accretion disks. In short they will provide large scientific returns in most areas of astronomy [1,2,3].

1.2.2.1 Advancing x-ray astronomy

X-ray astronomy has become an increasingly important tool, comparable with optical or radio astronomy. It is recognised an essential means of addressing some of the unresolved issues in astronomy. The following paragraph of this section will highlight some of these.

Accretion disks are created near gravitational potential wells formed by large gravitational sources, where orbiting matter falls into the well it forms a disk. As it spirals through the disk in it releases gravitational potential energy and heats up the material in the disk to high temperatures emitting x-rays. They release gravitational energy so efficiently they are 10

times more efficient than nuclear burning. Accretion disks are now recognised to occur in many astrophysical settings. Ranging over mass scales from

- Accretion disks which coalesce to form planetary systems.
- Binary stars containing a compact companion star which is accreting material from its neighbour e.g. Cataclysmic Variable (CV) stars.
- Active Galactic Nuclei (AGN) in which super massive black holes in the centre of a galaxy devours in falling material in the central region of the galaxy.

The general principles of these systems are reasonably well understood however, some of the underlying physics observed within these phenomena is still not clear. For example, the mechanism for generating the radio jets commonly associated within AGN and the role, which magnetic fields play in this, still needs to be resolved. Because these systems are large extended, hot x-ray emitting, objects imaging x-ray spectroscopy will play a central role in uncovering the true nature of these mechanisms.

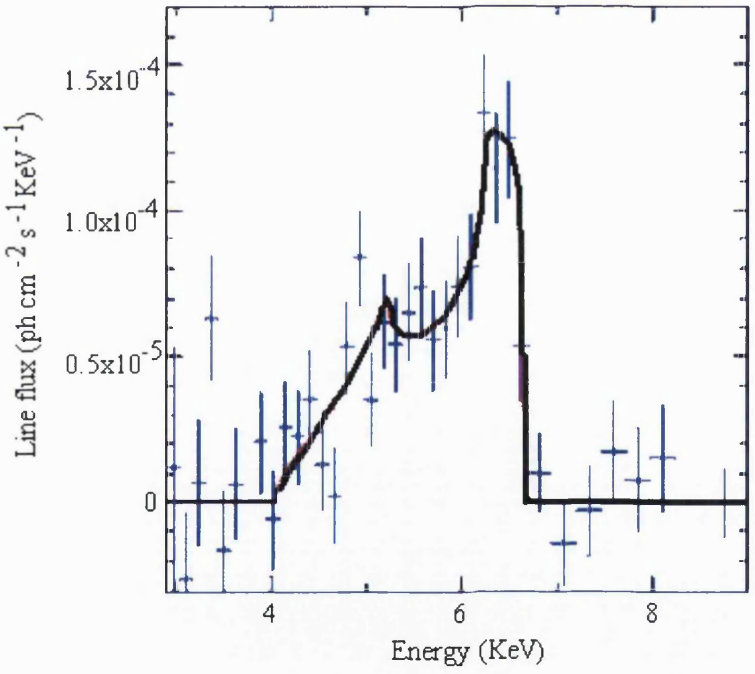

Figure 1.2 A very broad, asymmetric iron line profile, seen in a long ASCA observation of the Seyfert galaxy MCG-6-30-15. The solid line is a model of fluorescent emission from an accretion disk around a non-rotating black hole. (Taken from [2]).

Since the basic physical principles of all accretion disks should be similar, it will be possible to use a high throughput imaging spectrometer to study similar nearby systems within our own galaxy, such as CV and other x-ray binaries. By resolving line features from the

accretion disk and by measuring the continuum shape over a broad energy band in these systems it will be possible to study accretion disk physics in greater detail. For example the ASCA satellite detected relativistically broadened iron Kα emission lines from an AGN (see figure 1.2). In an AGN, x-ray emission arises from close to the event horizon of a black hole where the disk material is hottest. The strong gravitational fields in this region distort these spectral features, consequently they can be used to probe the space-time geometry close to the black hole and the nature of the material surrounding the black hole. In fact, this is the only observational method currently capable of determining black hole spin. By measuring these characteristics for many sources on future missions, a statistical picture will eventually be developed which will allow the study of chemical evolution in AGN over time. In addition, it will be possible to determine the distribution of black hole masses and spins as functions of time. Such studies are central to determining the evolutionary processes within AGN and clarifying the links between high-luminosity quasars and lower-luminosity Seyfert Galaxies.

The x-ray satellite ROSAT has previously resolved ~80% of the x-ray background at 1keV into discrete sources. Many were found to be AGN with a mean redshift of 1.5 and some have been detected out to redshifts as high as 4. The x-ray band above a few keV is effectively immune to absorption which allows AGN to be detected to high redshifts. In contrast to optical observations of AGN populations, which show a population peak at redshifts of 2-3, the corresponding current x-ray observations show no evidence for such a decline in numbers at higher redshifts. This needs to be confirmed by future missions, which will sample a greater number of AGN by accessing these higher red shift populations. These observations will be important since they tell us how AGN evolve and how structure on galactic scales evolved. Understanding these processes will also help us to answer questions on the nature of the connection between super massive black holes and their host galaxies.

Another problem in modern cosmology is to assess the amount of matter in the universe. Observations of the Lyman-α forest at large redshifts show that most of the predicted baryon content of the Universe is in the Inter-Galactic Medium (IGM). Similar observations show that the baryon content of stars, neutral hydrogen, and x-ray emitting cluster gas in the local Universe is ~ 10 times less than expected. This is confirmed by numerical simulations, which simulate the formation and evolution of structure in the universe. These predict that this 'missing' local material should reside as gas in the IGM with a temperature range of 10^5-10^7K. This material has not been detected locally and its existence needs to be confirmed. Gas at temperatures >10^5K will be highly ionised, making it impossible to detect absorption lines in the optical or ultraviolet bands. It should be possible to detect x-ray features from this

material, which will become imprinted on spectra of background objects (such as quasars). This would provide a powerful diagnostic tool to investigate the nature of the IGM.

It is largely accepted that the hot x-ray emitting gas dominates the baryonic content of galaxy clusters. Measurements on this gas are an invaluable tool to trace the overall mass content, including dark matter within the gravitational potential well of the cluster. The presence of emission lines from highly ionised elements particularly iron and oxygen, within this gas can be used to study global nucleosynthesis over time. Ultimately, such a study will clarify how nuclear processing during stellar evolution is fed into the IGM and Intra Cluster Medium (ICM) by supernovae. These emission features can also be used to determine the internal velocity dynamics of gas clouds, galaxies, IGM and the ICM with high precision. Thus a study of the x-ray emission from hot gas can be used to investigate galaxy collisions and mergers, supernova remnants and investigate the supply of enriched material from supernovae to the InterStellar Medium (ISM) the ICM and IGM. In short, we can examine the connection of matter on a wide range of scales over time, using x-rays.

The problems presented above are a small selection of the topics which future x-ray missions can help to address. A central tool to help resolve the above problems is the provision of a large 2-D x-ray imaging spectrometer. Such an instrument will need to provide high resolution spectral imaging of extended x-ray emitting objects. The resolution needs to be capable of resolving most of the important line complexes in the 1-12KeV region, many of the interesting atomic transitions occur in this energy range. Currently only x-ray gratings and crystal spectrometers can provide such resolutions, but these are intrinsically wasteful, using only a portion of the incident flux and are non-imaging. Future arrays will need to use the low flux levels from astronomic x-ray objects more efficiently, reducing the observational time required to obtain spectra; thus serving the x-ray astronomy community more efficiently.

1.2.3 Planned x ray missions

In the coming years there are at two new major missions planned to follow up on the progress that is currently being made in x-ray astronomy. These are the NASA Constellation-X proposal and ESA XEUS proposal. A prime goal of all these missions will be high resolution imaging spectroscopy. To achieve this the latter two of these missions will have to use undemonstrated new detector technologies since current detectors are not yet capable of providing a high spectral resolution in a large array format. Two of these missions; XEUS and Constellation-X are in an advanced stage of conception.

1.2.3.1 XEUS

XEUS is the European Space Agency proposal to provide a permanent orbital facility capable of addressing the future requirements of x-ray astronomers. XEUS is planned to consist of two separate spacecraft. The Mirror SpaceCraft (MSC) which will contain the x-ray mirrors and the Detector SpaceCraft (DSC) which contains the focal plane instrumentation. Both spacecraft will be deployed together and maintain a fixed separation of 50m. This distance is defined by the focal length required for the mirror system. After ~4 years both spacecraft will dock with the International Space Station for refurbishment and to add more mirror area to the MSC increasing the collecting area to ~30m^2 at 1keV. At this point, the focal plane detectors will also be renewed with the current technology of the period. The initial launch of the mission is planned for ~2010 and is expected to have an active life of ~20 years. The planned specification for the mission is shown in table 1.2.

PARAMETER	SPECIFICATION(GOAL)
Energy Range	0.05-30 (0.05-100)keV
Telescope Focal Length	50m
Mirror Effective Collecting Area (phase 1)	@ 1keV= 6 m^2
(phase 2)	@ 1keV =30 m^2
Mirror Effective Collecting Area (phase 1)	@ 8keV =3 m^2
(phase 2)	@ 8keV =3 m^2
Spatial Resolution (HEW)	@ 1keV = 2″
Field Of View	5-10′
Energy resolution (Narrow field detectors)	@ 8keV = 10eV
	@1keV = 1-2eV
Energy resolution (Wide field detectors)	@ 8keV= 110eV
	@1keV = 40-50eV
Limiting Sensitivity (phase 1)	3x10^{-24} J cm^{-2}s^{-1}
Limiting Sensitivity (phase 2)	4x10^{-25} J cm-^{2}s^{-1}

Table 1.2The basic design goals of The XEUS Observatory (Adapted from [9]).

The prime objective of the XEUS mission is high resolution spectroscopy over the 1-30keV range. Within this range the Narrow Field camera Instrument (NFI) is envisioned to carry out imaging spectroscopy in the 1-12keV range. The detectors for this instrument are planned to be a Cryogenic Imaging Spectrometer array (CIS). The elements of this array have not yet

been specified, but two technologies have been identified as promising. These are Superconducting Tunnel Junctions (STJ) and Semiconductor Microcalorimeters (SM) and are dealt with in more detail in section 1.3 and chapter 2 respectively. The baseline requirements of the CIS array are that it is to have a resolution of 1-10eV over a range of 1-10keV. The number of pixels required in the array is a minimum of (30x30) but with a goal of (100x100) pixels being set.

The pixel size is defined by the optics resolution. From table 1.2 the spatial resolution is given as 2″. The plate scale for a 50m focal length is ~4″/mm. To adequately sample the spatial resolution would require say 5 pixels, this gives an angular resolution of 0.4″ that translates to a pixel size of 100μm^2 in the focal plane. This gives a good idea of the expected size required for the pixels in future arrays.

1.2.3.2 Constellation X

Constellation-X is a NASA concept to advance x-ray astronomy early this century and is part of their long term x-ray astronomy program. Whilst ESA's XEUS uses a large telescope with a long focal length to provide the necessary collecting area to perform high throughput imaging spectroscopy. NASA has chosen a different approach and is planning to fly six smaller co-aligned telescopes in unison, which will give a larger effective area. As with XEUS, high throughput spectroscopy is central to the mission.

PARAMETER	SPECIFICATION
Energy Range	1-12keV
Telescope Focal Length	8m
Mirror Effective Collecting Area	@ 1keV= 1.5 m^2
	@ 6.4keV= 0.6 m^2
Spatial Resolution (HPD)	@ 1keV = 15″
Field Of View	2.5-10′
Energy resolution	0.3- 8keV = 1-2eV
Limiting Sensitivity	5x10^{-22} J cm^{-2}s^{-1}

Table 1.3 The High Throughput x-ray Spectrometer (Compiled from [10])

The planned specification of Constellation-X mission is shown in table 1.3. NASA has currently identified Transition Edge Sensors (TES) as being the best candidate detectors for

the planned High Throughput X-ray Spectrometer (HTXS) instrument on Constellation X [11]. However, they are pursuing a two track strategy, developing TES and SM (these are dealt with in more detail in section 1.3 and chapter 2) in a hope to identify the most fruitful technology. The expected improvement in resolution, of the HTXS instrument over the XRS array that was going to be used on Astro-E is shown in figure 1.3. The detectors have a technical specification similar to those for the XEUS NFI detectors, but will have a larger nominal size to accommodate the larger blur radius of Constellation-X.

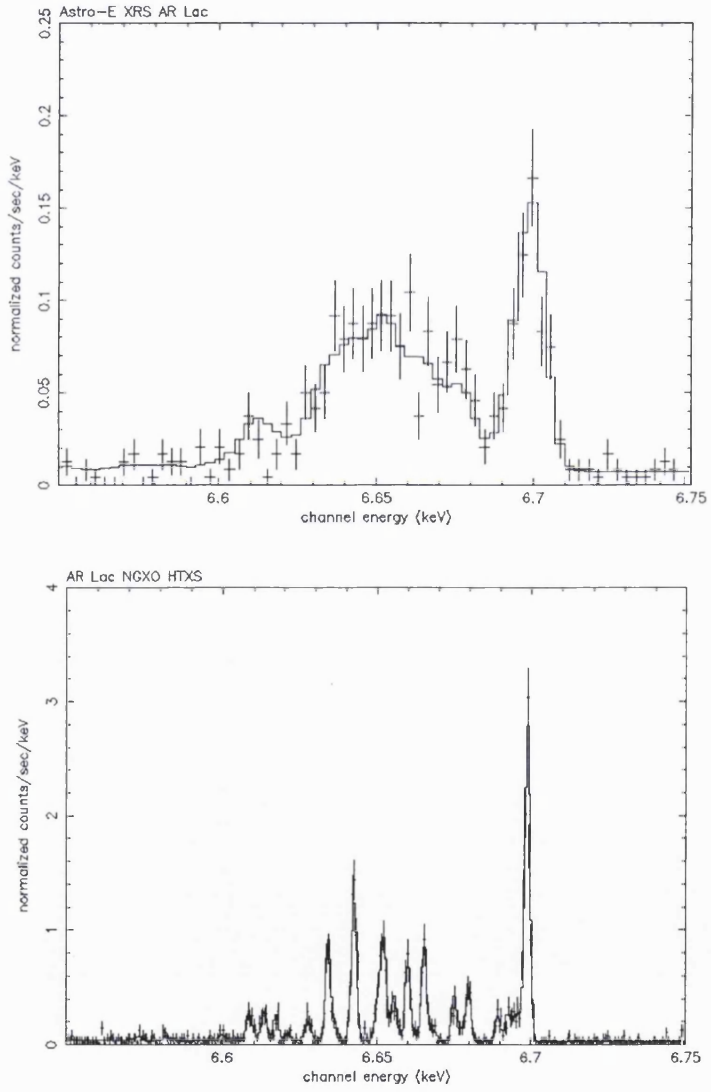

Figure 1.3. A simulation of the performance of the Astro-E XRS (upper) and the Constellation-X HTXS (lower). It shows how the HTXS will allow satellite lines of Iron to be fully resolved. (Adapted from [12])

1.2.4 X-ray microcalorimetery

Future x-ray missions are likely to require large arrays of imaging x-ray spectrometers, having up to 100x100 pixels, with each pixel typically 100-200μm^2 and an energy resolution of 1 to 8eV in the 1-12keV range. None of the x-ray detectors used to date, e.g. crystal spectrometers, CCD and proportional counters are capable of simultaneously satisfying all the criteria necessary to perform, high sensitivity, high resolution, x-ray imaging spectroscopy in an array. One way to create these arrays is to couple x-ray microcalorimeters together. X-ray microcalorimeters are detectors, which are capable of detecting individual x-rays with an energy resolution of a few electron volts. This is achieved by sensing the thermal energy produced by the absorption of a x-ray in matter and converting it into an analysable signal.

Physically a microcalorimeter may be created by employing different kinds of device to act as a thermistor: one method is to use a semiconductor as the thermistor creating a SM. As semiconductors are cooled below 1K, their resistance becomes a strong function of temperature. By setting a constant current through the semiconductor, the voltage signal produced across it is proportional to the temperature of the crystal, and hence the energy of an absorbed x-ray.

Research into x-ray microcalorimetery was largely developed in the early 1980's. An American collaboration between the Goddard Space Flight Center (GSFC) and the University of Wisconsin. They published a paper[13] suggesting it was possible to use a silicon based SM, to detect single x-ray photons, with unparalleled spectral accuracy, when operating at low temperatures. They showed that theoretically such a device would be limited only by thermodynamic fluctuations within it. In the same paper they proposed the design of an actual device and calculated that when operating at 0.1K it would yield an energy resolution of less than 1eV when detecting 6keV x-rays. Later that year they demonstrated the use of an antimony doped silicon thermistor capable of detecting 6keV x-rays with a resolution of 270eV at a temperature of 300mK[14]. This was comparable with theoretical estimates for the device, which estimated the resolution as 170eV at 300mK. This work was followed up in later years with a series of papers detailing their progress[15,16]. In more recent papers[17,18], they describe the development and operation of a 36 element experimental array of silicon microcalorimeters, which have an energy resolution of 7-8eV in the 1-6keV x-ray region when operating at 60mK. The array was flown successfully on a sounding rocket payload to observe the diffuse x-ray background in the energy band 0.1-1keV in 1996 [19]. They used the expertise acquired in creating the first array to create another 36 element array. This was to be

used in the x-ray spectrometer instrument to be flown on the ill-fated Japanese Astro-E mission (see figure 5.5 in section 5.3). It is planned to use this array format on the re-flight mission Astro-E2.

Since the GSFC program started, other groups have begun carrying out similar work to develop microcalorimeters. One of the most notable is the group at the Lawrence Livermore National Laboratory (LLNL). They demonstrated a resolution of 70eV at 300mK using a NTD Ge microcalorimeter[20] and developed a broad band, high resolution, x-ray microcalorimeter that has a resolution of 23eV over an energy range of 0.5-7keV[21] when operated at 80mK. Notably, they have recently collaborated with the National Institute of Standards and Technology (NIST), to pioneer the development of TES running in extreme electrothermal feedback mode. These devices are also microcalorimeters, but use the rapidly changing resistance within the superconducting to normal transition of a super conductor to detect absorbed photons. These are described in section 1.3.2.

1.2.4.1 MSSL detector programme

The x-ray detector program at MSSL began in collaboration with Queen Mary and Westfield College (QMW), University of London around 1987. It stemmed from research at QMW into infrared bolometers. Historically QMW have extensive experience in this area. They were responsible for the development of a large 2-D array using Neutron Transmutation Doped (NTD) Ge bolometers for the Sub millimetre Common User Bolometer Array (SCUBA) instrument. SCUBA is an infrared/submillimetre detection system that is in operation at the James Clerk Maxwell Telescope, on Mauna Kea in Hawaii [64]. At the time the collaboration began, MSSL was keen to develop new x-ray detector technologies.

The collaboration concentrated on extending the use of NTD Ge as the thermistor element of a SM. NTD Ge is a bulk doped semiconductor produced by irradiating a block of Ge in a uniform beam of neutrons. Because NTD Ge is bulk doped, it has a uniform doping profile, which gives it a superior noise performance to semiconductors created using other techniques.

The main emphasis of the group was to look at single pixel devices, which were easy to fabricate and could be assembled into larger 2-D arrays. This built on the expertise and knowledge of the SCUBA instrument. For SCUBA the modularity of the device was seen as

an advantage, if a pixel became damaged it could be replaced without having to replace the whole array.

The initial results of the group proved promising. Using an NTD Ge microcalorimeter [22] operating at a temperature 340mK, a raw RMS energy resolution of 286eV was demonstrated. After processing the results using a matched filter technique, a resolution of 149eV was obtained. The theoretical RMS resolution of the device at this temperature was estimated to be 123eV. A year later using a similar but smaller device[23] (the heat capacity was reduced by a magnitude) operating at the same temperature, they demonstrated a RMS energy resolution of 75eV detecting 5.57-5.9keV x-rays. The theoretical RMS resolution was estimated to be 41eV at this temperature. Higher resolutions were expected by operating these devices at lower temperatures. However following the initial detector experiments, the group found it problematic to achieve resolutions close to the predicted theoretical values. The work presented in this thesis was primarily intended to address this problem and ultimately pursue the creation of a small, high resolution prototype array.

1.3 Other future x-ray spectrometer detectors

SM are not the only technology capable of meeting the requirements for future spectroscopic x-ray arrays. At present, there are two other types of detector technologies being developed, which can also theoretically satisfy the requirements; STJ and TES. SM are dealt with in the next chapter in some detail. The others are briefly reviewed in the following sections.

1.3.1 Superconducting tunnel junctions

STJ come in many different varieties but the basic device is as shown schematically in figure 1.4. It consists of two superconducting layers separated by a thin insulating barrier, typically ~20μm thick. If an x-ray is absorbed in any one of the superconducting layers, or any layer connected to them, it will generate high energy phonons. These phonons will relax in a cascade process, breaking Cooper pairs in the physically connected electrode into quasiparticles. These quasiparticles may recombine and re-emit phonons in the process.

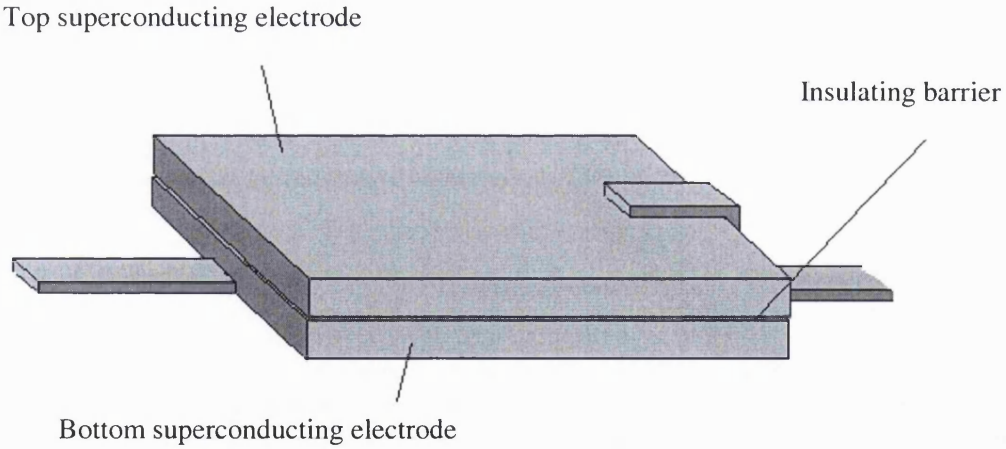

Figure 1.4Schematic of STJ detector with attached readout contacts.

The interaction between the phonons and Cooper pairs continues until the typical energy of the cascade drops below ε_c, the energy of an isolated Cooper pair. The consequence of this process is that during a x-ray event a temporary excess of quasiparticles is generated. There is a quantum mechanical probability that these quasiparticles will tunnel across the insulating layer into the second conducting electrode. The width of the barrier, its area and the number density of quasiparticles, dictate the tunnelling probability. By applying a bias voltage across

the device, the tunnelled charge produces an observable current pulse, which can be detected with a charge amplifier. The amount of detected charge is proportional to the quasiparticle density; hence, the energy of the incident x-rays. A schematic showing typical tunnelling processes across an STJ are shown in figure 1.5.

The high resolution obtainable by STJ detectors arises because they rely on the detection of quasiparticles. The energy ε to create a quasiparticle is of the order of meV. If an absorbed x-ray of energy E generates a number N of quasiparticles then the resolution in the detected energy ΔE created by random variations in the numbers of quasiparticles produced is given by Poisson statistics as $\Delta E = \sqrt{(E.\varepsilon)}$. This is a simplified picture, Poisson statistics is not an adequate description of the process, and an additional factor called the Fano factor F, needs to be included [25]. This changes the predicted R.M.S resolution to $\Delta E = \sqrt{F.(E.\varepsilon)}$. In terms of full width half maximum this is given as $\Delta E_{FWHM} = 2(\sqrt{2Ln(2)})\sqrt{F.(E.\varepsilon)}$. For Nb, ε is 2.64meV and F is 0.22. So for the detection of a 6keV x-ray in a Nb based STJ a resolution of ΔE_{FWHM}=4eV is expected.

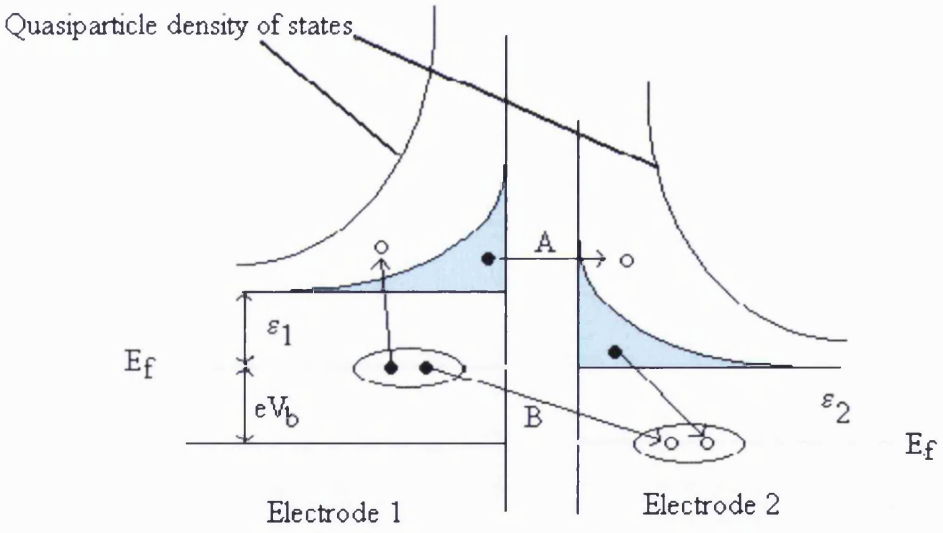

Figure 1.5 The major tunnelling processes in an STJ. In process A, tunnelling by a quasiparticle from an occupied state in electrode 1, to an unoccupied state in electrode 2. Process B a Cooper pair absorbs an energy > ε_1 and liberates a quasiparticle to an empty state in electrode 1, whilst its partner tunnels to recombine in electrode 2. V_b is the applied bias voltage across the electrodes, which shifts the normal energies between the electrodes by an amount eV_b. (Taken from [24])

The development of STJ detectors as x-ray detectors began in the mid 1980s [25]. STJ detectors had an advantage over SM, they did not require the low sub 100mK operational temperatures, required by SM, whilst offering a comparable energy resolution. The

operational temperature, of a STJ must be well below the super conducting transition temperature. Typically these devices are operated in the 100mK to 1K temperature range.

STJ detectors manufactured to date have not achieved their Fano limited resolution because of additional loss mechanisms, which generate variability in the number of quasiparticles. The main mechanisms are:

- Both phonons and quasiparticles will diffuse out of the detection electrode, during a detection event.
- Phonons are lost to the process as the mean phonon energy drops below the energy required to liberate quasiparticles.
- Quasi particles can become trapped at spatial inhomogeneities such as defects and impurity sites.
- Quasi particles are continually recombining to create phonons.
- Variations in the insulation barrier properties affect the tunnelling rates.

Each of these loss processes has associated with it a statistical noise which adds to the overall noise of the device. Such variations have been estimated to contribute 10-20eV[26] degradation in the device resolution.

Methods have been devised to limit the effects of these loss processes. The most notable method is that of quasiparticle trapping [27]. Quasi particle trapping effectively holds the quasiparticles close to the barrier region preventing them from escaping during the detection process. This is achieved by the addition of an extra layer of superconductor material which had a lower band-gap, ε', than the outer electrode, between it and the tunnel layer. This causes the quasiparticles generated by the cascade process to degrade to a typical energy ε' defined by the band gap on the inner electrode. They are then confined in the potential well created within the inner layer; thus minimising loss of quasiparticles from the tunnelling process. This scheme has improved the resolution of STJ but it has still not proved possible to achieve the Fano limited resolution. The typical resolutions so far obtained with STJ detectors for medium x-rays are 29eV for 5.89keV [28]. Research indicates that a large part of the remaining degradation in resolution may be due to quasiparticle loss at the detector edges and loss into the connecting superconducting leads [29]. More recent work has achieved energy resolutions of 12ev for 5.89KeV x-rays by introducing a metallic buffer layer under the electrode[77].

STJ detectors also suffer from poor quantum efficiency for energetic x-rays of more than a few keV. The superconductors used for STJ have low atomic numbers, which makes them poor x-ray absorbers. It is not possible to offset this by increasing the thickness of the superconducting layer, because this is found to degrade the tunnelling efficiency, resulting in an overall degradation in performance. The chief method to circumvent this problem has been to attach an absorber with a higher atomic mass to the STJ. The absorber can stop the x-rays efficiently, whilst the STJ acts as a thermistor of the phonon population in the absorber [30]. To conclude, STJ detectors have shown much promise but have not thus far been able to replicate the experimentally demonstrated resolutions of SM and TES.

1.3.2 Superconducting Transition Edge Sensors

TES, like SM are composite detectors. They use an absorber to thermalise incident x-rays in their phonon population. The absorber is thermally coupled to a transition edge sense element. This sensor consists of a layer of superconductor held within its normal superconducting transition region. Within this region, the resistance is a very strong function of temperature. Typically, the rate of change of resistance with temperature over the transition, is an order magnitude greater than that of typical semiconductor sensors giving an inherently higher resolution. TES, like semiconductor detectors, require low temperature operation to minimise noise (see section 2.21) and maximise their thermodynamic responsivity by minimising the heat capacity. This limits the materials and operational temperatures that can be used by TES since there are only five superconducting elements with transitions below 500mK. This limitation has been overcome by using the proximity effect to create the TES sensors. The proximity effect occurs when a superconductor and normal metal are in contact this causes the transition temperature of the composite to drop below that of the elemental superconductor [31]. In addition to having a low transition temperature, other desirable features of a good transition edge for a microcalorimeter sensor are a steep linear transition, which is wide enough to accommodate all x-rays of interest. A drawback is that all of these effects are modified by the presence of impurities in the sensor. So the deposition of ultra high purity thin films is required in order to create good transitions reproducibly.

Before 1996, readout of TES was performed using constant current biasing, in a manner similar to SM. In the constant current scheme, the bias current I_b must be applied so that the TES operating temperature T_e sits just at the base of its transition region. In this mode the TES is inherently unstable; if it detects an x-ray the temperature increases by dT causing the sensor to increase its resistance to R(Te+dT). This increases the joule heating in the detector,

which in turn pushes the resistance up further, eventually driving the device normal. This effect is seen above certain level of bias current termed the latching current. TES were initially readout using used warm Junction Field Effect Transistors (JFET) pre-amplifiers in the same manner as SM. However utilising the low impedance of the transition edge, the Munich dark matter group proved it was possible to use low noise DC Superconducting QUantum Interference Detectors (SQUID) to readout TES [32,33]. SQUID are solid state devices created using a small superconducting inductance in parallel to one or more Josephson junctions; these devices can be used as very sensitive magnetometers by coupling the superconducting inductance to a pick up loop. The method of using SQUID to readout TES is shown in figure 1.6(a). A constant bias current I_b is passed into the circuit. Any change in the transition edge resistance will result in a change in the branching current I_a. The resulting change in I_a is readout via an inductance coupled to the input inductance of a SQUID.

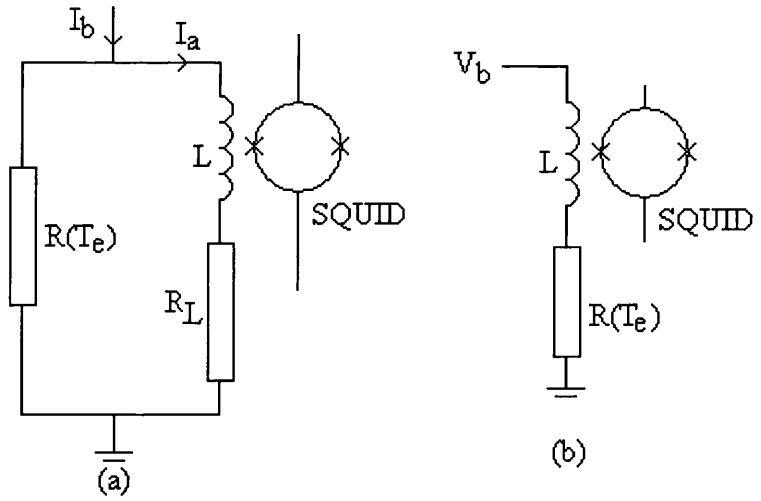

Figure 1.6 (a) Constant current bias scheme. R_L reference resistance, L Inductance coupled to SQUID input impedance. $R(T_e)$ resistance of Transition edge sensor at T_e within transition. I_b constant current, I_a branching current. (b) V_b constant voltage bias.

The use of SQUID with TES has additional benefits;

- They are very low noise devices with a low input impedance this makes the whole system relatively insensitive to microphonic pickup.
- They need much less operational power (~2μW) than conventional JFET(~5mW).
- SQUID can be operated at sub 4K temperatures closer to the detector making large arrays much easier to create. JFET need to be operated at temperatures of 70 – 140K on an independent temperature stage, greatly increasing the readout complexity, for large arrays

.

A favourable readout method has been developed for TES. This method utilises a constant voltage bias scheme along with high levels of electrothermal feedback [34] to maintain the device stability within the transition region. The scheme is shown in figure 1.6 (b). Here electrothermal feedback is applied by an external power source, which supplies a constant voltage that holds the detector at some fixed voltage V_b. The substrate is then cooled to a temperature T below the transition temperature of the superconducting edge T_c. As the TES cools through the transition, its resistance drops and consequently the bias power increases via $(V_b)^2/R(T)$. The result is that the device comes to a stable equilibrium temperature T_e within the transition. Effectively the device self biases itself. This method has advantages over the other schemes; it is inherently stable and forces the TES to respond faster than is possible from the thermal response alone. If an x-ray is detected it heats the absorber attached to the sensor, the sensor resistance rises, thereby reducing the bias power and forcing the device to cool more rapidly. With $T \ll T_c$ it is found that the reduction in bias power is approximately equivalent to the energy of the x-ray detected. Hence, by monitoring the bias current via a SQUID, the energy of the event can be recorded. This is given by the integral of the resultant current pulse times the bias voltage V_b. The effective time constant of the TES when biased in this manner is found to be 100 times less than the intrinsic thermal time constant of the device [35].

The fundamental thermodynamic resolution of TES when compared to a comparable SM is increased by approximately a magnitude, making it possible to use a normal metal absorber with these detectors. Although normal metal absorbers have high heat capacities they suffer from very little thermalisation noise and are thus preferred to other materials (see section 2.2.2). To date, these detectors have proved to be very efficient. Recently, resolutions of 7.2eV ± 0.4eV FWHM for 5.89keV x-rays [36] and 3.1eV ± 0.1eV FWHM over the energy range 0 - 2keV [37] have been reported. A further advantage is it should be relatively easy to create large arrays of TES because of their thin film nature, which should lend itself to standard photolithographic techniques.

2 Semiconductor Microcalorimeters

2.1 Introduction

This chapter addresses the background and theory necessary to understand and describe the behaviour of a SM operating at low temperatures. The object is to provide a basis for the development of a model that is capable of predicting the final resolution of a microcalorimeter system subject to all potential degrading effects. The construction of such a model is described in chapter 3.

In the following chapter, it is shown that ideally a microcalorimeter resolution should only be limited by the thermodynamic fluctuations within it. The dependence of the thermistor resistance on doping level and temperature is derived in a qualitative fashion. Ideal bolometer theory is presented. It is shown that the resolution predicted cannot be realised because of additional non-ideal effects.

2.2 Semiconductor Microcalorimeters

A SM is a composite device that incorporates an absorber (to thermalise x-rays) bonded to a semiconductor thermistor (which detects the temperature change induced by the absorption of the x-ray). In order to obtain a high resolution the resistance of the semiconductor, R(T), needs to be a strong function of temperature. For semiconductors at low temperatures the resistance is given by

$$R(T) = R_o.EXP\left(\sqrt{\left(\frac{T_g}{T}\right)}\right) \qquad \text{- 2.1}$$

where R_o, and T_g are constants, dependent on the level and nature of doping in the crystal. When operating in a bias circuit, as shown in figure 2.1, the bulk heat capacity C(T) of the microcalorimeter at a temperature T is thermally linked via a conductance $G(T-T_o)$ to a heat sink at T_o. In equilibrium the temperature difference $(T-T_o)$ is maintained by a constant bias current I_b, which dissipates a power $I_b^2R(T)$ in the detector. The absorption of an x-ray in the absorber raises the temperature of the detector by some amount ΔT resulting in a change in voltage the across the detector given by $R(\Delta T)I_b$. This makes the amplitude of the voltage pulse proportional to the energy of the absorbed x-ray.

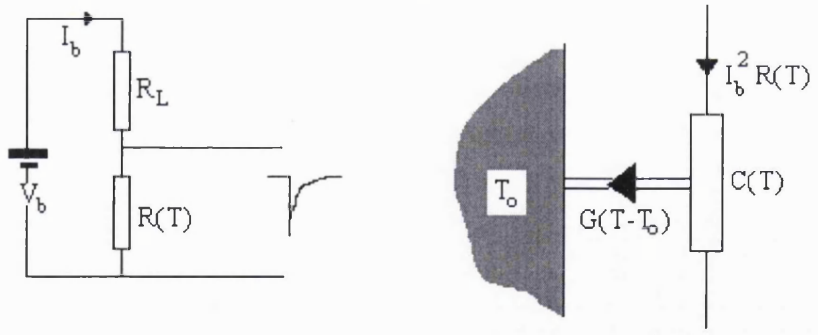

Figure 2.1 A Schematic of the electrical and thermal circuits of a microcalorimeter. Electrically: The detector resistance R(T) is biased with a constant bias current I_b. A constant current approximation is ensured by having $R_L>>R(T)$ using a bias voltage V_b. Thermally: the heat capacity C(T) of the detector operating at a temperature T is linked via the conductance $G(T-T_o)$ to a heat sink at temperature T_o.

2.2.1 Fundamental detector resolution

For any ideal microcalorimeter including SM, the ability to determine a temperature change is limited only by the random thermal variations within it. The magnitude of these variations may be calculated from pure thermodynamic considerations, knowing nothing of the specific microscopic nature of the detector, the method of proving this is dealt with in most statistical thermodynamic texts[76].

Consider the detector as an isolated system, consisting of a large number N of independent particles, with individual energies ε_i in thermal equilibrium at some temperature T. Irrespective of the nature of the particles within this system, from the partition function, the mean energy $\bar{\varepsilon}$ is given by

$$\bar{\varepsilon} = \frac{\sum_{i=0}^{i=N} \varepsilon_i \, \mathrm{Exp}(-\beta\varepsilon_i)}{\sum_{i=0}^{i=N} \mathrm{Exp}(-\beta\varepsilon_i)} \qquad \text{- 2.2}$$

where $\beta=(1/K_BT)$. Taking the partial derivative of the mean energy with respect to β gives

$$\frac{\partial\bar{\varepsilon}}{\partial\beta} = \bar{\varepsilon}^2 - \overline{\varepsilon^2} = \Delta E^2 \qquad \text{- 2.3}$$

By inspection, this is the mean squared variation ΔE^2 in energy about some mean $\bar{\varepsilon}$. However, from a classical macroscopic thermodynamic standpoint the heat capacity of any system is given by

$$C = \frac{\partial\bar{\varepsilon}}{\partial T} = \frac{\partial\bar{\varepsilon}}{\partial\beta}\left(-\frac{1}{K_B T^2}\right) \qquad \text{- 2.4}$$

Using equations 2.3 and 2.4 and taking the square root we obtain the relationship of the microscopic fluctuations in energy ΔE to the macroscopic heat capacity of the system

$$\Delta E = T\sqrt{K_B C} \qquad \text{- 2.5}$$

This implies that for an ideal isolated device in equilibrium, the temperature cannot be measured more accurately than the magnitude of these fluctuations.

This is an idealised case, for a real microcalorimeter, two additional effects must be accounted for. The detector is not a thermally isolated system but connected by a thermal link to a heat sink at T_o. Additionally there are extra noise sources arising from Johnson noise in the thermometer resistance R(T). An inclusion of these effects [13] gives the resolution of an ideal microcalorimeter as

$$\Delta E = \xi T\sqrt{K_B C} \qquad \text{- 2.6}$$

The multiplying factor ξ is a constant for a detector at a fixed temperature and is inversely related to the responsivity of the resistance to temperature, dR/dT. Typically for SM operating in an optimal temperature range, it may be shown that $\xi \approx 2$ [13,75,76]. However using a thermistor other than a semiconductor, with higher responsivity, it is possible to achieve an energy resolution closer to the ideal thermodynamic limit of an isolated system as given in equation 2.5.

Equation 2.6 shows that the resolution of an microcalorimeter is not dependent on the conductivity $G(T-T_o)$ to the heat sink. The implication of this is that there is no penalty for having a slow or fast detector. However, it is shown in section 3.3, when the detector is integrated in its biasing system the speed of the detector is integrally related to the overall system resolution. Equation 2.6 also tells us that the resolution of the detector varies with the square root of the heat capacity. Typically, the heat capacity of the detector may be given by

$$C(T) = A\left[\frac{T}{T_D}\right]^3 + BT \qquad \text{- 2.7}$$

The first term accounts for the specific heat of crystal lattice. T_D is the material's Debye temperature and A is a constant. The second term is due to the contribution from the

electronic gas where B is the electron coefficient. At low temperatures, the electrons are frozen out and the heat capacity is dominated by the lattice component. The implications of equations 2.6 and 2.7 are the heat capacity must be minimised and the detector operated at as low a temperature as possible to achieve the maximum resolution.

2.2.2 Selection of x-ray Absorbers

A key spectral region of interest in spectroscopic x-ray astronomy is from 1 to 12keV encompassing many of the interesting atomic x-ray transitions. At these energies, x-ray absorption in matter occurs predominately by the photoelectric effect. When a x-ray hits an atom in the lattice of the detector, it will cause the atom to recoil violently. Consequently, about 70% of the incident energy creates high frequency ballistic phonons, which degrade to become thermal phonons. The remaining 30% liberates a photoelectron. Electrons in outer shells of the atom will fill the vacancy left by the photoelectron in radiative transitions. The photoelectron and photons released by the x-ray event will cause further ionisation's in the same and/or neighbouring atoms. Eventually by continual interactions with the lattice, the electron-hole pairs degrade, depositing their energy in thermal phonons. Almost all of the energy (~ 99%) may be degraded into phonons and ends up as heat in the detector volume. Because of this early x-ray SM consisted of just the semiconductor. It was hoped that it would be possible to thermalise the x-ray in the semiconductor volume itself. This was not the case and these early microcalorimeters suffered from incomplete thermalisation and additional thermalisation noise.

Experimental work to investigate the reasons for the thermalisation noise was carried out at the GSFC. They found that the thermalisation noise was caused by the trapping of electron hole pairs on unoccupied donor sites for periods longer than the thermalisation time [1] (typically ns). This removed them from the thermalisation process during the x-ray event. Because of this, the quantum efficiency of the detector is decreased. A variation in the number of electrons trapped between each x-ray event creates the additional thermalisation noise. The work at the GSFC found the only effective solution to the inefficient thermalisation within the semiconductor was to bond the semiconductor to a material that was an efficient x-ray absorber.

The GSFC group examined many different types of material as potential absorbers [38]. They grouped the absorber materials as metals semiconductors and superconductors. Metals were found to be extremely efficient absorbers but they had very high heat capacities because of

their large electronic specific heats. Semiconductors with a band gap less than that of the thermistor crystal provided a good alternative. However, these are prone to trapping as in the case of a single thermistor. The best semiconductor absorber was found to be HgCdTe, which has a variable band-gap depending on the percentage of Cd in the material. With 10% Cd, HgCdTe has a 60meV band gap. This material was found to add an additional 11eV thermalisation noise to 6 keV x-rays. The trapping was found to be a function of the band gap and it proved possible to reduce it by reducing the band gap of the material. By removing all the Cd from HgCdTe the semi metal, HgTe is produced. This has a zero band gap and was found to add very little thermalisation noise <3eV to a 6keV x-ray. The problem with semiconductors and metals as absorbers is they have relatively high heat capacities because they have low Debye temperatures. Superconductors at temperatures below their transition temperature offer an attractive alternative as they have a low heat capacity. However, a large amount of the incident x-ray energy goes into the breaking of Cooper pairs to create quasi-particles. These eventually recombined generating phonons. This process is relatively slow, which creates thermalisation noise. Of the superconductors tested by the GSFC, they found that tin in foil form had the best performance, having a thermalisation noise of <3eV for a 6keV x-ray. Its performance is comparable to the HgTe but it has a lower heat capacity.

To summarise, the GSFC found that near unity quantum efficiency with low thermalisation noise was possible for microcalorimeters by including an appropriate absorber. The absorber limitations have important ramifications for the construction of a high-resolution calorimeter with a resolution of 1-2eV. There are two potential paths to create such a microcalorimeter

- Use a metal absorber, which has near perfect thermalisation, and offset the high heat capacity by using a more sensitive thermistor with a very high dR/dT (allowing it to operate closer to the thermodynamic limit) as is done for TES

- Find new more efficient absorber materials with low heat capacities, which can be used with SM.

In light of this, it is unlikely that SM using current absorbers are going to attain a resolution of less than 3eV.

2.2.3 NTD Ge

NTD Ge is a bulk doped semiconductor with a very regular doping profile. It is produced by irradiating a block of germanium in a uniform beam of neutrons. A dopant site is created

when a Ge atom in the lattice captures a neutron from the beam. This makes the parent nucleus unstable, causing a radioactive decay which creates one of two daughter nuclei, arsenic (forming an acceptor site) or selenium (forming a donor site). The ratio of the donor sites to acceptor sites is fixed by the isotopic abundance of the daughter nuclei, for NTD Ge the ratio is 0.32. Different levels of doping are produced by varying the exposure time in the beam.

2.2.3.1 Band structure in semiconductors

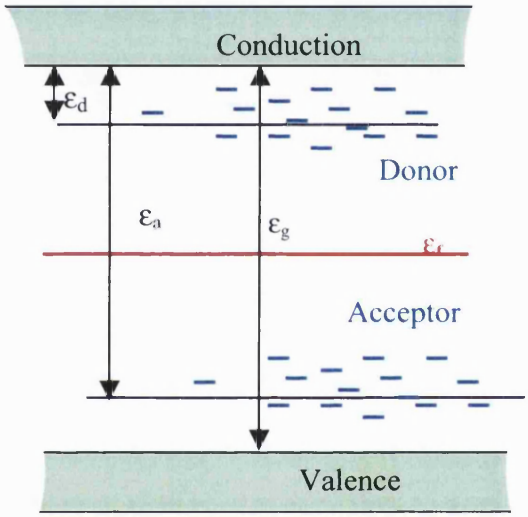

Figure 2.2 A schematic showing the energy band structure of a doped semiconductor. ε_g is the band gap energy of the semiconductor, ε_f is the Fermi level. ε_d and ε_a are the isolated donor and acceptor energies.

To use a semiconductor as a microcalorimeter thermistor, knowledge of how the resistance of the semiconductor varies with temperature and doping level is needed. Here a qualitative outline of the theory concerning the nature of these dependencies is presented. A thorough working of the topic may be found in Shklovskii and Efros [39]. Semiconductors possess an energy band structure created by the superposition of the energy levels of individual atoms within the crystal lattice. This is shown diagrammatically in figure 2.2. The valence band contains electrons bound to their parent nuclei whereas the conduction band contains free electrons. Supplying an energy ε_g to an electron in the valence band liberates it, allowing it to participate in conduction within the crystal. The introduction of dopant atoms into the picture modifies the nature of the conduction process. The levels on donor sites are lightly bound and may be represented by discrete energy levels just below the conduction band. The energy ε_d,

when a Ge atom in the lattice captures a neutron from the beam. This makes the parent nucleus unstable, causing a radioactive decay which creates one of two daughter nuclei, arsenic (forming an acceptor site) or selenium (forming a donor site). The ratio of the donor sites to acceptor sites is fixed by the isotopic abundance of the daughter nuclei, for NTD Ge the ratio is 0.32. Different levels of doping are produced by varying the exposure time in the beam.

2.2.3.1 Band structure in semiconductors

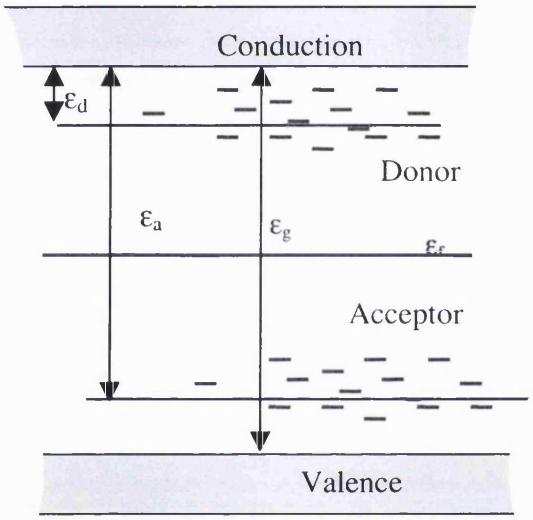

Figure 2.2 A schematic showing the energy band structure of a doped semiconductor. ε_g is the band gap energy of the semiconductor, ε_f is the Fermi level. ε_d and ε_a are the isolated donor and acceptor energies.

To use a semiconductor as a microcalorimeter thermistor, knowledge of how the resistance of the semiconductor varies with temperature and doping level is needed. Here a qualitative outline of the theory concerning the nature of these dependencies is presented. A thorough working of the topic may be found in Shklovskii and Efros [39]. Semiconductors possess an energy band structure created by the superposition of the energy levels of individual atoms within the crystal lattice. This is shown diagrammatically in figure 2.2. The valence band contains electrons bound to their parent nuclei whereas the conduction band contains free electrons. Supplying an energy ε_g to an electron in the valence band liberates it, allowing it to participate in conduction within the crystal. The introduction of dopant atoms into the picture modifies the nature of the conduction process. The levels on donor sites are lightly bound and may be represented by discrete energy levels just below the conduction band. The energy ε_d,

needed to liberate an electron on an isolated donor site, is small compared to ε_g the intrinsic energy gap. Acceptor sites are similarly represented as discrete energy levels above the valence band with ε_a the energy needed to liberate an electron from an isolated acceptor state

2.2.3.2 Conduction properties in NTD Ge

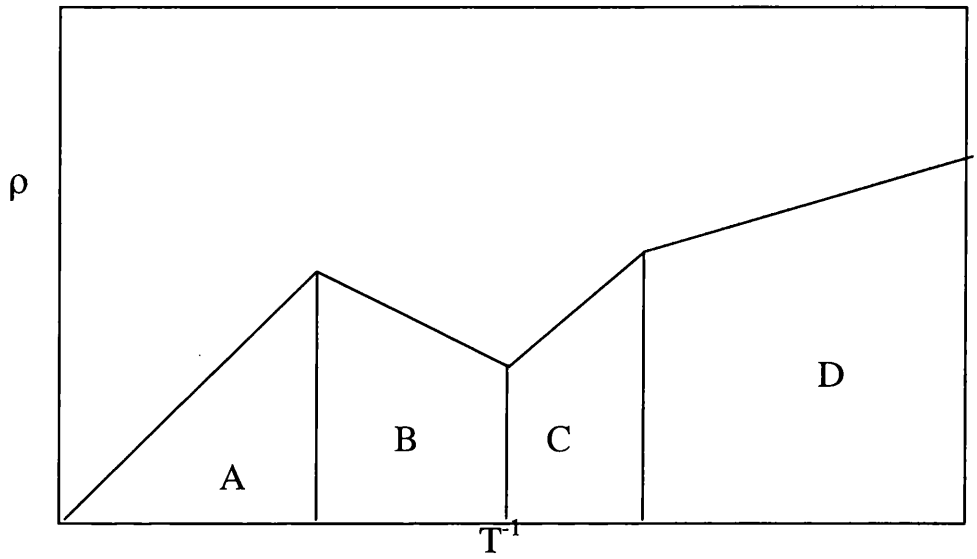

Figure 2.3 A schematic showing the temperature dependence of resistivity ρ for a lightly doped semiconductor with temperature T. Range A is the intrinsic conductivity temperature range (T>400K). Range B is the saturation conduction range (400K<T<50K). C is the freeze out range (50K<T<7K). D is the hopping conduction range (T<7K). Adapted from [39].

At high temperatures (>400K) conduction within the crystal is dominated by the intrinsic carrier concentration of the Ge. The number of those carriers with energy ε_g gives the number of intrinsic carriers N_i that can participate in the conduction process at any instant. The distribution of N_i is given by a Boltzmann distribution

$$N_i(\varepsilon_g) \propto EXP\left(-\frac{\varepsilon_g}{K_B T}\right) \qquad \text{- 2.8}$$

From this, it is seen that the distribution of carriers falls rapidly as a function of temperature. At temperatures in the range 50K-7K the intrinsic carrier concentration is gradually frozen out. At this point, conduction within the crystal becomes dominated by the properties of the

extrinsic carrier population, N_e, provided by the dopant nuclei. For temperatures lower than ~7K the extrinsic electrons and holes become trapped in the potential wells of their parent donor and acceptor sites respectively and all conduction via the conduction band effectively ceases. At temperatures below this, the only way for electrical conduction to occur in the crystal is by nearest neighbour hopping.

2.2.3.3 Hopping conduction

In the hopping regime the only way for a carrier to move within the crystal is to tunnel via the overlapping wave functions of the carriers trapped on their dopant sites. For this process to occur it is necessary to have vacant dopant sites available for the carriers to occupy. The probability of a charged carrier being trapped at a distance r from a point like central potential is given by its wave function, which has the form

$$N_c(r) \propto EXP\left(-\frac{r}{\lambda}\right) \qquad \text{- 2.9}$$

Where λ is the characteristic size of the wave function typically of the order of ~100 $\mathring{A}$. The probability of a number of carriers $N_c(\Delta\varepsilon)$ having an energy $\Delta\varepsilon$ at a temperature T is given by a Boltzmann distribution

$$N_c(\Delta\varepsilon) \propto EXP\left(-\frac{\Delta\varepsilon}{K_B T}\right) \qquad \text{- 2.10}$$

Using the previous two expressions we can derive the form governing the transition between two dopant sites separated physically by a distance r and energy $\Delta\varepsilon$. This is given by a product of the probabilities

$$N_c(r,\Delta\varepsilon) \propto EXP\left(-\frac{\Delta\varepsilon}{K_B T}\right) EXP\left(-\frac{r}{\lambda}\right) \qquad \text{- 2.11}$$

More explicitly, $N_c(r,\Delta\varepsilon)$ gives the rate at which carriers can make a transition between any two states separated by a distance r and energy $\Delta\varepsilon$ within the crystal. This equation governs

the rate at which charge carriers make the transition; it effectively represents the conductivity between any two sites. Thus, the inverse equation gives the resistivity ρ between any two sites

$$\rho \propto EXP\left(\frac{\Delta\varepsilon}{K_B T} + \frac{r}{\lambda}\right) \qquad \text{- 2.12}$$

Having defined the general form of the conduction between any two sites the next step is to extend this to describe the bulk conductivity of the entire crystal. A full derivation begins with the assumption that the bulk conductivity of the crystal may be idealised by a random network of resistors in series and parallel. The problem now is to calculate the conductivity of this network.

Deriving the conductivity in such a network is not a straightforward matter; here a simplification is presented (full details are given in [39]). In equation 2.12 the resistivity for the two site transition at some temperature T is defined by r and $\Delta\varepsilon$. Clearly, sites separated by all energies and distances need to be considered to determine the bulk conductivity of the crystal. To achieve this it is necessary to know something about the dispersion of energy levels within the crystal, this is given by its density of states $D(\varepsilon)$.

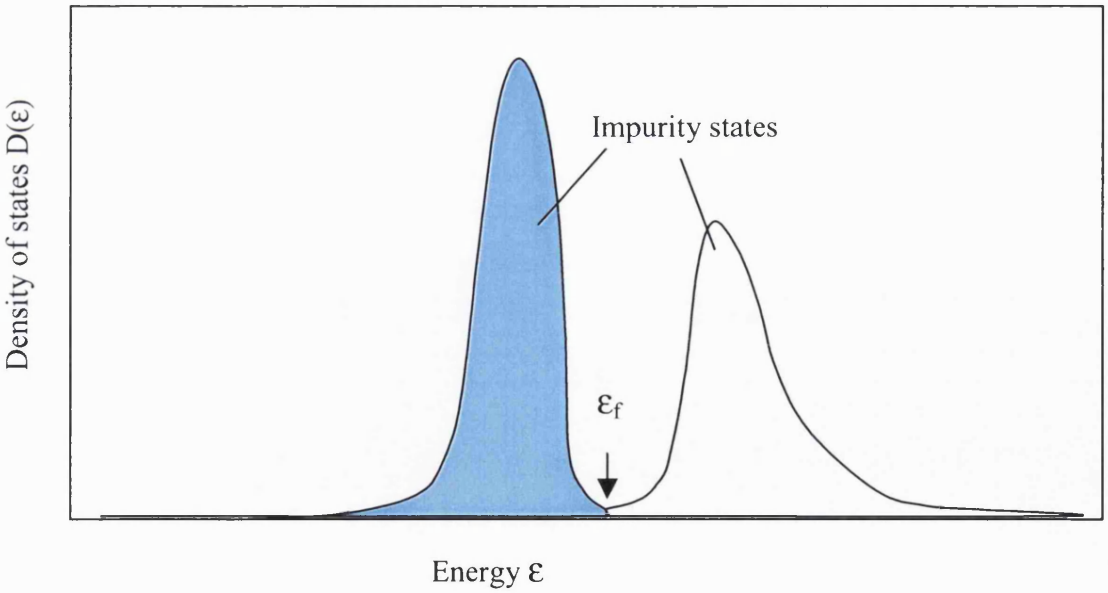

Figure 2.4The density of states D(ε) in a lightly doped semiconductor with intermediate compensation. Note the coulomb gap in the impurity states at the Fermi level ε_f.

The density of states for a crystalline semiconductor is characterised by a Coulomb gap in the density of states at the Fermi level ε_f where $D(\varepsilon) \rightarrow 0$ as shown in Figure 2.4. This gap arises

due to the long-range Coulomb interaction between the dopant sites. Within the Coulomb gap, around the Fermi level, D(ε) has an ε^2 dependence. At low temperatures, the ground state of the system is characterised by its Fermi energy and a small spread of states around this level. So to approximate the density of states at low temperatures we need only be concerned with sites capable of making the small transitions Δε about the Fermi level. The number of such states N(Δε),in this range, in a unit volume is given by area under the curve around the Fermi level

$$N(\Delta\varepsilon) = \int_{\varepsilon_f}^{\varepsilon_f + \Delta\varepsilon} D(\varepsilon_f)\Delta\varepsilon = c'\Delta\varepsilon^3 \qquad \text{- 2.13}$$

Where c′ is a constant, the $\Delta\varepsilon^3$ arises because of the $\Delta\varepsilon^2$ dependency within the coulomb gap. As the energy Δε between these states is small, by definition the number of carriers capable of making the transition between such states will be small from equation 2.10. Correspondingly, the overlap of the carrier wave functions of these states will be small. This being the case the states can be assumed to have no spatial correlation. So the separation between these states can be approximated by their mean separation. This is given by $r=1/(N(\Delta\varepsilon))^{1/3}$. From equation 2.13 the mean inter site spacing, characterised by states around the coulomb gap has the form $r=1/(c'\Delta\varepsilon)$. Substituting this for r into equation 2.12 the form of the resistivity between these states in terms of Δε is

$$\rho \propto EXP\left(\frac{\Delta\varepsilon}{K_B T} + \frac{1}{\lambda c'\Delta\varepsilon}\right) \qquad \text{- 2.14}$$

Examining this equation, we see there are two competing terms in the exponent. The number of carriers available is defined by the first and the second defines the overlap of dopant sites having a characteristic size λ. There will be an optimal value of Δε given by $\Delta\varepsilon = \sqrt{(K_B T/c'\lambda)}$ where the resistivity has a minimum. This implies the conductivity of the entire system is effectively defined by conduction within this narrow band of optimal states about the Fermi level, since the resistivity here has a minimum. If we substitute this back into equation 2.14 we may define the resistivity for the entire crystal as

$$\rho \propto EXP\sqrt{\left(\frac{T_g}{T}\right)} \qquad \text{- 2.15}$$

Where $T_g = (4/(c'\lambda K_B))$ and is a measure of the characteristic activation temperature of states within the optimal band. By normalising equation 2.15 with ρ_o the zero temperature resistivity we arrive at a general form for ρ

$$\rho = \rho_o EXP\sqrt{\left(\frac{T_g}{T}\right)} \qquad \text{- 2.16}$$

Multiplying this by the crystal of thickness d and dividing by the cross sectional area A, the resistance given by equation 2.1 is obtained. The zero temperature resistance is given by $R_o=(d/A)\rho_o$.

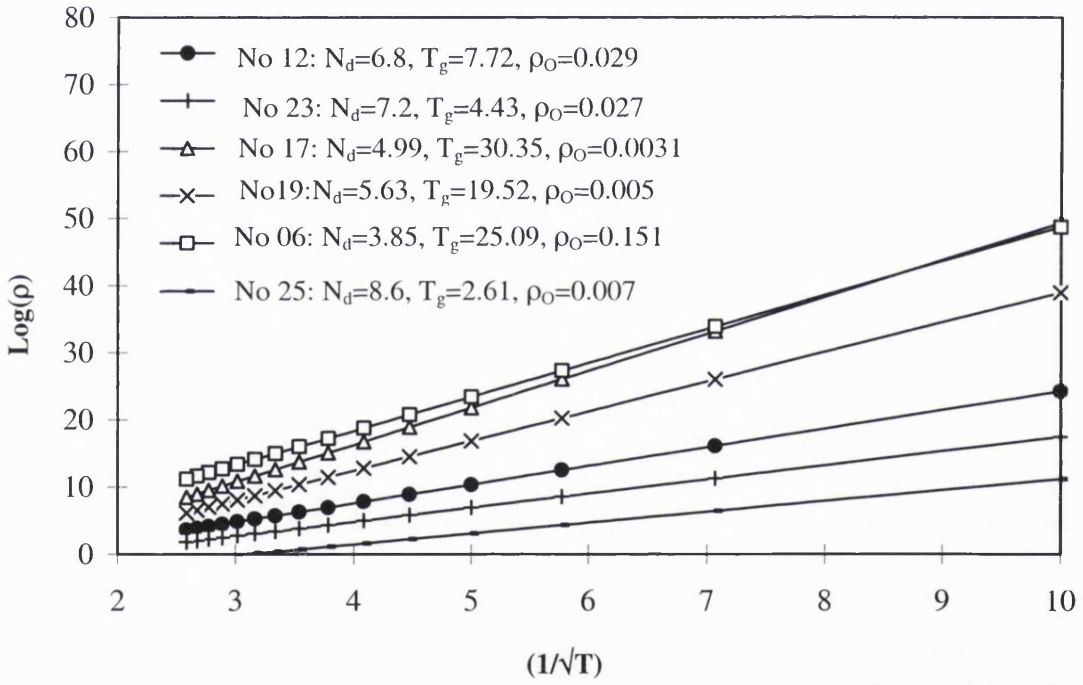

Figure 2.5 A plot of resistivity ρ, Versus temperature T, for selected NTD Ge crystals. Shown are the relationship of the band gap parameter T_g and zero resistivity ρ_o on doping level. The donor concentrations N_d for the different NTD Ge are given in units of ($10^{16}cm^{-3}$) .The values presented are compiled from published sources [40,41,42,43].

What do the above equations tell us about general resistivity in the crystal? The resistivity is defined by T_g and ρ_o. T_g is set by the conductivity within of a narrow band of optimal states. This narrow band of states is fixed by the spatial distribution of sites, which is directly related to the dopant level. Thus by varying the doping level of the crystal, we can tailor its

resistivity. The effect of this relationship for actual NTD Ge crystals is shown in figure 2.5 and table 2.1. The lower the doping level the higher the value of T_g.

NTD Ge number	Donor concentration ($10^{16}cm^{-3}$)	Tg (k)	ρ_o (Ω.cm)
No 25	8.60	2.61	0.007
No 23	7.20	4.43	0.027
No 12	6.80	7.72	0.029
No 19	5.63	19.52	0.005
No 17	4.99	30.35	0.0031
No 06	3.85	25.09	0.151

Table 2.1 The characteristics taken of the differently doped NTD Ge crystals used in simulations later in the thesis. The values presented are compiled from published sources [44,45,46,47].

The different serial numbers shown in the above table and figure for each NTD Ge along with its corresponding ρ_o and T_g are taken from published data [48,49,50,51]. All values modelled for the NTD Ge later in the thesis use these values. All the experimental crystals tested during the PhD were obtained from E.E. Haller at the University of California, Berkeley.

2.3 Bolometer theory

A description of how a SM will operate within the biasing circuit is needed in order to determine how to achieve an optimal response from the overall system. For SM, this is largely provided by ideal bolometer theory. Ideal bolometer theory has been developed by many authors [52,53,54,55] to describe the operational response of an infrared bolometer. The theory presented here summarises those topics pertinent to microcalorimeters; full treatments of bolometer theory are found in the associated references.

Physically a bolometer is the same as a microcalorimeter, consisting of a semiconductor thermistor bonded to an absorber. It operates in the same biasing circuit as a

microcalorimeter, as shown in figure 2.1. The difference between them arises because of the regime in which they are expected to operate. For a bolometer, when detecting extraterrestrial infrared sources, corrections must be made for the presence of a large contaminating infrared background, emitted by the instrument, earth etc. Thus, to detect anything in the infrared region, the desired signature must be extracted from within this large background flux. The typical method for doing this with astronomical sources is to switch between viewing a region of sky near the source, thus measuring the background, then viewing the source and sky, effectively measuring the background plus the source signal. Physically this is achieved by nodding the telescope back and forth from the desired source to a nearby region of sky producing a modulated flux of infrared radiation with the modulation frequency given by the nodding frequency of the telescope (typically around 10Hz). The chopping frequency is then extracted electronically by phase sensitive detection and all other frequencies are discarded. The amplitude of the final detected waveform then gives the magnitude of the source at that point in the sky. The implication here is that mathematically, a bolometer system can be regarded as being in a state of quasi-thermal equilibrium, varying by small amounts about an equilibrium point because of the modulated signal from the nodding process. In addition, the bandwidth of the detection stage has no effect on the detection of the infrared signal, as long as the chopping frequency can be accommodated. This means the bandwidth of the detection system can be disregarded.

2.3.1 Equilibrium State

A description of the bolometer in its bias circuit requires three fundamental relationships

- The detector resistance R(T)
- The power flowing through thermal link to the heat sink $W(T-T_o)$
- The bulk heat capacity of the entire device C (T).

These relationships typically have the forms given by equation 2.1, 2.18, 2.7 respectively. Using these fundamental relationships, a model of the response of the detector for all bias currents and heat sink temperatures can be derived. The relationship between the heat sink temperature T_o and the detector temperature T is given implicitly by the detector load curve. The detector load curve is the name given for the relationship between the applied voltage V and bias current I and is derived from a knowledge of the detector resistance R(T) and the dependence of the thermal power $W(T-T_o)$ flowing through the thermal link to the heat sink at a temperature T_o . A set of typical load curves for a bolometer is shown in figure 2.6. To

derive the load curve relationship we assume that the detector is at some equilibrium temperature T above the heat sink temperature T_o.

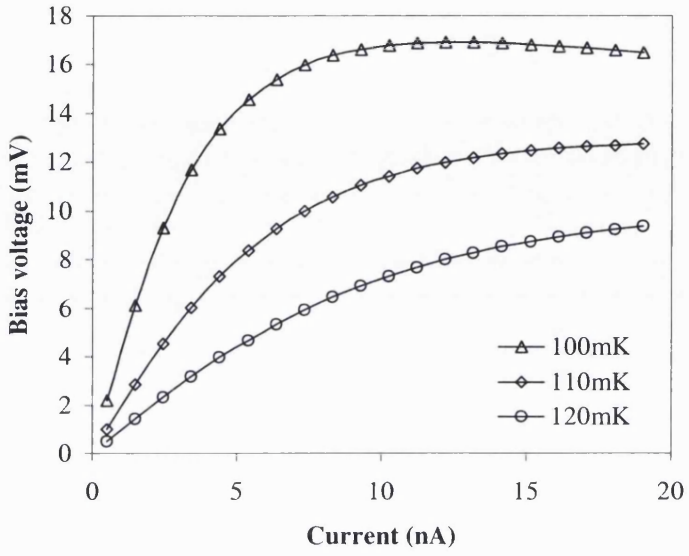

Figure 2.6 A typical set of load curves. These are for a (0.25x0.25x0.25)mm^3 NTD Ge No 17 bolometer bonded to two 8μm ∅, 1mm long copper thermal links.

The thermal power $W(T-T_o)$ flowing into the heat sink is defined by the conductivity K(T) of the thermal link. K(T). Typically metallic links are used and can be described by

$$K(T) = K_o\left(\frac{T}{T_o}\right)^{\beta} \qquad \text{- 2.17}$$

K_o and β are constants, depending on the link material. The thermal power flowing to the heat sink along a link of cross section A, length L and conductivity K(T) is then described by

$$W(T - T_o) = \frac{A}{L}\int_{T_o}^{T} K(T)dT \qquad \text{- 2.18}$$

For equilibrium this must be equivalent to the bias power dissipated in the resistance R(T), by the bias voltage V, which is given by $V^2/R(T)$. With the bolometer operating in the presence of an additional background power source, dumping an additional thermal power Q_b in the bolometer, the equilibrium voltage V(T) is modified to

$$V(T) = \sqrt{\left((W(T-T_o)-Q_b).R(T)\right)} \qquad \text{- 2.19}$$

Similarly the equilibrium current I can be defined as

$$I(T) = \sqrt{\left(\frac{(W(T-T_o)-Q_b)}{R(T)}\right)} \qquad \text{- 2.20}$$

Combining both these equations, the load curve V(I) for the detector may be obtained. Each point on the load curve then represents an equilibrium state of the microcalorimeter at some temperature T above the heat sink T_o.

2.3.2 Load curve parameters

Having obtained the equilibrium operating points of the detector, a description of how the detector will respond to an incident signal and how it is compromised by noise can now be determined. To achieve this we must calculate a number of parameters, which describe the bolometers response at a load curve position.

The rate of change of the detector resistance at any biasing point is given by the detector's thermal coefficient of resistance

$$\alpha = \frac{1}{R(T)}\frac{dR}{dT} = -\frac{1}{2}\left(\frac{T_g^{1/2}}{T^{3/2}}\right) \qquad \text{- 2.21}$$

The dynamic conductance, G_d gives the rate of change of thermal power to the heat sink for any point on the load curve

$$G_d = \frac{dW}{dT} = \frac{A}{L}K_o\left(\frac{T}{T_o}\right)^{\beta} \qquad \text{- 2.22}$$

Physically G_d is modified by the dissipation of external power P in the detector to give the effective conductance G_e

$$G_e = G_d - \alpha P\left(\frac{R_L - R}{R_L + R}\right) \qquad \text{- 2.23}$$

The external power P absorbed by a bolometer is the sum of the background power Q_b and the electrical bias power $I^2R(T)$ dissipated in the detector. Using the bulk heat capacity C(T) given in equation 2.7 and G_d from equation 2.22, the intrinsic thermal time constant τ for the detector may be defined for each explicit load curve temperature T

$$\tau = \frac{C(T)}{G_d(T)} \qquad \text{- 2.24}$$

This is modified by the presence of external power being dissipated in the bolometer, via equation 2.23, to give an effective time constant τ_e of the bolometer

$$\tau_e = \frac{C(T)}{G_e(T)} \qquad \text{- 2.25}$$

Electrically a bolometer is not a pure resistance but has associated with it some impedance. The zero frequency impedance Z of the detector is give by the slope of the load curve at a bias point

$$Z = R\left(\frac{G_d + \alpha P}{G_d - \alpha P}\right) \qquad \text{- 2.26}$$

This impedance arises because of the finite thermal time τ the detector takes to respond to changes in its equilibrium position. At high frequencies Z is modified to give the effective detector impedance $Z(\omega)$

$$Z(\omega) = Z\frac{1 + j\omega\tau\left(\frac{Z+R}{2Z}\right)}{1 + j\omega\tau\left(\frac{Z+R}{2R}\right)} \qquad \text{- 2.27}$$

It is seen here that Z(ω) is a complex quantity; it represents the electrical response of the bolometer at all frequencies. The spectral from of the impedance defined by equation 2.27 is shown schematically in figure 2.7 and its complex nature in figure 2.8.

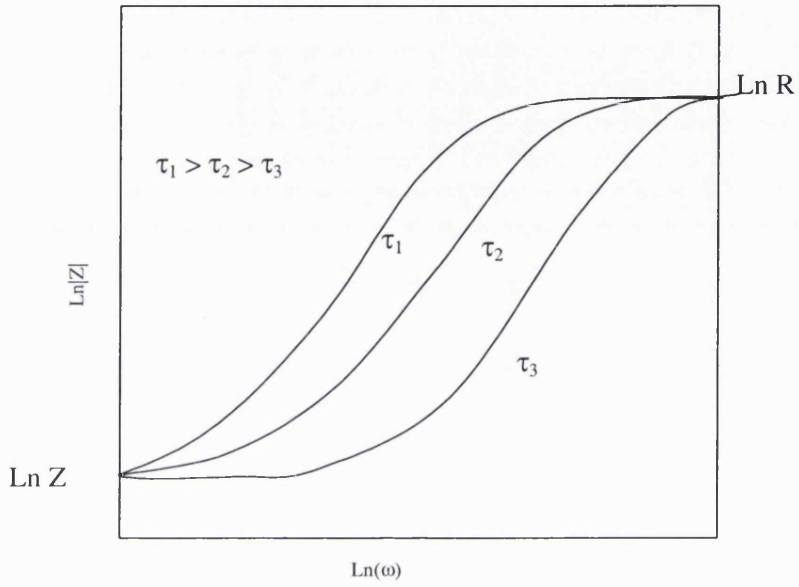

Figure 2.7 The frequency dependence of the impedance and its relationship to the bolometer time constant τ. At high frequencies, the bolometer approaches the resistance at that operating point R and at very low frequencies, it approaches Z the DC impedance.

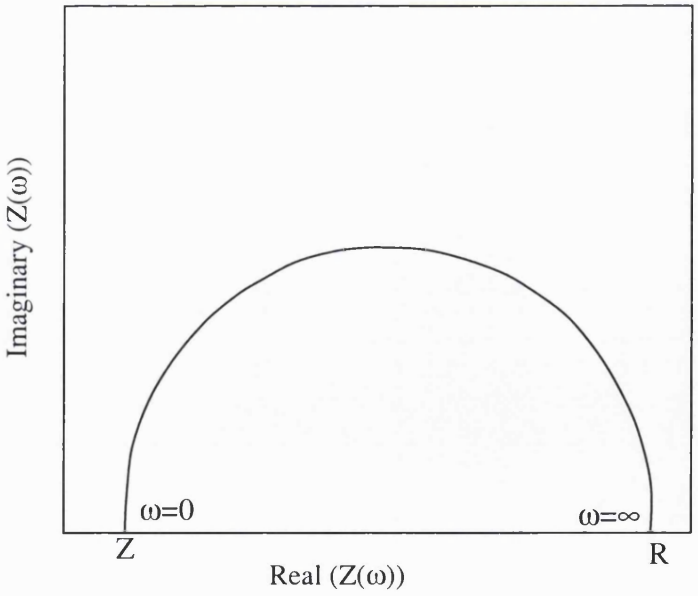

Figure 2.8 The complex nature of the bolometer impedance Z(ω). At high frequencies the bolometer is purely resistive and has a resistance given by R. At low frequencies it is resistive and given by Z the DC impedance. For intermediate frequencies, it has a large inductive component.

The rate of change of the detector voltage to a given input power is defined as the detector responsivity. The equilibrium value for the responsivity is given by

$$S_o = \frac{dV}{dW} = \frac{\alpha V}{G_e} \qquad \textbf{- 2.28}$$

S_O varies with frequency. This is given by the frequency dependent form $S(\omega)$ as

$$S(\omega) = \frac{\alpha V}{G_e}\left(\frac{R_L}{R_L - Z(\omega)}\right)\left(\frac{1}{\sqrt{1+\omega^2\tau_e{}^2}}\right) \qquad \textbf{- 2.29}$$

This term contains the intrinsic frequency dependence of the bolometer and its associated circuit. The last bracketed term of 2.29 contains the dependence on the effective time constant. The effect of the bolometer circuit, given in the first set of brackets, is superimposed on this. The bolometer circuit attenuates the bolometer responsivity across the load resistor R_L to ground.

Using the equations defined above, the detector response to any absorbed thermal signal can now be ascertained, whether it is generated by an external signal or by noise mechanisms within the bolometer circuit.

2.3.3 Noise analysis

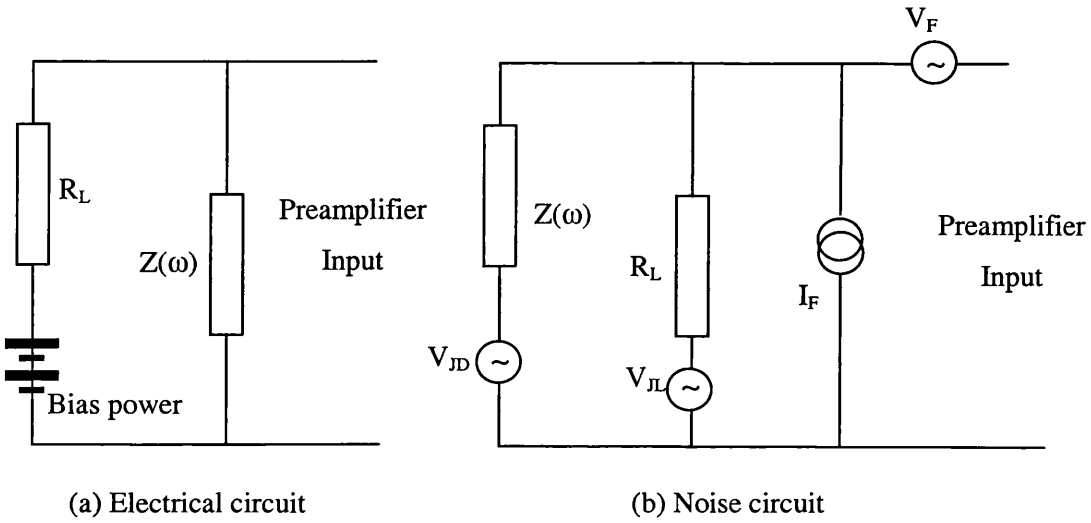

(a) Electrical circuit (b) Noise circuit

Figure 2.9 The bias circuit and a schematic of the associated noise model. $Z(\omega)$ is the detector impedance and R_L the load resistance. Associated with the detector and load resistances are two Johnson noise sources V_{JD} and V_{JL}. V_F and I_F are the associated pre-amp voltage and current noise sources.

Five sources of noise are associated with a bolometer circuit, which are shown schematically in figure 2.9 these are

- Phonon noise V_P
- Johnson noise V_{JD} from the bolometer
- Johnson noise V_{JL} from the load
- Preamplifier voltage noise V_F
- Preamplifier current noise I_F

Phonon noise V_P and Johnson noise V_{JD} arise in the bolometer. In addition to these, there are other noise sources associated with the bias circuit; Johnson noise from the load resistance R_L, preamplifier voltage noise V_F and preamplifier current noise I_F, which also need to be considered. With a selective choice of components, the noise from the additional sources can be minimised [53] and in theory, a resolution very close to that given by equation 2.6 should be attainable.

2.3.3.1 Phonon noise

Phonon noise is essentially a type of shot noise arising in the detector thermal links, created by the random number of phonons flowing through the links, generated by the random thermal fluctuations within the detector. The magnitude of the Phonon noise varies with a Gaussian distribution over time and frequency. This distribution can be defined by the RMS spread in its Noise Equivalent Power (NEP), which is given as

$$NEP_P = \sqrt{(4K_B G_d)}T \qquad \text{- 2.30}$$

Where K_B is Boltzmann's constant and G_d the thermal conductance of the link to the heat sink. An additional factor needs to be added to this term Φ. This arises because of the thermal gradient ($T-T_O$) in the links, this has been shown [53] to reduce the typical RMS excursion of the NEP and is given by

$$\Phi = \left(\left(1-\frac{3}{2}(T-T_o)\right)+\left(\frac{15}{12}(T-T_o)^2\right)\right) \qquad \text{- 2.31}$$

The thermal signal generated by NEP_p has equal contributions from all frequencies giving it an RMS spread that is spectrally constant. As shown in equation 2.29 the detector responsivity $S(\omega)$ is frequency dependent and has a roll off at high frequencies. The result is the envelope of $S(\omega)$ is superimposed on the noise voltage V_P generated by NEP_p. Combining both these effects, we have the phonon voltage noise V_p in the bolometer circuit as

$$V_p = NEP_p \Phi S(\omega) \qquad \text{- 2.32}$$

2.3.3.2 Johnson noise

The random thermal motion of electrons in any resistance gives rise to Johnson noise. The amplitude of the voltage signal produced by the Johnson noise varies with a Gaussian distribution. This Gaussian distribution has a RMS spread given by $V_{JD} = \sqrt{(4K_B TR)}$. The RMS spread is spectrally constant up to high frequencies (GHz). The associated resistance in a bolometer is a Johnson noise source, which generates a noise V_{JD}. This is described by the Johnson noise arising in a resistance however, a bolometer is not a straightforward resistance,

so the form of V_{JD} needs to be modified to account for the electro-thermal nature of the bolometer. The presence of electro-thermal effects means the bias power does work in the bolometer and effectively suppresses any resistance changes in the detector. This effect reduces the magnitude of the RMS spread V_{JD}. Additionally within a bolometer circuit, any noise voltage generated across the detector will decay to ground across the potential divider created by the bolometer in series with the load resistor. This has the effect of reducing the magnitude of the RMS voltage spread V_{JD}. Both these effects combined modify the standard Johnson noise to

$$V_{JD} = \sqrt{(4K_B TR)}\left(\frac{R_L}{R_L + Z(\omega)}\right)\left(\frac{\left(\omega + \frac{1}{j\tau}\right)}{\left(\omega + \frac{1}{j\tau_e}\right)}\right) \qquad \text{- 2.33}$$

This is the resultant Johnson noise from the bolometer within its circut. Examining this equation, we see that it is the standard Johnson noise term, multiplied by two additional terms; the first term accounting for the attenuation of the voltage noise across the load resistor R_L, the second term accounting for the electro thermal feedback effect [42].

Similarly, the load resistor is also a source of Johnson noise, this is a standard resistor, but it needs to be modified for the effect of the bolometer bias circuit. Any voltages developed across the load resistance are attenuated to ground across the potential divider created by the detector impedance $Z(\omega)$. By combining this with the standard Johnson noise term the resultant Johnson noise from the load resistor is

$$V_{JL} = \sqrt{(4K_B T_o R_L)}\left(\frac{Z(\omega)}{Z(\omega) + R_L}\right) \qquad \text{- 2.34}$$

Here we see that the magnitude of the typical RMS spread is reduced across the complex impedance of the detector, causing the whole term to vary with frequency giving a roll off at high frequencies governed by the bolometer impedance.

2.3.3.3 Preamplifier noise

Bolometers are constant current biased detectors, which use high input impedance JFET as preamplifiers.

JFET's generate voltage noise, which arises from Johnson noise in the channel of the JFET, because the channel has associated with it some resistance. This noise is superimposed on the detector signal, giving rise to the effective noise quantity V_F that appears at the output of the preamplifier chain. There is no direct method to calculate the magnitude of V_F, it needs to be determined experimentally, by measuring the RMS input short noise of the preamplifier. The RMS value of V_F is effectively constant at all frequencies, with the amplitude varying as a Gaussian distribution.

In addition to the voltage noise, the JFET also generates current noise V_C. This is generated by the leakage current I_A that travels from the channel to the gate of the JFET, because across these terminals the JFET is effectively a PN junction. This noise can not be calculated and needs to be measured experimentally. The RMS spread of this quantity will generate a current noise in ($A/\sqrt{Hz}$). This in turn creates a voltage noise ($I_A R_L$) across the load resistor, which is attenuated to ground across the potential divider created by the load resistance R_L and the detector impedance $Z(\omega)$ to give

$$V_C = I_A R_L \left(\frac{Z(\omega)}{Z(\omega) + R_L} \right) \qquad \text{- 2.35}$$

We see here that although the RMS value of ($I_A R_L$) is spectrally constant, the final noise voltage at the output of the system is not. It has a spectral roll off at high frequencies created by the detector impedance $Z(\omega)$.

2.4 Application of bolometer theory to microcalorimeters

Bolometer theory provides a general framework within which the response of a microcalorimeter can be calculated, but three additional areas need to be incorporated.

The voltage pulse produced by an x-ray contains spectral information up to high frequencies. The peak of the pulse is dominated by high frequency components, these are parasitically filtered by the R-C roll off within the bias circuit. This results in a considerable reduction in the detected amplitude and signal to noise ratio of the final voltage pulse. The energies involved in detecting x-rays are relatively large compared to the infrared signals that bolometers detect. As a result, microcalorimeters cannot be regarded as being in a state of quasi-equilibrium during a detection event: standard bolometer theory relies on this being the case. The high resolutions expected for future microcalorimeters means that these detectors need to be run at sub 100mK temperatures. At temperatures below 300mK the hopping conduction process described in section 2, is reduced by the non-ideal solid state phenomena of electron-phonon decoupling and the electric field effect. Standard bolometer theory does not include these effects. All of these effects can potentially compromise the resolution of a x-ray microcalorimeter and need to be included in a model of the resolution of a microcalorimeter system.

2.4.1 Attenuation by system bandwidth

Bolometer theory assumes that the detector is not system limited as mentioned in section 2.3 but this is not true for microcalorimeters. The voltage signals from a x-ray event have a large frequency spread, the sharp peak of the voltage pulse generated by an x-ray, will contain very high frequencies that are filtered by stray capacitances in the biasing circuit. An estimate of the bandwidth of a microcalorimeter circuit having a resistance R(T) and capacitance C is given by its 3_{DB} point which is $1/(2\pi R(T)C)$. A typical microcalorimeter resistance may lie in the range 10-100MΩ. An estimate of the system capacitance is obtained by noting that a typical JFET input capacitance is ~ 4pF. From this, we estimate the lower limit of the system bandwidth as ~400Hz. The spectral extent of a x-ray pulse with a decay constant τ_e can be estimated by $(1/\tau_e)$Hz. A typical microcalorimeter will have a time constant faster than 1ms giving a lower limit to the spectral extent of the pulse of 1kHz. Clearly, such a pulse is retarded by the bias circuit. The peak of the x-ray pulse, contains most of the high frequency information, this is contained in a small temporal region less than 1μs. This implies the peak

contains spectral information out to 1MHz. This is preferentially lost by the bias system, exacerbating the attenuation problem, since this region contains most of the height of the pulse. To accurately calculate the height of voltage pulses in the system we must incorporate attenuation.

2.4.2 Signal induced non linearity

The small signal analysis assumed by bolometer theory is not always applicable to a study of microcalorimeters. Low heat capacities and potentially large x-ray energies may drive the detector system out of equilibrium during a pulse event into a regime that is not described small signal analysis. Whether or not the microcalorimeter is in equilibrium and can still be described by standard bolometer theory during the detection of a x-ray photon needs to be ascertained. One way to assess this is to model the change of the normal equilibrium parameters, during a x-ray event, from their normal equilibrium values. The temporal profile of an ideal temperature pulse produced by an x-ray of Q Joules in a detector of heat capacity $C(T_{equ})$, at its equilibrium temperature T_{equ} can be modelled by

$$T(t) = T_{equ} + \left(\frac{Q(T_{equ})}{C}\right)\mathrm{Exp}\left(-\frac{t}{\tau_e}\right) \qquad \text{- 2.36}$$

Where the temperature pulse decays exponentially back to the equilibrium temperature, with the effective detector time constant. By calculating the responsivity, system bandwidth, heat capacity and detector noise, the effect of nonlinear, temperature induced effects, during the temperature pulse can be modelled.

The percentage change of these values from their equilibrium levels was estimated for a typical MSSL microcalorimeter set up. The microcalorimeter was modelled at two operating temperatures 50mK and 20mK, when detecting 1keV, 5keV and 10keV x-rays. The results are shown in figure 2.10. This plot was generated for a $(0.25x0.25x0.25)mm^3$ NTD Ge thermistor, ρ_O and T_g are those for NTD Ge No 19 (see figure 2.5, table 2.1). NTD Ge No 19 has a relatively high doping level and correspondingly low resistance at the modelled temperatures. At 50mK the non linearity effect was found not too severe, when detecting a 10keV x-ray the system is just beginning to deviate from its equilibrium state. However, at 20mK even a 1keV photon caused the detector to deviate significantly from its equilibrium

state. Clearly for this detector at temperatures below 50mK the non-linearity of the detector must be addressed in some fashion.

The effects demonstrated here can be exacerbated if different crystals and crystal sizes are used. For instance, a more lightly doped semiconductor has a larger T_g, which gives it a larger thermal coefficient of resistance, α in this temperature range, so the relative change of circuit attenuation, noise and responsivity will be increased. Similarly, if using a smaller crystal, the magnitude of the induced temperature excursion increases. To better understand the behaviour of any crystal, these effects need to be modelled for a variety of doping levels and crystal sizes.

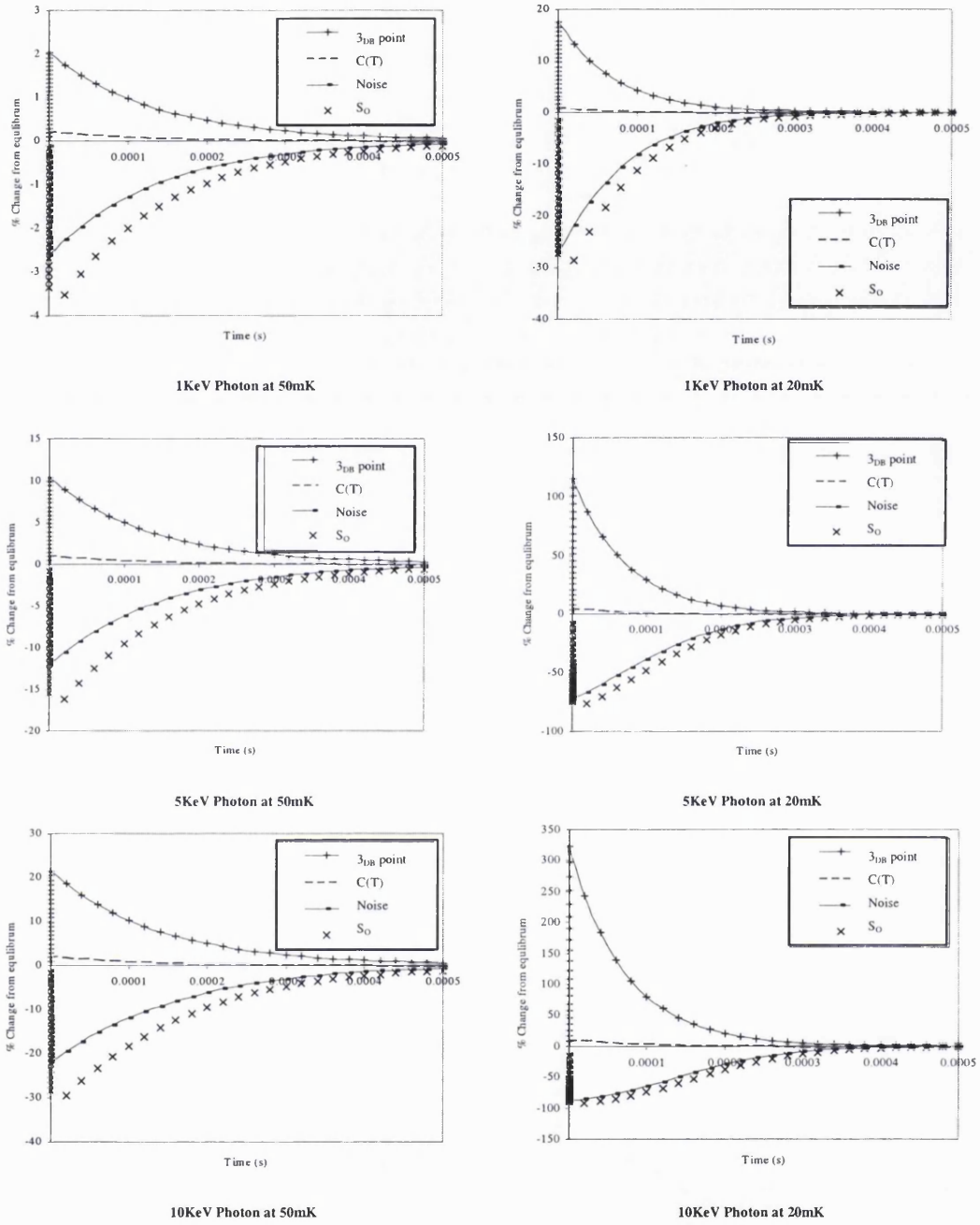

Figure 2.10 Detector response at 20mK and 50mK of a (0.25x0.25x0.25)mm^3 NTD Ge No19 detector with a 0.5mm^2 0.015mm thick Sn absorber, 2 x 8μm ∅, 0.5mm long brass wires. For 1, 5 and 10keV x-rays. The plots show the % change of the DC responsivity S_o, The heat capacity C_{Bulk}, The bandwidth 3_{DB} and the noise V_{noise} from their equilibrium values during and x-ray event.

2.4.3 Non ideal solid state effects

2.4.3.1 The electric field effect

At temperatures less than 300mK, observations of resistivity in semiconductors exhibit a deviation from the temperature dependence characteristic of variable range hopping. It is postulated that this effect is due to the presence of the electric field across the detector, which changes the conduction properties of the crystal [56,57].

The effect of the field on conduction in the crystal can be explained in a similar fashion to that for hopping conduction (in section 2.2.3.3). Equation 2.9 gives a probability that a charge carrier will be a distance, r, from an impurity trap and equation 2.10 gives the proportion of carriers with energy, $\Delta\varepsilon$, capable of making the transition to a neighbouring trap. In the presence of an external electric field of magnitude E, the potential of the trap is effectively increased to ($\Delta\varepsilon$-eEr), where e is the electronic charge. Consequently, equation 2.10 is modified. Now the number of carriers N_c capable of making the transition is changed to

$$N_c(\Delta\varepsilon, E) \propto EXP - \left(\frac{\Delta\varepsilon - eEr}{K_B T}\right) \qquad \textbf{- 2.37}$$

or

$$N_c(\Delta\varepsilon, E) \propto EXP - \left(\frac{\Delta\varepsilon}{K_B T}\right) EXP\left(\frac{-eEr}{K_B T}\right) \qquad \textbf{- 2.38}$$

The first term is unchanged from equation 2.10 in the hopping conduction derivation in section 2.233. As before, $\Delta\varepsilon$ and r can be approximated to give the same answer as that arrived at in equation 2.16 multiplied by the second exponential term to give

$$\rho(T, E) = \rho_o EXP\left(\left(\frac{T_g}{T}\right)^{\frac{1}{2}}\right) EXP\left(\frac{-eEr}{K_B T}\right) \qquad \textbf{- 2.39}$$

Replacing r by the average hopping length L, as given by Mott's law, and changing the resistivity into resistance, we arrive at the standard equation representing the effect of the field on the conduction properties within the crystal

$$R(T,E) = R_o EXP\left(\left(\frac{T_g}{T}\right)^{\frac{1}{2}}\right) EXP\left(\frac{-eEL}{K_B T}\right) \qquad \text{- 2.40}$$

The inclusion of the electric field effect in the resistance of NTD Ge has proved effective in explaining most of the observed deviations from normal hopping conduction in the temperature range 100mK to 300mK. However, it is generally accepted that the electric field effect alone cannot account for observed deviations at temperatures below 100mK [58].

2.4.3.2 Electron-phonon decoupling

At temperatures below 100mK electron-phonon decoupling offers the best description for the observed deviation from variable range hopping [59]. The resistivity, as described by variable range hopping, relies on energy being imported to charge carriers frozen on trapping sites allowing them to tunnel to new states. The mechanism for delivering this energy is the absorption and emission of phonons. The rate at which this interaction occurs is proportional to the product of the electron density of states given by the Fermi function f(e) and the phonon distribution n(q). The Fermi function is a Fermi-Dirac distribution and dependent on the temperature of the electron gas whilst the phonon distribution is a Bose-Einstein distribution and dependent on the temperature of the phonon population. As the temperature is reduced, there are a rapidly diminishing number of states into which the phonons and electrons can scatter, this reduces the coupling between the phonons and electrons. Therefore, the bias power dissipated in the electron population cannot readily leak into the lattice and consequently heats up the electron gas relative to the lattice.

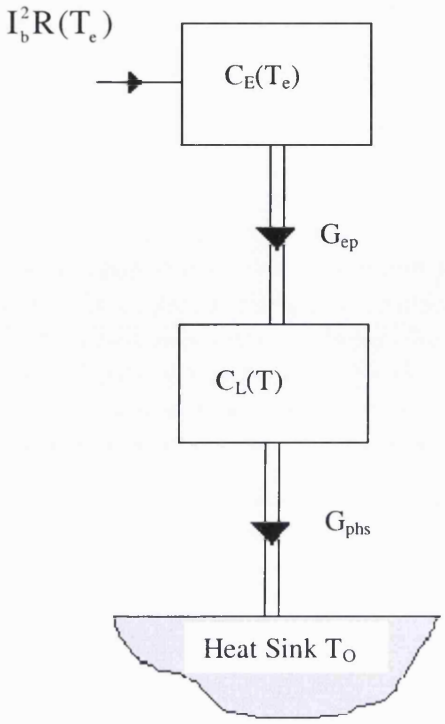

Figure 2.11 A schematic diagram showing the thermal model of the detector as a two component system. Consisting of electrons with heat capacity C_E and lattice with heat capacity C_L coupled by the conductance G_{ep}. The bias power $I_b^2R(T_e)$ heats the electron component whilst the lattice cools via the conductance G_{phs} to the heat sink (Adapted from [60]).

This effect can be modelled simply by the inclusion of the thermal impedance G_{ep} between the electron and the phonon population as shown in figure 2.11. The equilibrium power W_{ep} flowing from the electron population at a temperature T_e to the phonon population at some temperature T via the conductance G_{ep} is given by

$$W_{ep}(T_e - T) = G_{ep}\left(T_e^{\alpha'+1} - T^{\alpha'+1}\right) \qquad \text{- 2.41}$$

Where α' is a constant ~5. G_{ep} has units ($W/K^{\alpha'+1}$). It is assumed that the resistance is dependent on the temperature T_e of the carrier population alone, since only the carriers contribute to conductivity within the crystal. Incorporating this change into equation 2.1 gives

$$R(T) = R_o EXP\left(\sqrt{\left(\frac{T_g}{T_e}\right)}\right) \qquad \text{- 2.42}$$

Including the electron-phonon decoupling model, with hopping conduction for NTD resistance, has proved successful in reproducing the observed VIs of NTD Ge thermistors at

temperatures below 100mK, as shown in figure 2.12. the model produces a good fit to observed data. The correlation below 25mK is not exact, this implies that there are additional effects, unaccounted for by the electron-phonon decoupling models.

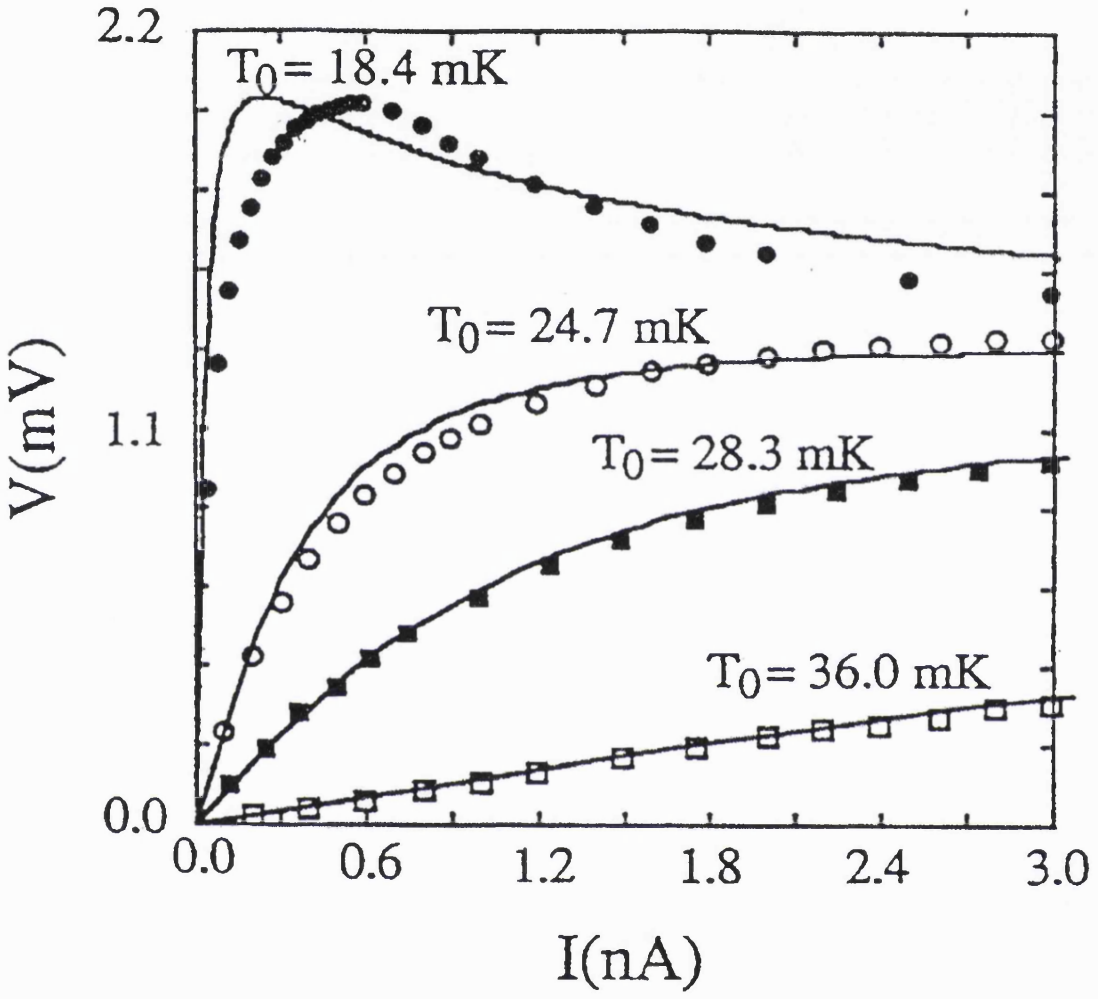

Figure 2.12A comparison of experimentally obtained VI in the temperature range 18 to 36mK, with the corresponding predictions of the electron-phonon decoupling model. Solid lines are the model predictions and symbols experimental data. (Taken from ref [58]).

3 Numerical model of a microcalorimeter system

3.1 Introduction

The last chapter has shown that ideal bolometer theory alone is not sufficient to describe the behaviour of microcalorimeters at all temperatures and photon energies. In particular it fails to address four major effects.

- Attenuation of the x-ray pulse by the detector system.
- Non linear detector and system response during the detection of high energy x-rays at low temperatures.
- Modified hopping conduction created by the presence of an electric field across the detector.
- Electron-phonon decoupling within the crystal at low temperatures.

The extent to which each of these effects compromises the final resolution of the system needs to be assessed for all potential operating points of the system. Because of the complexity of the system and the number of free parameters involved, the method chosen to achieve this aim was to numerically model the detector system for all operating points of interest.

The four non-ideal effects were simulated, by constructing three separate numerical models of the detector system. The first modelled the effect of system attenuation and included the effect of a non-linear heat capacity system on system resolution. The final two models added the effects of electron-phonon decoupling and the electric field respectively.

3.2 Basic model elements

All the system models constructed relied on three common sub models :

- A model of the detectors thermal system
- A model of the transfer characteristics of the bias circuit
- A model to calculate the system noise at an equilibrium point on a load curve.

The model of the detector's thermal system is based on that shown in figure 2.1. This model is used to generate the thermal profile of a x-ray induced pulse, which is converted into a voltage pulse. The model of the transfer characteristics then allows the attenuation of a voltage signal in the bias/readout circuit to be simulated. The noise model uses bolometer theory to calculate the system noise at an equilibrium point on the load curve. Combining the inputs of the sub models for the different scenarios allows the signal to noise of a given operating point to be calculated.

3.2.1 Thermal system

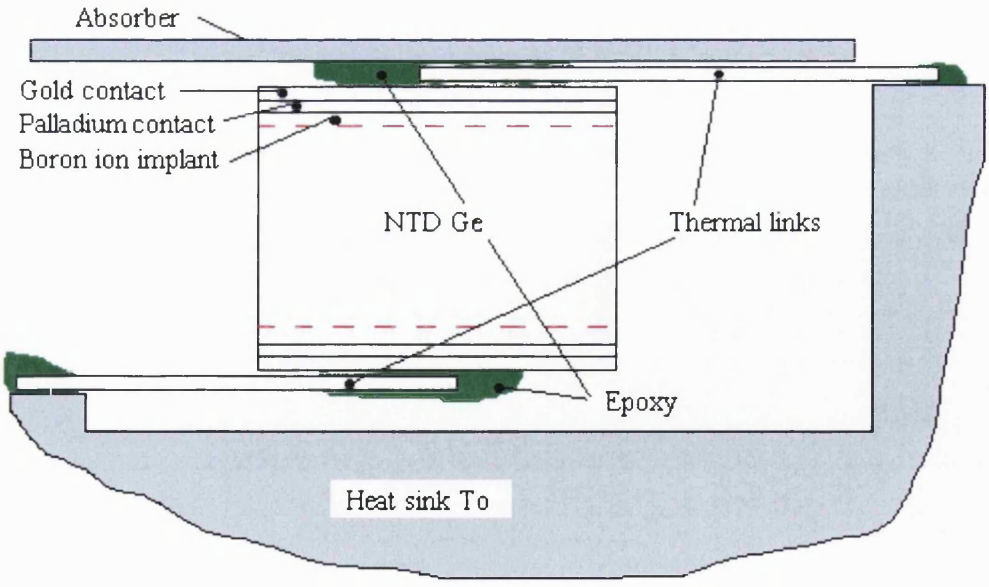

Figure 3.1 A schematic showing the assumed physical format for the detector models.

The thermal model was developed for the NTD Ge detectors used at MSSL. A schematic typical of these detectors is shown in figure 3.1. The NTD Ge crystals have two opposing

faces with a 20nm thick gold layer on top of a 400nm palladium layer; beneath these there is a 1μm thick boron ion doped layer. These dimensions were fixed in the model; all other dimensions and the materials chosen for the thermal links, absorber and epoxy were left as free parameters.

Thermally, a precise model of the detector presented in figure 3.1 would be complicated since there will be thermal impedances at the boundaries between all the components (this is dealt with further in section 4.3.3). For simplicity, it is assumed that the internal boundaries of the detector do not exist and that the only thermally restricting boundary is the thermal link to the heat sink. In other words, within the entire volume of the detector, all the elements are in thermal equilibrium forming a compound heat capacity $C_{Bulk}(T)$.

To create the compound heat capacity, the dimensions of the elements and their heat capacities over the range of interest are needed. The bulk heat capacity is given by

$$C_{Bulk}(T) = A.T^3 + B.T \qquad \textbf{- 3.1}$$

where the coefficients A and B, are summed over all components,

$$A = vol_1.a_1 + vol_2.a_2 + vol_3.a_3.... \qquad \textbf{- 3.2}$$

$$B = vol_1.b_1 + vol_2.b_2 + vol_3.b_3.... \qquad \textbf{- 3.3}$$

and ai and bi are the lattice and electron constants of the i^{th} component. The power flowing to the thermal link is modelled by equation 2.18.

These equations define the thermal model of the system. By numerically solving them, the response of the system to the deposition of energy by a x-ray pulse can be modelled.

3.2.2 Transfer characteristics

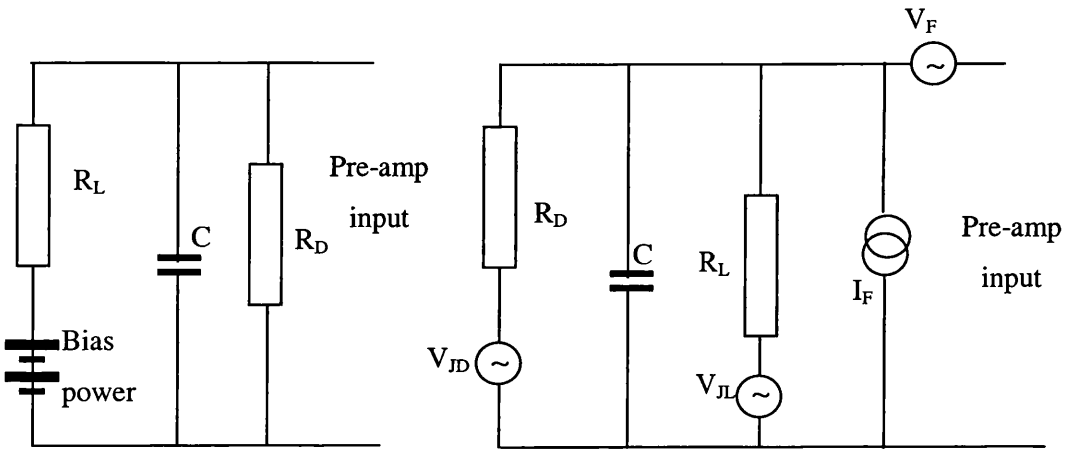

(a) Electrical circuit (b) Noise circuit

Figure 3.2 The experimental detector bias circuit and the associated noise diagram. R_D is the 'detector' resistor and R_L the load resistor. C is the parasitic capacitance in the system. Associated with the detector and load resistors are two Johnson noise sources V_{JD} and V_{JL}. V_F and I_F are the effective pre-amp voltage and current noise sources.

The model of the system transfer characteristics evolved from a series of experiments to map the spectral response of an experimental detector system. The experiments were performed using a circuit based on the standard detector circuit (shown in Figure 2.1), but with the detector replaced by a 30MΩ resistor to eliminate phonon noise and the detector impedance to simplify subsequent analysis. A schematic diagram of the circuit used is shown in figure 3.2. The noise model which was produced assumed that the magnitude of the RMS spread of the Johnson noise generated by the load, V_{JL} , is reduced by attenuation to ground across the potential divider created by R_L, in series with the complex impedance $Z_{\|CRD}$. This impedance is calculated from $Z_C(\omega)$ and R_D in parallel

$$\frac{1}{Z_{\|CRD}} = \frac{1}{R_D} + \frac{1}{Z_C(\omega)} \qquad \text{- 3.4}$$

where $Z_C(\omega)$ is the impedance created by the parasitic capacitance C within the system and given by

$$Z_C(\omega) = \frac{1}{j\omega C} \qquad \text{- 3.5}$$

Similarly, the Johnson noise generated in the detector resistor V_{JD} is reduced across the potential divider created by R_D in series with $Z_{\|CRL}$. This is the impedance generated by the load resistance R_L and the capacitative impedance $Z_c(\omega)$ in parallel.

$$\frac{1}{Z_{\|CRL}} = \frac{1}{R_L} + \frac{1}{Z_C(\omega)} \qquad \text{- 3.6}$$

The experimental system was connected to a JFET preamplifier. So in addition to the Johnson noise in the resistors R_D and R_L, there was a JFET current noise I_F. This created an RMS voltage spread $V_{\|L}$ generated across the load, which was attenuated across a potential divider, created by Rd and the impedance $Z_{\|CRD}$ in parallel. All these noise sources are uncorrelated Gaussian noise, so they can be added in quadrature to give the resultant sum $V_N(\omega)$ of the total RMS spread of noise at the output

$$V_N(\omega) = \sqrt{\left(\left(V_L\left(\frac{(Z_{\|CRD}(\omega))}{(Z_{\|CRD}(\omega))+R_L}\right)\right)^2 + \left(V_{JD}\left(\frac{(Z_{\|CRL}(\omega))}{(Z_{\|CRL}(\omega))+R_D}\right)\right)^2 + V_F^{\,2}\right)} \qquad \text{- 3.7}$$

where V_L is the quadrature sum $\sqrt{((V_{\|L})^2 + (V_{JL})^2)}$ and V_F is the effective voltage noise of the JFET.

A comparison of $V_N(\omega)$ predicted by equation 3.7 with experimental data is shown in figure 3.3. The model of the system fitted the data very well over a wide range of frequencies and heat sink temperatures.

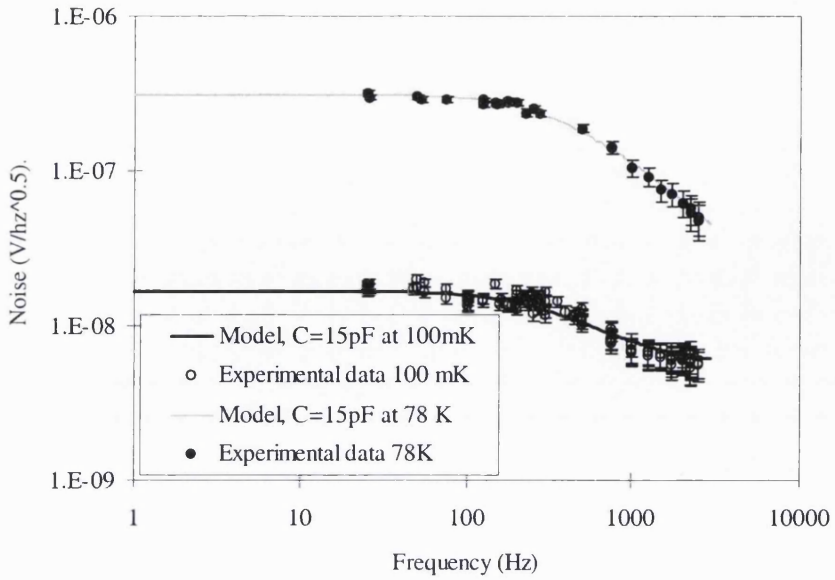

Figure 3.3 A comparison of the spectral noise model with experimental data. For the model V_F=5.6nV/(√Hz), I_F=2.5fA/√Hz, R_L=90MΩ, R_D=30MΩ, C=15pf.

Because the individual noise generators in the experimental system V_{JD}, V_{JL}, V_{IL} and V_F have no intrinsic frequency dependence, the resultant frequency profile of the noise sum $V_N(\omega)$ of the system contains its spectral response. So taking the general form of the noise model it was possible to generate a model of the transfer characteristics of a typical bias circuit. Since zero frequency noise signals $V_N(\omega=0)$ in the system are unattenuated, the frequency response profile of the noise response can be normalised by dividing $V_N(\omega)$ by $V_N(\omega=0)$ to give the frequency response of the bias system i.e. its transfer characteristics.

The approach used to model the transfer characteristics was to take the noise model and remove the frequency independent noise terms V_{IL} V_{JL} V_F and V_{JD}, leaving the functional form of $(V_N(\omega)/V_N(0))$ to give the transfer characteristics $T(\omega)$.

$$T(\omega) = \left(\frac{\sqrt{\left(\left(\frac{\left(Z_{\text{IICRD}}(\omega)\right)}{\left(Z_{\text{IICRD}}(\omega)\right)+R_L} \right)^2 + \left(\frac{\left(Z_{\text{IICRL}}(\omega)\right)}{\left(Z_{\text{IICRL}}(\omega)\right)+R_D} \right)^2 \right)}}{\sqrt{\left(\left(\frac{R_D}{R_D+R_L} \right)^2 + \left(\frac{R_L}{R_L+R_D} \right)^2 \right)}} \right) \quad \text{- 3.8}$$

For comparison of the functional fit T(ω) was compared to the actual profile obtained from ($V_N(\omega)/V_N(\omega=0)$) for all likely microcalorimeter operating regimes and found to be in good agreement. A comparison of ($V_N(\omega)/V_N(\omega=0)$) with equation 3.8 for a typical microcalorimeter is shown in figure 3.4.

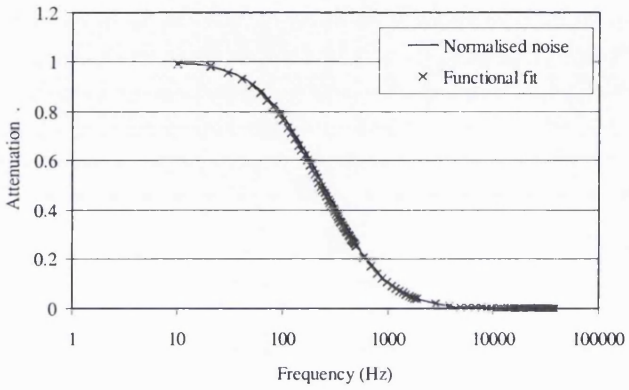

Figure 3.4 A comparison of the normalised noise profile ($V_N(\omega)/V_N(\omega=0)$) and the corresponding functional fit from equation 3.8. Calculated for R_L=240MΩ, R_D=24MΩ, C=16pf at 100mK.

Having found an expression for the general functional form of the transfer characteristics of the circuit in figure 3.2 it can be extended to that of an actual bolometer circuit by replacing R_D with the bolometer impedance Z(ω) in equation 3.8. In doing this we generate a functional form for the transfer characteristics of a microcalorimeter circuit

$$T(\omega)=\left(\frac{\sqrt{\left(\left(\frac{Z_{\|CZ}(\omega)}{Z_{\|CZ}(\omega)+R_L}\right)^2+\left(\frac{Z_{\|CRL}(\omega)}{Z_{\|CRL}(\omega)+Z(\omega)}\right)^2\right)}}{\sqrt{\left(\left(\frac{Z}{Z+R_L}\right)^2+\left(\frac{R_L}{R_L+Z}\right)^2\right)}}\right) \qquad \textbf{- 3.9}$$

Where $Z_{\|CZ}$ (ω) is the impedance of the bolometer and capacitance in parallel

$$\frac{1}{Z_{\|CZ}}=\frac{1}{Z(\omega)}+\frac{1}{Z_C(\omega)} \qquad \textbf{- 3.10}$$

Z is the zero frequency impedance of the microcalorimeter given by equation 2.26.

Now the attenuation of an x-ray induced voltage pulse V(t) generated in the detector bias circuit can be modelled. To do this, the Fourier transform V(f) of an numerically generated discrete x-ray voltage pulse V(t) is calculated. This is multiplied by the transfer characteristics $T(\omega)$ of the detector circuit, as given by equation 3.9, to give an attenuated pulse $V'(f)$ which can be transformed back to the time domain giving the final voltage pulse $V'(t)$ from the detector system.

Computationally, there is an added complication; the form of $T(\omega)$ must be converted into a form consistent with that generated by numerical transforms. From equation 3.9, $T(\omega)$ is a continuous function in frequency ranging from $-\infty$ to $+\infty$. It is Hermitian in nature since the real part is even and the imaginary part odd. When a numerical convolution is performed, it needs to be converted into a discrete function having only +ve frequencies. To do this and retain the Hermitian nature of $T(\omega)$ the cyclic property of a discrete numerical transform is needed to reconstitute the arrays of $T(\omega)$ in a different form. This is achieved by joining the real and imaginary components as follows

$$T(\omega) = [T_{real}(+\omega), T_{real}(-\omega)] + j[T_{imag}(+\omega), T_{imag}(-\omega)] \qquad \textbf{- 3.11}$$

The negative frequency values $T(-\omega)$ are now shifted to the right spectrally by an amount $(2\pi.f_{max}/2)$. As a result $T(\omega)$ now ranges from zero to $(2\pi.f_{max})$. This technique is dealt with in standard Fourier transform texts [61].

3.2.3 Noise model

A model of the noise in the detector system is based on standard bolometer treatment of noise as described in section 2.3.3. Here the standard bolometer noise model is adapted to include the presence of a parasitic capacitance, C, in the noise circuit as shown in figure 3.2. The noise model assumes that the microcalorimeter is in equilibrium at some working temperature, T, as dictated by its load curve position. The phonon voltage noise V_P from equation 2.32 is now also modified by the presence of the parasitic capacitance since the responsivity, $S(\omega)$, given by equation 2.29, is now attenuated by the complex impedance $Z_{\|CRL}$ of the load R_L and parasitic capacitance $Z_c(\omega)$ in parallel.

$$S(\omega) = \frac{\alpha V}{Ge}\left(\frac{(Z_{\text{IICRL}}(\omega))}{(Z_{\text{IICRL}}(\omega)) - Z(\omega)}\right)\left(\frac{1}{\sqrt{1+\omega^2.\tau_e^2}}\right) \qquad \text{- 3.12}$$

This change is incorporated into equation 2.32 to produce a reduced RMS spread of phonon noise created by the additional attenuation across the capacitance. The RMS spread of Johnson noise in the detector resistance, defined by V_{JD} in equation 2.33, is now reduced across the complex impedance Z_{IICRL} produced by the load resistor and the parasitic capacitance in parallel, modifying it to

$$V_{JD} = \sqrt{(4K_B T R_D)}\left(\frac{(Z_{\text{IICRL}})}{(Z_{\text{IICRL}}) + R}\right)\left(\frac{\left(\omega + \frac{1}{j\tau}\right)}{\left(\omega + \frac{1}{j\tau_e}\right)}\right) \qquad \text{- 3.13}$$

In the same manner, the Johnson noise from the load resistor V_{JL} from 2.34 is also reduced by the inclusion of the parasitic capacitance to

$$V_{JL} = \sqrt{(4K_B T_o R_L)}\left(\frac{(Z_{\text{IICZ}})}{(Z_{\text{IICZ}}) + R_L}\right) \qquad \text{- 3.14}$$

where Z_{IICZ} is the impedance of the detector and parasitic capacitance in parallel. The voltage noise, V_C, created by the JFET current noise I_A, given in equation 2.35, is now dropped across Z_{IICZ} giving a reduced RMS spread defined by

$$V_C = I_A R_L\left(\frac{(Z_{\text{IICZ}})}{(Z_{\text{IICZ}}) + R_L}\right) \qquad \text{- 3.15}$$

The JFET voltage noise V_F is added in the preamplifier stage and is unmodified by the presence of the parasitic capacitance. The above equations give the RMS spread of individual noise components in the system. The total at the output of the system $V_{Noise}(\omega)$ is produced by summing the individual terms in quadrature

$$V_{Noise}(\omega) = \sqrt{\left(V_P^2 + V_{JD}^2 + V_{JL}^2 + V_F^2 + V_C^2\right)} \qquad -3.16$$

The resultant summed noise distribution $V_{Noise}(\omega)$ gives the typical RMS noise in the circuit in ($V/\sqrt{Hz}$). It is a Gaussian distribution since all its components are Gaussian, with a mean value of zero. For any Gaussian distribution varying about a mean value of zero, the RMS spread is equivalent to the 1 σ spread [62]. This means the noise sum in equation 3.16 represents the 1 σ envelope of the system over all frequencies and as such gives the magnitude of the typical instantaneous noise excursion. At any instant in time, all frequencies and all components may contribute to the noise. Thus the temporal 1 σ noise is produced by summing $V_{Noise}(\omega)$ over all frequencies. Taking the square of equation 3.16 gives the spectral density in units of (V^2/Hz). Summing the spectral density over all frequencies for small spectral intervals $\delta\omega$ (Hz) produces the final noise sum V_N in Volts [63].

$$V_N = \sqrt{\sum_0^\infty V^2{}_{Noise}(\omega)\delta\omega} \qquad \textbf{- 3.17}$$

Theoretically, this is summed over all frequencies. In practice, the sum is out to 100kHz.

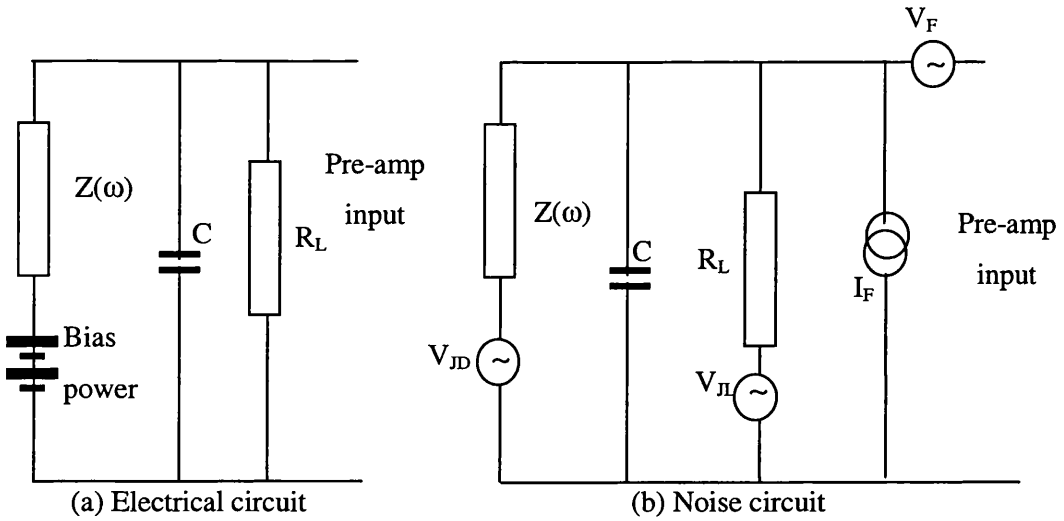

Figure 3.5 The bias and pre-amp electrical circuit and the associated noise diagram. Z(ω) is the detector impedance, R_L the load resistance, C the parasitic capacitance, V_{JD} and V_{JL} are Johnson noise from the detector and load, V_F effective voltage noise from the pre-amp and I_F current noise from the pre-amp.

3.3 System attenuation model

Taking the component sub models (from sections 3.2.1, 3.2.2 and 3.2.3), we can now generate a model capable of estimating the final resolution of the microcalorimeter system subject to the attenuation created by the detector bias and readout circuit. To do this we use the model of the system transfer characteristics to generate the final shunted voltage pulse V′(t) from an initial input pulse V(t) which is calculated by the thermal system model for a given equilibrium temperature. The height of the final pulse is combined with the output from the system noise model, giving the final resolution of the system at a fixed operating temperature. Generating a set of operating temperatures, from the system load curves, we obtain a map of the operational response of the detector system.

3.3.1 Equilibrium State

The equilibrium operating temperatures of a detector are calculated from ideal bolometer theory using the detector's load curve given by equations 2.19 and 2.20. The system parameters (see eqns 2.21-2.29) are then calculated for each load curve point, and used as arguments for the system noise model, the system transfer characteristics model and the pulse model. By sampling the load curve at regular intervals a set of discrete points are generated allowing the signal to noise estimates of these points to be calculated. This creates a map of the detector's response for all load curve points.

3.3.2 Pulse models

There are two ways to model the detector pulse.

- We can assume that the system is not compromised by a non linear heat capacity and use an ideal pulse model. An ideal pulse model assumes that all the x-ray energy is thermalised at once, producing an instantaneous rise in detector temperature, which decays exponentially back to the heat sink temperature.

- We can numerically model the resultant pulse generated in the thermal system by depositing the energy of the x-ray in small increments and reassessing the state of the system at each interval.

3.3.2.1 Ideal pulse

For each load curve point the detector is at some equilibrium temperature, T_{equ}. Using equation 2.36, the temperature profile T(t) of an ideal pulse created by an x-ray of Q Joules is calculated. Assuming a constant bias current during the duration of the pulse, this is converted to a voltage profile V(t) using the detector resistance R(T) to give

$$V(t) = V_o EXP - \left(\frac{t}{\tau_e}\right) \qquad \text{- 3.18}$$

From equation 2.36 the temperature step dT=Q/C(T) produced can be converted into a voltage step if we assume a constant bias current I_b. From equation 2.1 this gives $Vo=I_bR(dT)$ which is the ideal pulse height. This simple model assumes instantaneous thermalisation of the absorbed x-ray. The voltage pulse V(t) is generated over a temporal range of t_{max} seconds in increments of t_{inc} seconds. Consequently the Fourier transform V(f) of the voltage pulse V(t) is generated over a spectral range $1/t_{inc}$ in increments of $1/t_{max}$. The product of $T(\omega)$ and V(f) can then be used to give the attenuated pulse V′(f) in frequency space. Performing an inverse transform on V′(f) will generate the final profile of the attenuated pulse V′(t). In figure 3.6, the effect of system attenuation is demonstrated by showing pulse heights from the attenuated and unattenuated cases at different bias currents.

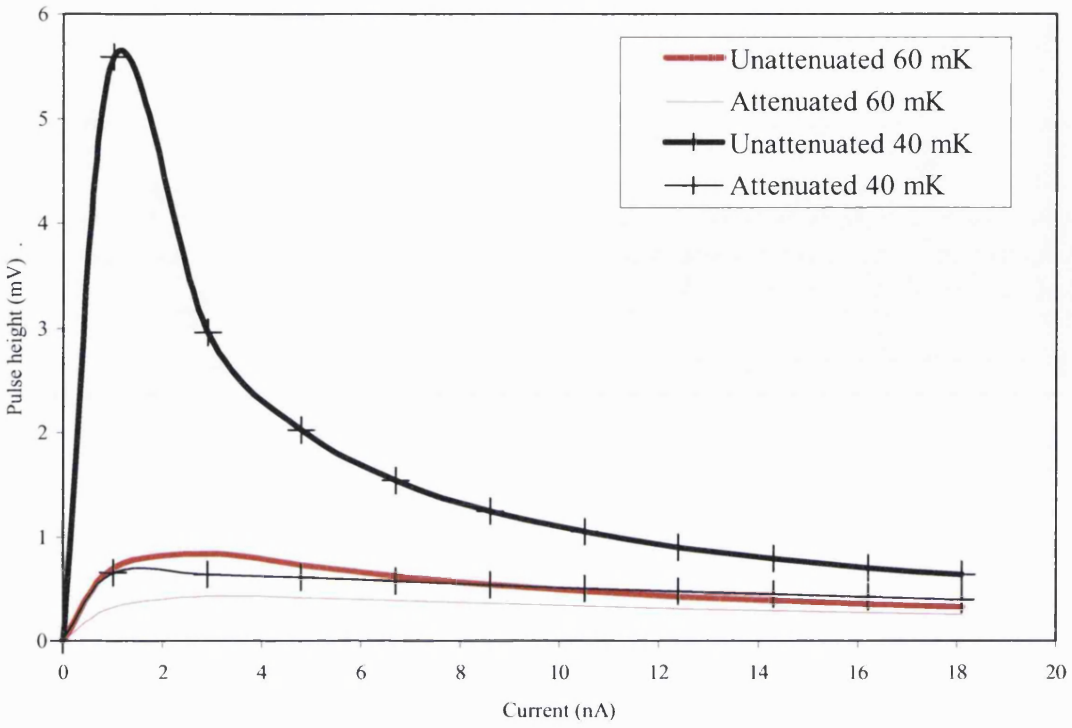

Figure 3.6 The effect of attenuation by the detector system on an x-ray voltage pulse. The data are modelled for a (0.25x0.25x0.25)mm^3 NTD Ge No 17 thermistor with a H_{20} epoxy bonded 0.015x0.5x0.5mm^3 tin absorber and two 8 μm diameter 0.5mm long brass links.

3.3.2.2 Non linear pulse

Using the ideal pulse analysis, the attenuation model is only valid in the small signal regime. From a consideration of figure (2.10) a NTD Ge microcalorimeter, with typical detector dimensions, detecting 1 to 10 keV x-rays, the small signal regime may be regarded as an adequate description of a typical system down to temperatures of 50mK. At temperatures below this, the detector response becomes significantly non-linear. In this temperature regime, a scheme that incorporates the non-linear behaviour within the current model is necessary.

Equation 2.36 assumes that the x-ray thermalisation is instantaneous and defined by the equilibrium values of the system. In reality, this is not the case, x-ray thermalisation is finite and all points of the pulse are governed by the dynamic values of the thermal system at that

instant. To model this, we assume a quasi-dynamic temperature, $T_{(n)}$, constant over small time intervals dt, such that at the end of dt the temperature is given by

$$T_{(n+1)} = T_{(n)} + dT_{(n+1)} \qquad \textbf{- 3.19}$$

where $T_{(n)}$ is the temperature of the end of the previous dt. The temperature change $dT_{(n+1)}$ during the current dt is defined by

$$dT_{(n+1)} = \frac{\left(I_b^2.R(T_{(n)}) - W(T_{(n)})\right)dt + dQ}{C(T_{(n)})} \qquad \textbf{- 3.20}$$

where $(I_b)^2R(T_{(n)})$ is the bias power, $R(T_{(n)})$ the detector resistance, $W(T_{(n)})$ the thermal power to the heat sink, $C(T_{(n)})$ the heat capacity and dQ the absorbed external power during dt. By setting the initial temperature to the equilibrium load curve temperature, T_e, and numerically solving equations 3.19 and 3.20 in succession, the temperature profile of an x-ray pulse may be generated.

To do this the pulse is modelled in two temporal parts.

1) An x-ray of energy Q Joules is absorbed in a period t_{abs}, the absorption time.
2) The detector temperature returns to the equilibrium temperature in a time t_{fall}.

The reason for modelling the pulse in two temporal parts is the large difference in time scales of these two events, typically 3-4 orders of magnitude.

To incorporate a varying heat capacity into the photon absorption phase, the photon is assumed to be absorbed in N_{abs} discrete intervals each of length $dt = (t_{abs} / N_{abs})$, each allowing an energy $dQ = Q/N_{abs}$ to be absorbed. When t_{abs} is reached all of the photon energy has been thermalised, producing a temperature, T_{abs}, above the equilibrium temperature. For the decay period, t_{fall}, dQ is set to zero and the system allowed to decay in N_{fall} intervals each of length $dt = (t_{fall}/N_{fall})$. The thermal pulse is then converted into a voltage pulse V(t) using equation 2.1 assuming a constant bias current. Care must be taken when generating the temperature pulse so that the increments and range correspond with the numerical model of $T(\omega)$ from equation 3.11. More explicitly an integer number of absorption intervals are set equivalent to a fall interval defining the maximum Fourier transform frequency f_{max} as $t_{fall}=1/f_{max}$. The entire pulse period is set by the frequency interval of the Fourier transform $(t_{abs}+t_{fall})=f_{int}$.

Figure 3.7 shows the comparative effects of the different pulse models for the same case.

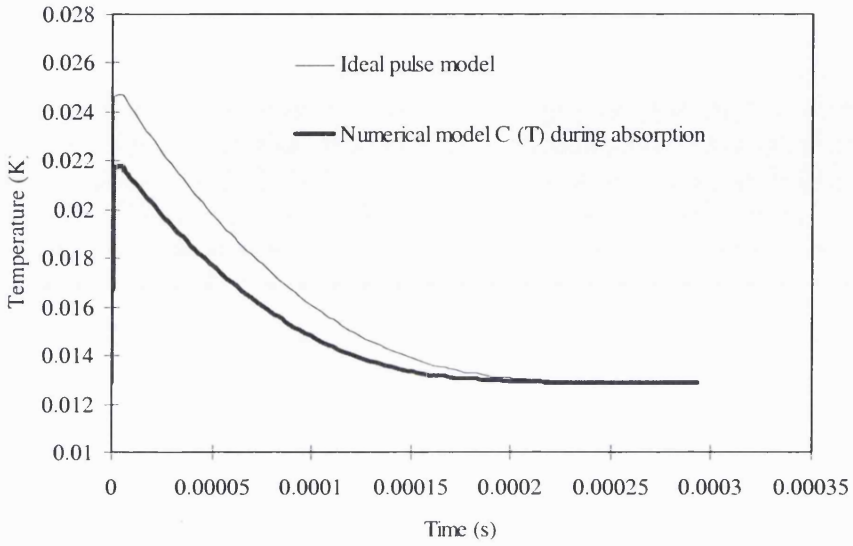

Figure 3.7 A comparison of an ideal pulse with a numerical pulse from the system thermal model. One assumes instant thermalisation ($C(T_e)$ C is fixed at T_e) the other models the non-linear effect ($C(T_{(n)})$ C variable during the pulse). The pulse is for a 0.25mm^3 NTD Ge thermistor with a 0.015 thick 0.5 mm^2 Sn absorber. The thermal links were two 8μm ∅ 0.5mm long brass wires. The pulse is for 10keV x-ray. With T_e=12.85mK and T_o=10mK.

The non-linear pulse model does not address all the non-linearities created by the rapid increase in temperature and the corresponding drop in resistance during a x-ray event. There are four significant effects on the system

1. The attenuation of the pulse is reduced.
2. The noise is reduced.
3. The detector responsivity is decreased.
4. The heat capacity increased.

The pulse model only incorporates 3 and 4. However 1 and 2 conspire to increase the signal to noise of the system whilst the 3 an 4 reduce it. Therefore, the non-linear pulse effectively models the worst resolution attainable by the system.

3.4 Electric field model

For temperatures below 300mK, the effect of the electric field across the detector on the resolution of the system needs to be added to the attenuation model. The origin of the electric field effect is explained in section 2.431. Here the non-linear attenuation model described in the last section is adapted to include the electric field effect.

3.4.1 Load curve modified by the electric field

To include the presence of the electric field effect, the basic form of detector resistance R(T), given in equation 2.1, has to be replaced with R(E,T) given in equation 2.40. This equation incorporates the effect of the electric field on the detector resistance. We see the field is dependent on the resistance, since the field across a detector of thickness, d, is given by E=(V/d), where V is the voltage across the detector. For a constant bias current, I_b, the electric field across the detector is restated as $E = I_b R(E,T)/d$. Equation 2.40 needs to be solved iteratively. The iteration is performed as follows

$$R_{(n+1)} = R(T)EXP\left(\frac{-eI_b LR_{(n)}}{dK_B T}\right) \qquad \text{- 3.21}$$

where $R_{(n)}$ is the estimate preceding $R_{(n+1)}$. The iteration is begun using the equilibrium value of the field E by setting $R_{(n=0)}$ to the equilibrium value given by R(T). The process is repeated until $R_{(n+1)}=R_{(n)}$. Typically, a solution is found within 7-8 iterations. When this process is incorporated into equations 2.19 and 2.20, to generate the detector load curve, it has the effect of suppressing it as shown in figure 3.8. As the hopping length L_O is increased (the level of doping is decreased) the detector becomes more susceptible to the effect of the field and it is suppressed further.

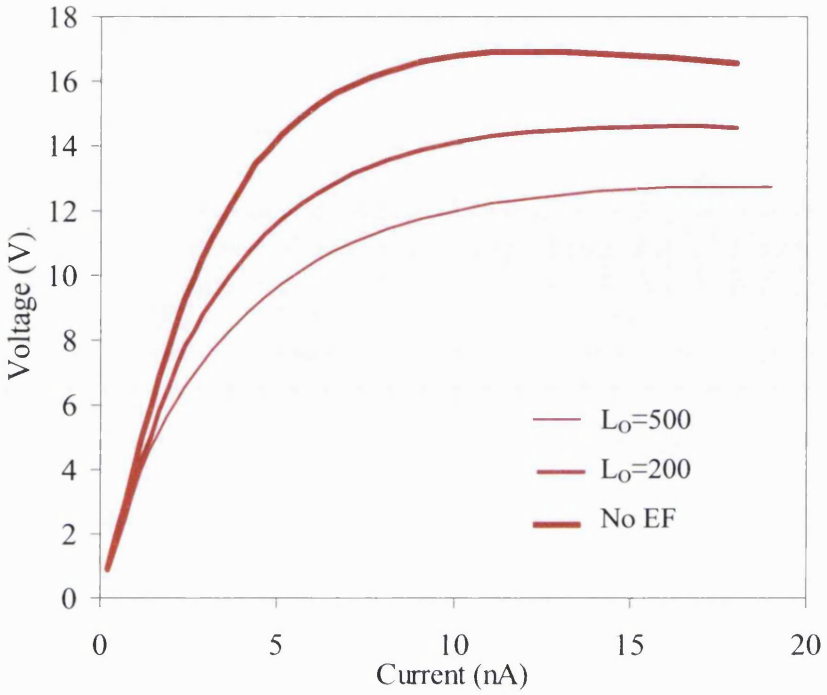

Figure 3.8 Load curves modified by the presence of the electric field for varying hopping lengths L_O given in Å. The parameters defining the system are given in tables 3.1 and 3.2.

Because the detector load curve is offset from the ideal case (the top curve on figure 3.8), a new set of equilibrium points is defined for the detector. The resistance has changed and the thermal coefficient of resistance, α, given by equation 2.21 is redefined as

$$\alpha = \frac{1}{R(T)}\frac{dR}{dT} = -\frac{1}{2}\left(\frac{T_g^{1/2}}{T^{3/2}}\right) - \frac{eEL}{K_B T^2} \qquad \text{- 3.22}$$

This equation shows the additional effect of the field in the RH term. We see that if the E field is neglected (i.e. E is set to zero), α returns to its standard value as given in equation 2.21. This change in α is propagated through all subsequent load curve parameters in equations 2.22 to 2.29. In the model, this happens implicitly, since α is calculated from slopes of the resistance and temperature arrays used to generate to create the load curve.

3.4.2 Pulse model including the electric field effect

A full inclusion of the electric field needs to address how it modifies the pulse profile generated by an x-ray event. The electric field model assumes a common temperature for all the detector components. This means that the non-linear thermal pulse model, as described in section 3.3.2.2, does not need to be significantly altered. To include the effect of the electric field we replace R(T) by R(E,T) and must now iteratively solve R(E,T) for each period dt defined in equation 3.20. This produces a modified thermal pulse which can be converted to an initial voltage pulse V(t) using R(E,T). This voltage pulse is then convoluted with the system response T(ω) to produce the final attenuated pulse V′(t). The effect of the field alone can be seen by comparing the unattenuated pulses, modelled for different hopping lengths L_O, at a fixed bias current. An example of this is shown in figure 3.9, where we see that the inclusion of the electric field reduces the voltage pulse produced by an x-ray. In addition, we see as L_O increases, the field produces a greater reduction in pulse height. This shows that the lightly doped NTD Ge crystals are more susceptible to the influence of electric fields.

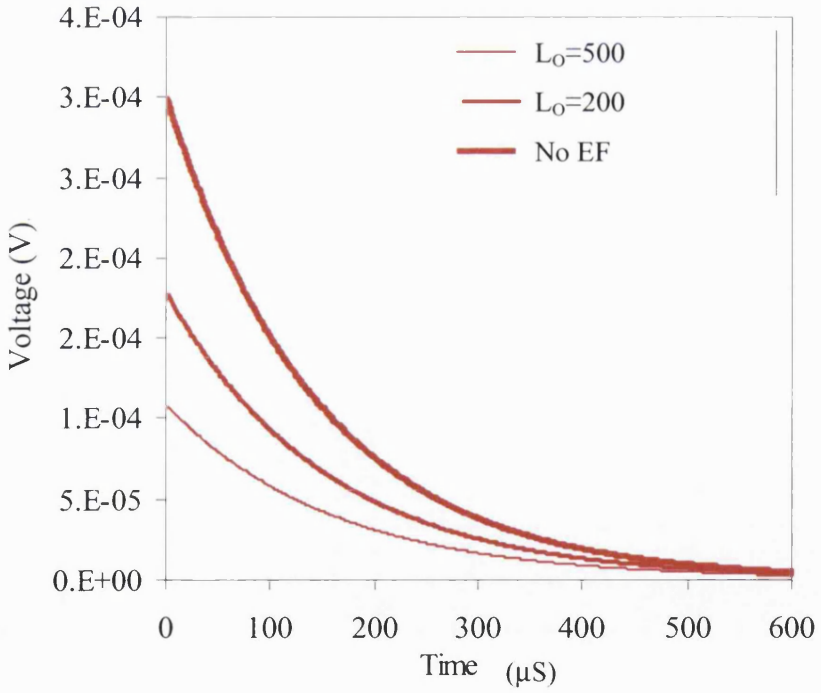

Figure 3.9 The simulated effect of the electric field on an x-ray induced pulse for varying hopping lengths L_O in Å. The parameters defining the system are given in tables 3.1 and 3.2.

3.4.3 Noise model modified by the electric field

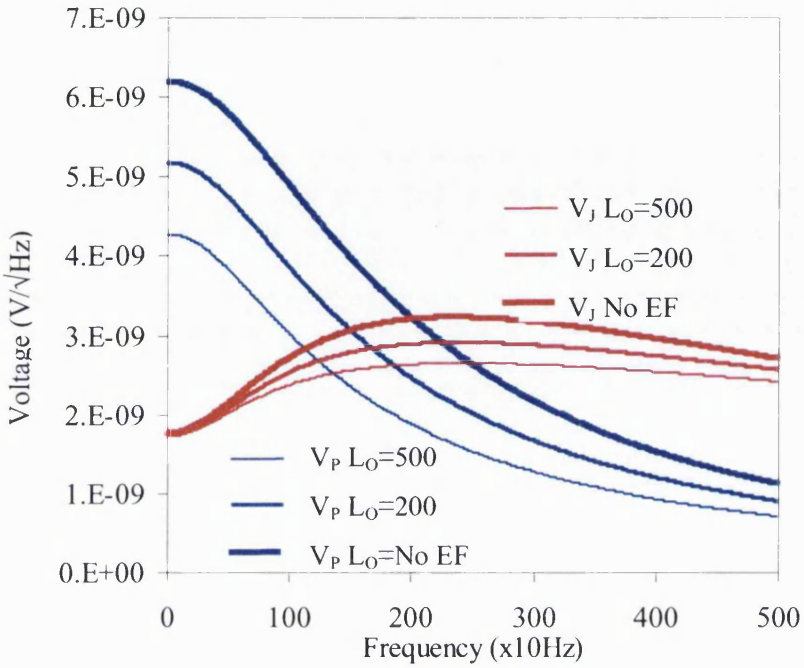

Figure 3.10 The modelled effect of the electric field on the detector Johnson and phonon noise for varying hopping lengths L_O in Å. The parameters defining the system are given in tables 3.1 and 3.2.

In addition to modifying the voltage pulses, the electric field also modifies the noise levels in the system. The normal noise model, calculated for the equilibrium state of the system, is still a good representation. The reason for this is although the electric field changes the bias position of the detector it does not introduce any dynamic effects, which cannot be modelled using small signal bolometer noise analysis. The modified equilibrium noise estimate can then be calculated by feeding the modified parameters R(E,T), α, $Z(\omega)$ and $S(\omega)$ for each load curve point into the standard noise model defined in section 3.2.3., implicitly incorporating the effect of the electric field into the system noise. An example of the noise calculated by doing this is shown in figure 3.10, which plots the phonon noise and Johnson noise, calculated for a fixed bias current, with hopping length. As the hopping length increases it has the effect of decreasing the noise voltage.

3.4.4 Effect on signal to noise estimate

The signal to noise ratio obtained using the modified models in section 3.4.2 and 3.4.3 is reduced by the presence of the field. The reduction in signal to noise is inversely proportional

to the hopping length. The implication is that more heavily doped crystals will be less affected by the electric field, as they have an inherently shorter hopping length.

3.5 Electron-phonon decoupling model

As shown in section 2.4.3.2, to reliably predict the performance of NTD Ge below 100mK, electron-phonon decoupling must be included. In this section, the modifications necessary to include electron-phonon decoupling in the standard attenuation model are described.

3.5.1 Modified thermal system

Electron-phonon decoupling can be included by modifying the standard thermal model of the detector system described in section 3.3.2.2. The modifications are based on the electron-phonon decoupling model developed by Wang and presented in section 2.4.3.2. In the standard decoupling model the presence of the electron-phonon decoupling is modelled by separating the heat capacity C(T) into lattice and electron components, $C_L(T)$ and $C_E(T)$, respectively and introducing a finite conductance G_{ep} between them.

To model a microcalorimeter during an x-ray event this scheme needs to be changed as shown in figure 3.11. As the thermistor is a composite device, the relationship of the decoupled electrons to the rest of the detector needs to be established. The simplest way to achieve this is to assume that the thermistor phonons are closely coupled and in thermal equilibrium with all other components of the detector, excluding the electrons in the thermistor. In the detector, the electron population will have some heat capacity $C_E(T_e)$, that is held at a temperature T_e above the rest of the detector (temperature T, heat capacity $C_{Rest}(T)$), by the bias power $I_b^2R(T_e)$. As in Wang's model, the components are linked with a conductance G_{ep} resulting in a thermal power $W_{ep}(T_e-T)$ flowing from the electrons to the rest of the detector. The thermal power $W(T-T_O)$ flowing to the heat sink at a temperature T_O is the same as that in the normal model of section 3.3.2.2, defined by the dynamic conductivity of the thermal link G_d (equation 2.22). The resistance is now a function of the electron temperature only, and given by equation 2.42. The heat capacity of the electron component $C_E(T_e)$ is defined as

$$C_E(T_e) = \left(vol_{Cryst}.b_{Cryst}\right).T_e \qquad \text{- 3.23}$$

where vol_{Cryst} is the volume of the thermistor crystal in cm^3 and b_{Cryst} is its electron coefficient in $J/K^2/cm^3$ for the electron component. Now the bulk heat capacity of the entire detector $C_{Bulk}(T,T_e)$ is a function of the temperature of the electrons T_e and the temperature of the rest of the detector T. This is given by

$$C_{Bulk}(T)=C_{Rest}(T)+C_E(T_e) \qquad \text{- 3.24}$$

As $G_{ep} \rightarrow \infty$ the electron temperature $T_e \rightarrow T$ and the thermal model reverts to the standard model presented in section 3.21.

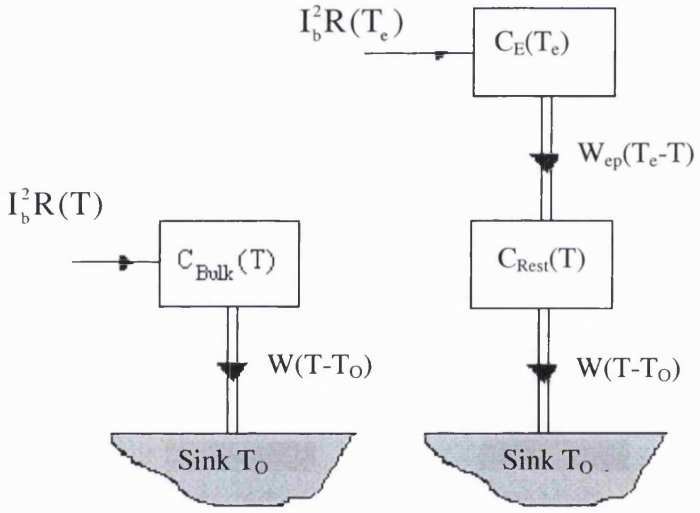

Figure 3.11 A schematic showing the modifications to the standard thermal model (right) to include electron-phonon decoupling (left). $I_b^2R(T)$ is the bias power, $C_{Bulk}(T)$ compound heat capacity, C_{Rest} the compound heat capacity excluding the electron component of the thermistor, $C_E(T)$ the heat capacity of the thermistor electron component, $W_{ep}(T_e-T)$ the power flowing from the electrons to the rest of the detectors, $W(T-T_o)$ the thermal power flowing to the heat sink at T_o.

3.5.2 Decoupled equilibrium points

To incorporate decoupling into the load curve models, the equilibrium condition $(I_b)^2R(T_e)=W_{ep}=W$ is assumed and used to generate the load curve consistent with equations 2.19 and 2.20. Each point on the load curve now has equilibrium temperatures T_e and T for each component. The effect of having a decoupled electron and phonon population in the model is shown in figure 3.12.

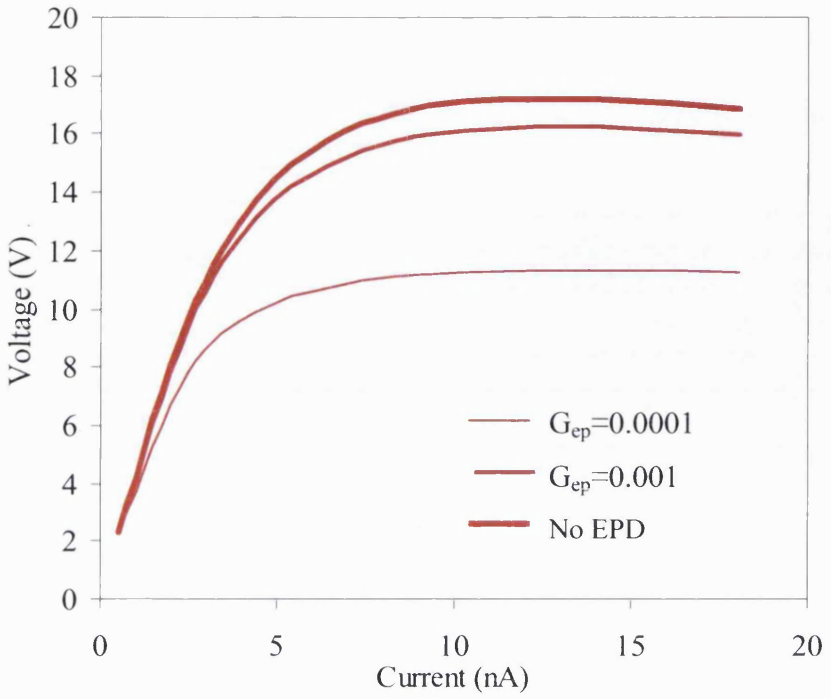

Figure 3.12 The simulated effect of including differing levels of electron-phonon decoupling in a detector VI model. The level of decoupling is increased, by decreasing the conductance G_{ep} between the electrons and phonons. The parameters defining the system are given in tables 3.1 and 3.2. G_{ep} is in $(W/k^{(\alpha'+1)})$, and $\alpha'=5$.

The presence of electron-phonon decoupling flattens the detector load curve, since now the equilibrium detector resistance $R(T_e)$ is a function of the equilibrium temperature of the electrons, which is above the equilibrium temperature of the rest of the detector. As the level of decoupling is increased, the temperature of the electrons increases more and suppresses the VI further.

By manipulating equation 2.41 the relationship between the temperature of the electrons and the temperature of the phonons can be found. For consistency with the standard attenuation model, we must replace the temperature of the phonons T_p with a common temperature T representing the entire detector. The thermistor electron temperature T_e is related to this by the following relationship

$$T_e = \left(\frac{W_{EP}}{G_{EP}} + T^{(\alpha'+1)} \right)^{\left(\frac{1}{\alpha'+1}\right)} \qquad \text{- 3.25}$$

It is important to know the relationship between these temperatures since any external signal is absorbed in the component defined by the heat capacity $C_{Rest}(T)$. It is necessary to know how the resistance $R(T_e)$ responds to changes in the bulk temperature T, not T_e. We can redefine $R(T_e)$ in terms of R(T). As in the electric field model, we use this to find the change in the temperature coefficient of resistance, α, as a function of the bulk detector temperature, T, created by incorporating decoupling into the model. Mathematically α is redefined as

$$\alpha = \frac{1}{R(T_e)}\frac{dR}{dT} = -\frac{1}{2}\left(\frac{T_g^{1/2}}{T_e^{3/2}}\right)\left(\frac{T}{T_e}\right)^{\alpha'} \qquad \text{- 3.26}$$

Here the RHS of this equation shows that as T_e approaches T, the conditions for decoupling are removed, and α reverts to its normal form given by 2.21. The new α and $R(T_e)$ modify the effective conductance G_e, the impedance $Z(\omega)$ and the responsivity $S(\omega)$ for each load curve point. This is done implicitly in the model by calculating α numerically from the modified resistance and temperature arrays, which are generated to create the load curve.

3.5.3 Decoupled pulse model

The voltage pulse produced by the absorption of an x-ray must be remodelled to include the electrons as a separate component. To achieve this, the thermal system during the absorption of an x-ray must now be modelled as a two component system. The temperature of the electron component $T_{e(n+1)}$ at the end of some interval dt is dependent on the temperature at the end of the previous interval $T_{e(n)}$ and the change $dT_{e(n+1)}$ during the current period, using the following relationship

$$T_{e(n+1)} = T_{e(n)} + dT_{e(n+1)} \qquad \text{- 3.27}$$

The temperature change $dT_{e(n+1)}$ in the electron heat capacity $C_E(T_{e(n)})$ is given by

$$dT_{e(n+1)} = \frac{\left(I_b^2 R(T_{e(n)}) - W_{ep}(T_{e(n)} - T_{(n)})\right)dt}{C_E(T_{e(n)})} \qquad \text{- 3.28}$$

This is defined by the bias power $I_b^2R(T_{e(n)})$ deposited in the electron population and the power flowing to the rest of the detector $W_{ep}(T_{e(n)}-T_{(n)})$. Similarly, the temperature of the rest of the detector T_{n+1} at the end of some interval dt is dependent on the temperature at the end of the previous interval T_n and the change $dT_{(n+1)}$ during the current period via

$$T_{(n+1)} = T_{(n)} + dT_{(n+1)} \qquad \text{- 3.29}$$

where the temperature change $dT_{(n+1)}$ in the component $C_{Rest}(T_{(n)})$ during the interval dt is

$$dT_{(n+1)} = \frac{\left(W_{ep}\left(T_{e(n)} - T_{(n)}\right) - W(T_{(n)} - T_o)\right)dt + dQ}{C_{Rest}\left(T_{(n)}\right)} \qquad \text{- 3.30}$$

This temperature change is governed by the power flowing into the element from the electron population $W_{ep}(T_{e(n)}-T_{(n)})$, the external power dQ absorbed during that interval dt and the power flowing out to the heat sink $W(T-T_o)$. When a photon of energy Q is absorbed and thermalised in the absorber, it produces a temperature rise $Q/C_{Rest}(T)$ in the component $C_{Rest}(T)$. To account for a varying heat capacity during the photon absorption the photon is assumed to be absorbed in N_{abs} discrete intervals each of length $dt = (t_{abs} / N_{abs})$; in each of these a power Q/N_{abs} is deposited in the component $C_{Rest}(T_{(n)})$. The induced temperature rise reduces the thermal power $W_{ep}(T_e - T)$ flowing from the electron population to the rest of the detector causing a rise in the temperature of the electrons, $dTe_{(n)}$. When t_{abs} is reached, all the photon energy Q is absorbed, and the system is then allowed to decay back to equilibrium over N_{fall} successive intervals covering a period $t_{fall}=N_{fall}.dt_{fall}$.

The thermal profile of the pulse produced in the electron population can be generated by successively solving these equations. Using $R(T_e)$, the temperature spike in T_e created by the photon absorption can be converted into an unattenuated voltage pulse V(t) by assuming constant bias current I_b and using equation 2.42. V(t) can then be convoluted in the normal manner with the transfer characteristics, to produce the final attenuated decoupled pulse V′(t). The effect of decoupling on the unattenuated pulses, V(t), is illustrated in figure 3.13. It can be seen how the finite conductance between the electrons and phonons imposes a rise time on the temperature of the sense component, the electrons. This is because of the time taken for a temperature change in the rest of the detector to be registered in the electron population. This rise time reduces the height of the final pulse, and as the conductance between the electrons and phonons is reduced, the reduction in pulse height is increased.

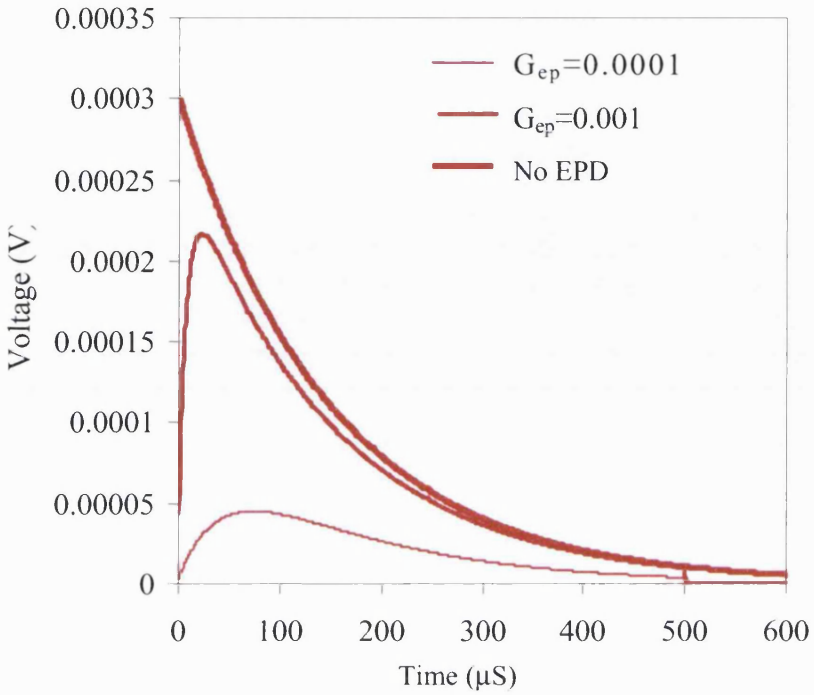

Figure 3.13 The effect of electron-phonon de coupling on an x-ray induced pulse for increasing levels of decoupling. The parameters defining the system are given in tables 3.1 and 3.2. G_{ep} is in (W/k^6), and $\alpha'=5$.

3.5.4 Decoupled noise model

In the case of the electric field noise model, the equilibrium noise estimates of the system were changed because the load curve had changed. This also happens in the electron-phonon decoupling case. The modified parameters for $R(T_e)$,α, $Z(\omega)$ and $S(\omega)$ for each load curve point are put into the standard noise model defined in section 3.2.3. An example of the effect of decoupling on the system noise is shown in figure 3.14. Here the Johnson and phonon noise for different decoupling levels at a constant bias current are shown. As the decoupling increases, the Johnson noise V_J at a load curve points decreases. This is due to the reduced detector resistance imposed by the higher electron temperatures. Correspondingly, the increased temperature of the electrons reduces the responsivity of the detector, thus reducing the level of phonon noise V_P. As decoupling decreases, the model reverts to the standard noise levels.

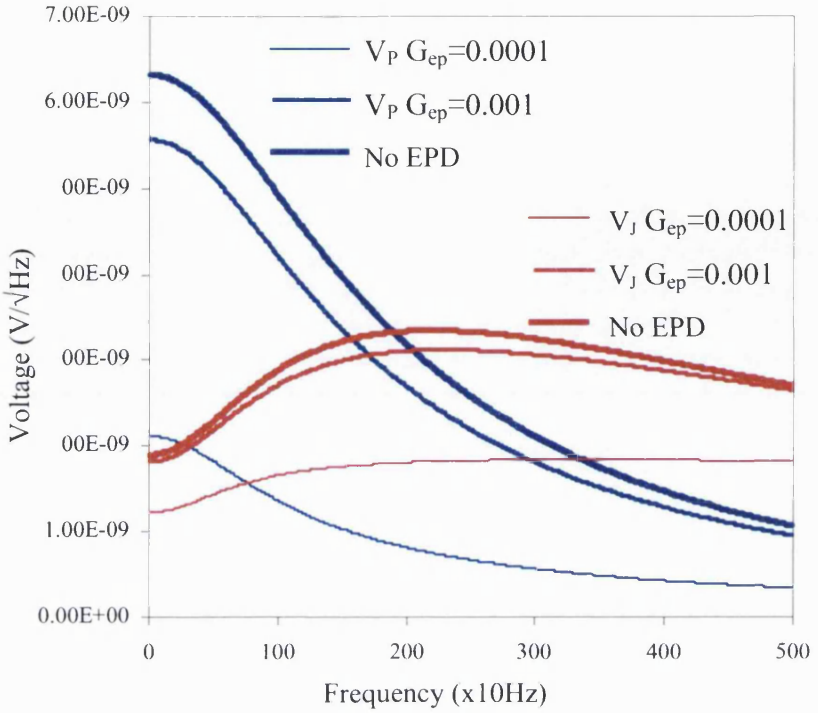

Figure 3.14 The simulated effect of electron-phonon decoupling on the system noise for varying levels of decoupling. The parameters defining the system are given in tables 3.1 and 3.2. G_{ep} is in (W/k^6), and α'=5.

3.6 Comparison of modelling with experiment.

The predictions of the different models were compared with the results from a series of experiments undertaken with a real microcalorimeter system. The intention was to use the experiments to address the accuracy of the numerical models.

3.6.1 Experiment details

An experimental NTD Ge detector was constructed in a standard format as shown in figure 3.15. It consisted of No17 NTD Ge (the nomenclature is explained in figure 2.5 and table 2.1) thermistor bonded to a $0.5mm^2$ 0.115mm thick tin absorber with H_{20} epoxy. H_{20} is silver filled epoxy commonly used in the construction of bolometers and microcalorimeters, because it provides a good electrical and thermal contact. The doping level of NTD Ge No17 (figure 2.5) gives a good responsivity and resistance for operating temperatures in the region of 80 to 110 mK, close to the base temperature of the Adiabatic Demagnetisation Refrigerator (ADR). The thermal links used were two 8μm ∅, 1.5mm long brass wires also bonded with H_{20} epoxy. Details of the detector dimensions are given in table 3.1, which presents the modelled parameters. During the tests, the detector was enclosed in a small housing that had a single aperture, see figure 3.15. The aperture was covered with three layers of MLI to minimise the amount of radiant background power on the detector whilst still transmitting a reasonable x-ray flux.

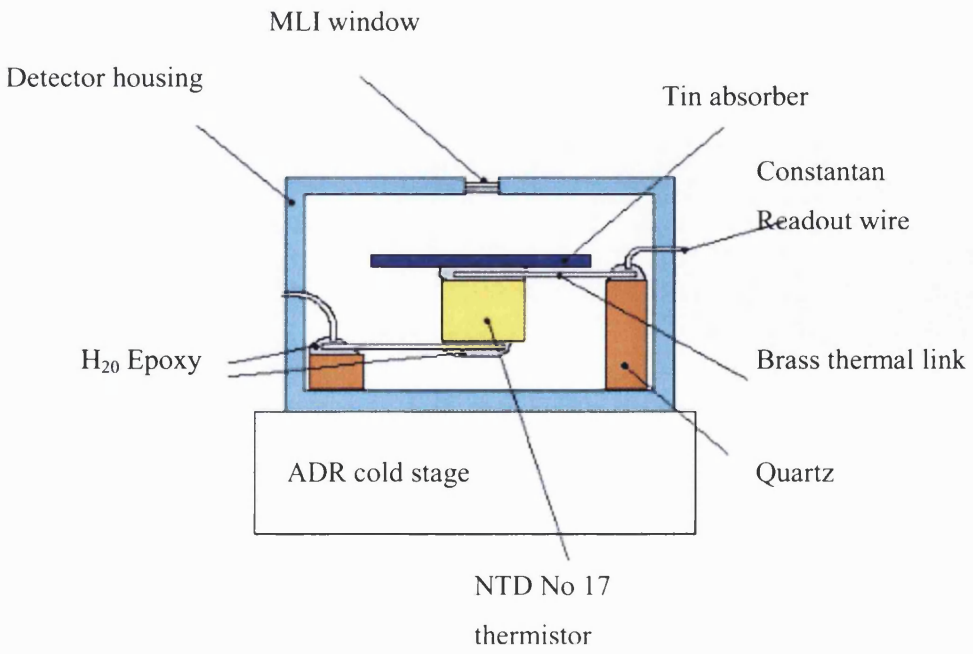

Figure 3.15 Schematic of the experimental detector in its housing.

The experiment was performed in an ADR capable of attaining temperatures down to 40mK. The temperature of the cold stage was measured using a RuO resistive thermometer. The detector was biased using a 120MΩ Nichrome resistor. The readout from the detector was taken from the housing via Constantan wires to a warm JFET pre-amp stage at 110K and from there to a final room temperature low impedance AC amplifier. The estimated capacitance of the bias system was ~ 16pF. X-ray data were obtained by illuminating the housing aperture with 5.89keV x-rays.

3.6.2 Experimental conditions.

During the experiments, two complicating factors were evident. The detector was subject to considerable background power loading during the tests and the system was susceptible to microphonic noise, which created an undulating DC baseline. These effects could not be eliminated during the tests, however it still proved possible to acquire useful data of the system response.

3.6.2.1 Background power

The presence of background power during the experiments is evident from the comparative load curves shown in figure 3.16, which were taken during the tests. Both were taken with the cold stage at 100mK; one in the presence of a 4.2K He bath and the other in the presence of a 1.6K He bath. The different bath temperatures create different power loading conditions on the detector. If the detector is properly shielded from stray radiation, then the detector response should be the same in both cases. From both the VI curves in figure 1.6 this was not the case during the experiment. Several shielding methods were tried, for example taping all the visible joints of the detector housing with Al tape, putting graphite loaded resin between all joints, but it proved impossible to fully eliminate the background power. This greatly complicated the subsequent modelling as it was not possible to measure R_o and T_g for each crystal directly by observing R(T). This is because the cold stage temperature T is not indicative of the detector temperature due to the loading.

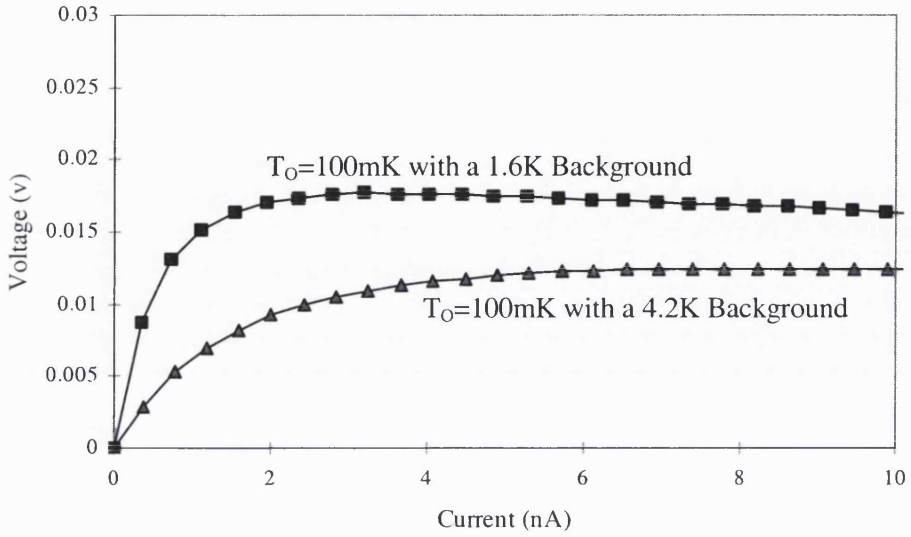

Figure 3.16 The effect of power loading on the experimental detector.

Ideally the values of R_o and T_g should be measured for each NTD Ge crystal, because it has been observed that crystals can have values different from those expected [58,60] (figure 2.5). However, we can make some estimate of the likely power on the detector. From the VI plot, the power difference between the curves can be estimated by assuming a constant bias current. This gives a power difference of 38pW power difference. We can use this to estimate the residual power loading in the 1.6K background as follows.

The frequency of radiation from a black body some temperature T will have a characteristic frequency υ giving a typical photon energy of $h\upsilon=k_BT$ where h, k_B are Planck's and Boltzmann's constants respectively. For the detector operating conditions T_1 = 1.6K and T_2=4.2K this yields characteristic photon energies of $dE_1=2.55x10^{-23}$J and $dE_2=5.63x10^{-23}$J. If it is then assumed that the number density N of photons in each case remains constant $N(dE_1)=N(dE_2)$ i.e. the change in power incident on the detector (38pW) is solely attributable to the change in photon energy. The unit flux of photons incident on the detector is given by $N=dP_{(1.6->4.2)}/(dE_1-dE_2)$. A flux of $1.23x10^{12}$photons/s is calculated for this case. Since N is now known, the power reaching the detector N.dE is estimated to be ~69pW for the 4.2K case and ~31pW for the 1.6K case. These values can now be used in the models to simulate the experimental power loading.

3.6.2.2 **Baseline noise**

During the experiments, an additional problem was noted: the baseline was unstable and tended to undulate as seen in figure 3.17. The origin of the undulation appeared to be microphonic and might have been due to detector instability, making it susceptible to low frequency vibrations, or due to resonant vibrations induced in the readout wires. It was not possible to identify the source of the vibrations and eliminate them during the experimental runs. This adds a noise term to the x-ray data.

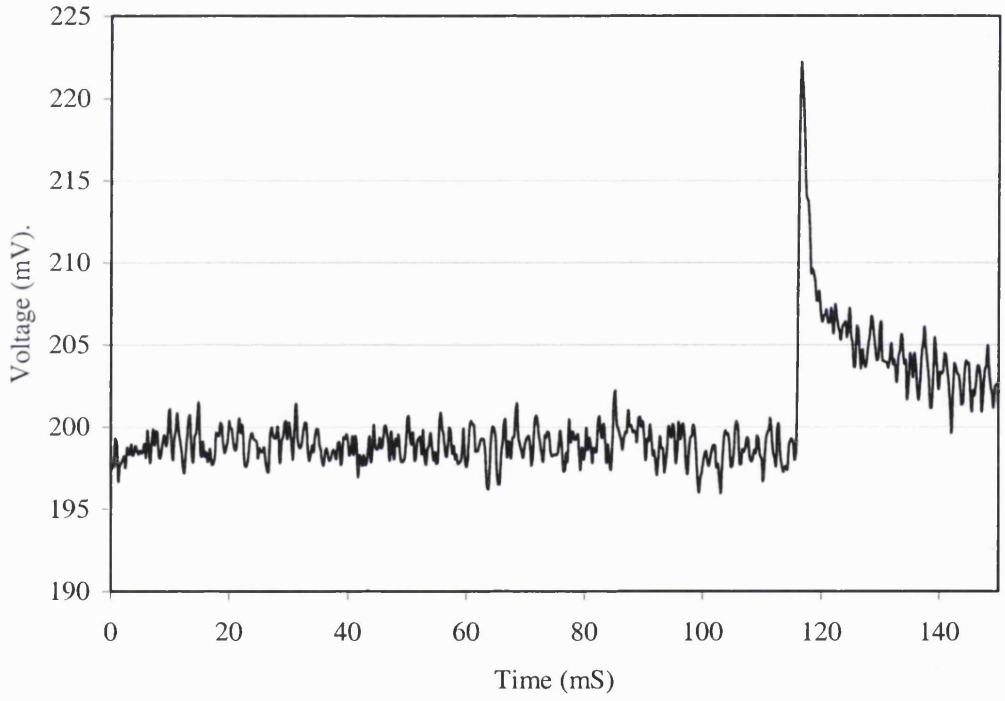

Figure 3.17 An experimental pulse captured in the presence of an undulating baseline.

3.6.3 Experimental results

During the experiment, load curves were recorded for the detector at 50mK, 70mK and 100mK. These are shown in figure 3.18. The system response was also measured at the same heat sink temperatures. This was achieved by capturing a number of x-ray pulses (typically 6-10) at five different bias currents. The bias currents chosen were ~ 0.5, 1.0, 3.0, 6.0, 9.0nA. The maximum pulse heights were then averaged to obtain an estimate of the mean pulse height of the system for each load curve position. The standard deviation of pre-pulse baselines was used to estimate the 1σ voltage noise of the system at that load curve point. Combining these, the signal to noise response of the experimental system was estimated. This is shown in figure 3.19.

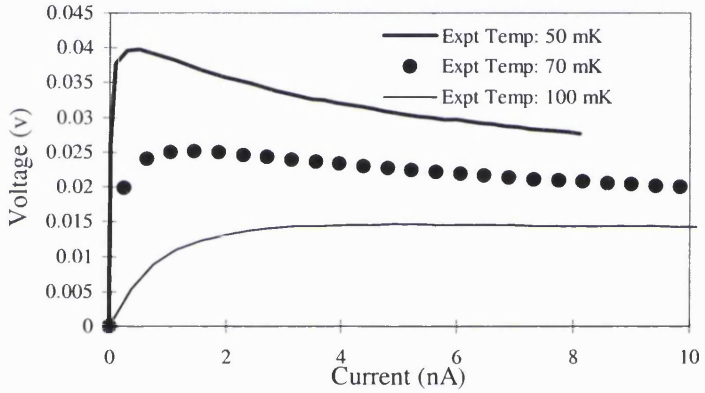

Figure 3.18 VI curves from the experimental detector

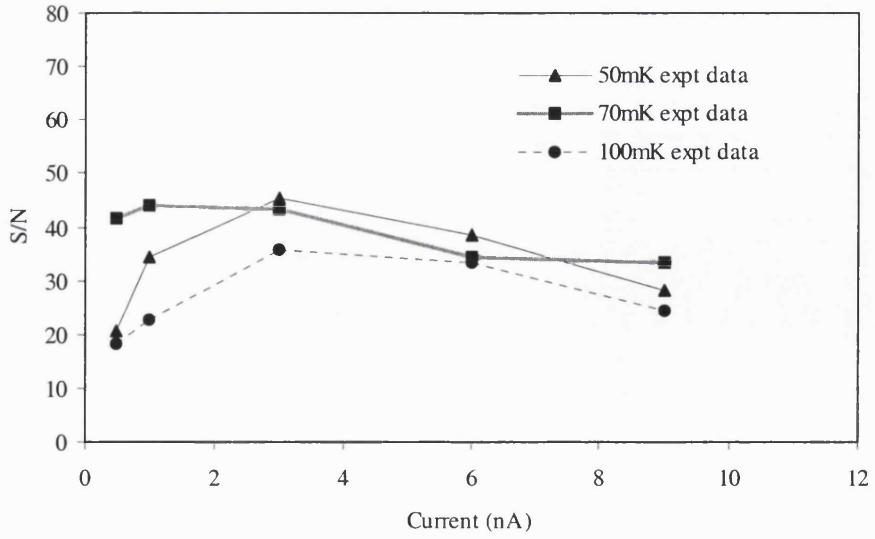

Figure 3.19 The experimentally obtained signal to noise response of the system.

3.6.4 Modelling the experimental system

The response of the experimental detector system was modelled for the non-linear model (section 3.3.2.2), E-field model (section 3.4) and the EP decoupling model (section 3.5). For these simulations, the values of the experimental system presented in tables 3.1 and 3.2 were used. The heat capacity fits for all the materials of the detector components were obtained from published sources [64,65,66]. The values for α' and L_O are taken from reference [42].

COMPONENT	DIMENSIONS (mm)
NTD Ge No17 Crystal (x1)	(0.25x0.25x0.25)
Palladium (x2)	(0.25x0.25x0.00002)
Gold (x2)	(0.25x0.25x0.0004)
Boron ion layer (x2)	(0.25x0.25x0.001)
tin absorber (x1)	(0.50x0.50x0.015)
H_{20} Epoxy (x2)	(0.04x0.04x0.04)
brass wire (x2)	Radius=0.004, Length=1.5

Table 3.1 Dimensions of the detector components

GENERAL MODEL PARAMETERS		
PARAMETER	VALUE	UNITS
General		
brass wire		
β	1	
K_o/T_o^{β}	0.648	(W/K)
(NTD Ge NO 17)		
* T_g	34	K
* ρ_o	0.014	Ω.cm
Capacitance	16.5	pF
Load resistance	240	MΩ
x-ray signal	5989	eV
Fet voltage noise V_F	5.7	nV/√Hz
Fet current noise I_F	2.5	fA/√Hz
Background power	61	pW
E_field model		
L_o	450	Å
** **EPD model**		
G_{ep}	0.00006	$W/k^{(\alpha'+1)}$
α'	5	

***It was not possible to measure ρ_o and T_g directly for the crystal due to the presence of background power. The values used in the modelling were inferred from a visual best fit basis over all the experimental heat sink temperatures and power loading conditions for all of the models. For the electron-phonon decoupling model it was not possible to measure the G_{ep} of NTD Ge No17 during the experiment and no published value was available.**

****The value shown in table 3.2 was also fitted on a visual best fit basis, for the different heat sink temperatures looked at. All other dimensions and values in the models have been measured.**

Table 3.2 General parameters necessary to run the various models.

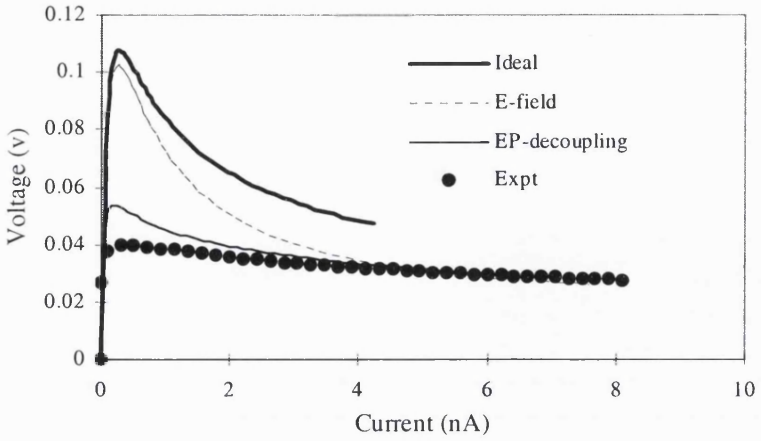

Figure 3.20 The 50mK load curves for the modelled system, the system defined by tables 3.1,3.2 and compared to the corresponding experimental VI at 50mK.

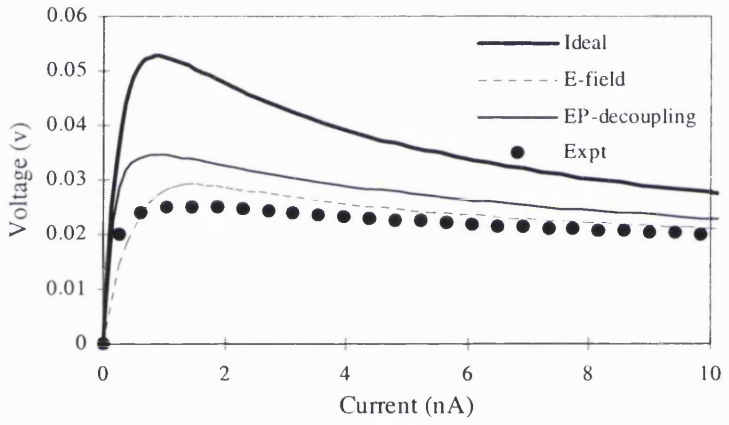

Figure 3.21 The 70mK load curves for the modelled system defined in tables 3.1,3.2 and the corresponding experimental VI at 70mK.

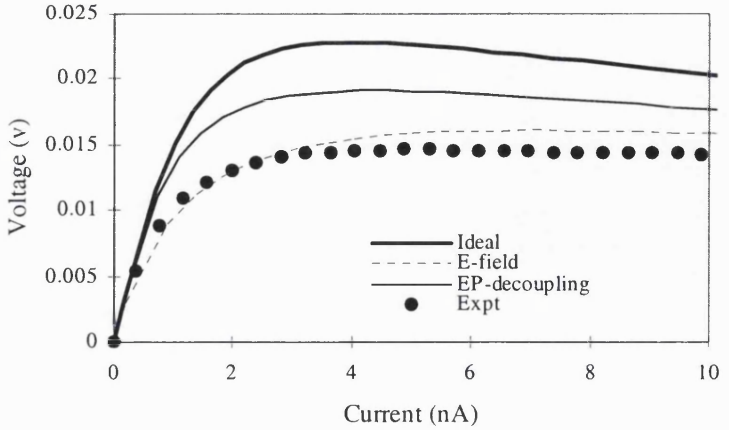

Figure 3.22 The 100mK load curves for the modelled system defined tables 3.1,3.2 compared with the corresponding experimental VIs at 100mK.

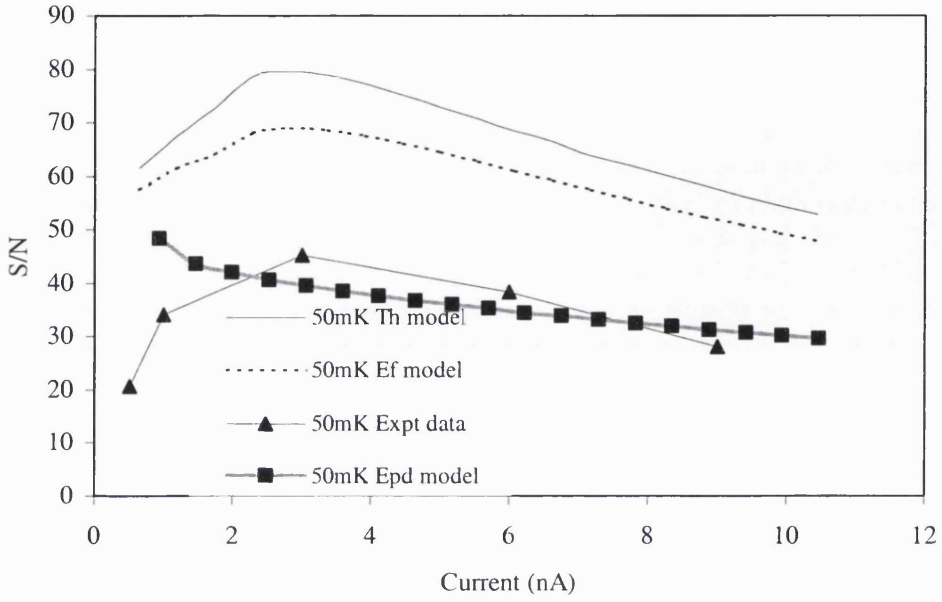

Figure 3.23 The model predictions at 50mK compared to experiment. The modelled system is given in tables 3.1,3.2

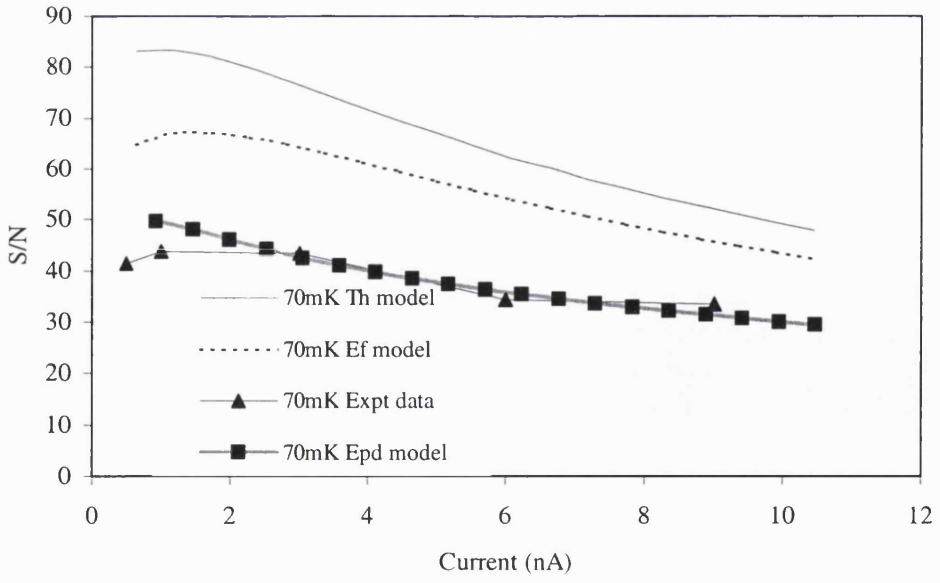

Figure 3.24 The model predictions at 70mK compared to experiment. The modelled system is given in tables 3.1,3.2

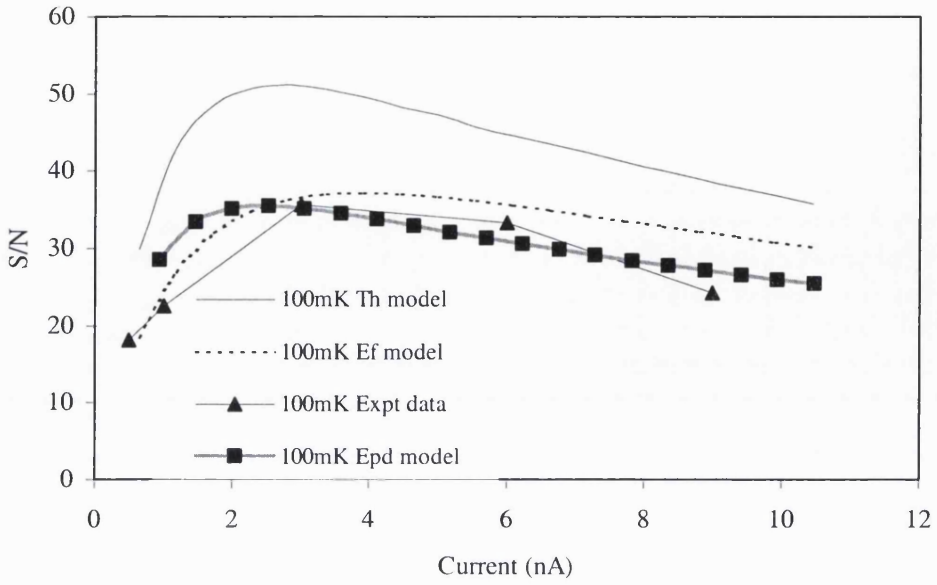

Figure 3.25 The model predictions at 100mK compared to experiment. The modelled system is given in tables 3.1,3.2

3.6.5 Conclusions

The modelling predictions for the detector load curves are compared to those obtained experimentally at heat sink temperatures of 50mK, 70mK and 100mK in figures 3.20-3.22. All the load curve models for the different cases generate curves that have a similar magnitude to the experimental observations. However, the ideal load curve model is consistently high at all temperatures. Notably, the most accurate model at 100mK is the electric field model, whilst at 50mK the electron-phonon decoupling model is more accurate. This is consistent with the findings of others [59]. In figure 3.21 we see the response at 70mK, where both the electron-phonon decoupling model and the electric field model are in close agreement, possibly indicating that both effects are operating concurrently in the detector as expected.

Looking at the signal to noise predictions from the different models, (figures 3.23-3.25), we see that the ideal model is consistently predicting a higher system resolution than that observed. It should be borne in mind that the models assume the detector is power loaded, with an additional background power. This has the implication that the detector is operating at a higher temperature, because of the additional power dissipation, for a given bias current.

This makes the effects of electron-phonon decoupling, the electric field and system attenuation not as severe as they might otherwise be.

The downside of the modelling process is that the values of ρ_o and T_g had to be inferred and are not independent. The accepted values are ρ_o=0.003 (Ω.cm) and $\sqrt{T_g}$ = 5.5 ($K^{0.5}$) as shown in figure 2.5. However using these values in the models none of the models gave consistent load curves or S/N predictions for the three temperatures looked at. However good fits to all the data are obtained with ρ_o = 0.014 (Ω.cm) and $\sqrt{T_g}$ = 5.83($K^{0.5}$). Because ρ_o and T_g could not be measured due to background power loading it is not possible to state how correct these values are, however, the magnitude of the variation between the accepted values and the inferred values are routinely observed in other NTD Ge crystals[58,60]. Another value inferred for the electron phonon decoupling model was the G_{ep} for NTD Ge No 17. This was obtained using a visual best fit of the model to all the data sets. There is no published data on this value so it is not known how good the best fit value of 0.00006 (W/K^6) is.

None of the models individually provide an exact fit to the experimental data, the electron-phonon decoupling model is best below 70mK, and the electric field model above. These are, however, an accurate representation of the physical processes involved in the practical detection of x-rays. This work is a good basis to tie in with future experiments having better statistical data.

4 High resolution NTD Ge microcalorimeter

4.1 Introduction

Future x-ray detectors are likely to require an energy resolution of ~2-8eV in the 1-12keV energy range. Theoretically, a semiconductor microcalorimeter with an NTD Ge thermistor of dimensions (0.2x0.2x0.2)mm^3, operating at temperatures of ~50mK is capable of providing this resolution, in practice, microcalorimeters have attained a resolution of ~ 8eV for 6keV x-rays [67].

Detectors run at MSSL have not achieved comparable results. In particular when experimental microcalorimeters have been run at temperatures less than 100mK, they have failed to show the predicted improvements in energy resolution. One of the goals arising from this modelling, is to identify the reasons behind the poor performance of the detectors run at MSSL. A second goal was to determine the highest resolution practically attainable using an NTD Ge based microcalorimeter. This chapter describes the way the model was used to investigate ways of improving the performance of an actual detector.

4.2 Optimisation of a microcalorimeter and its system

4.2.1 Limiting resolution of the basic system

The modelling process began by taking the current MSSL detectors as a baseline. The typical parasitic capacitances, load resistance, preamplifier noise, size of NTD Ge, size and type of absorber and finally the size and thermal link type typical of the MSSL system were used. Typically the detectors consisted of a tin absorber and two brass wires bonded to an NTD Ge crystal. The baseline crystal was assumed to have ρ_o=0.105(Ω.cm) and T_g=22.781($K^{0.5}$), the published values for NTD Ge No16 (figure 2.5). The reason for choosing this crystal to start the optimisation process was that the resistance and responsivity were most suited to operating at a relatively high temperature (100-200mK). The values of the baseline system are presented in tables 4.1 and 4.2. The estimated heat capacities for the different components at 50mK are also presented.

COMPONENT	DIMENSIONS (mm)	HEAT CAPACITY (J/K)
NTD Ge Crystal (x1)	(0.20x0.20x0.20)	$5.60X10^{-13}$
Palladium (x2)	(0.20x0.20x0.00002)	$8.80X10^{-14}$
Gold (x2)	(0.20x0.20x0.0004)	$1.12X10^{-13}$
Boron ion layer (x2)	(0.20x0.20x0.001)	$4.00X10^{-16}$
tin absorber (x1)	(0.50x0.50x0.015)	$7.09X10^{-15}$
H_{20} Epoxy (x2)	(0.06x0.06x0.06)	$8.21X10^{-13}$
brass wire (x2)	Radius=0.004,Length=0.6	$8.12X10^{-14}$

Table 4.1 Baseline detector format. The heat capacities of the components are evaluated at 50mK.

PARAMETER	VALUE	UNITS
Parasitic capacitance	16	pF
Pre-amp noise	5.7	nV/√Hz
Load resistor	240	MΩ

Table 4.2 Baseline bias system

Initially the simpler non-linear attenuation model defined in section 3.3.2.2 was assumed to be an adequate description of the system. The effects of electron-phonon decoupling and the detector electric field were addressed later in the modelling process.

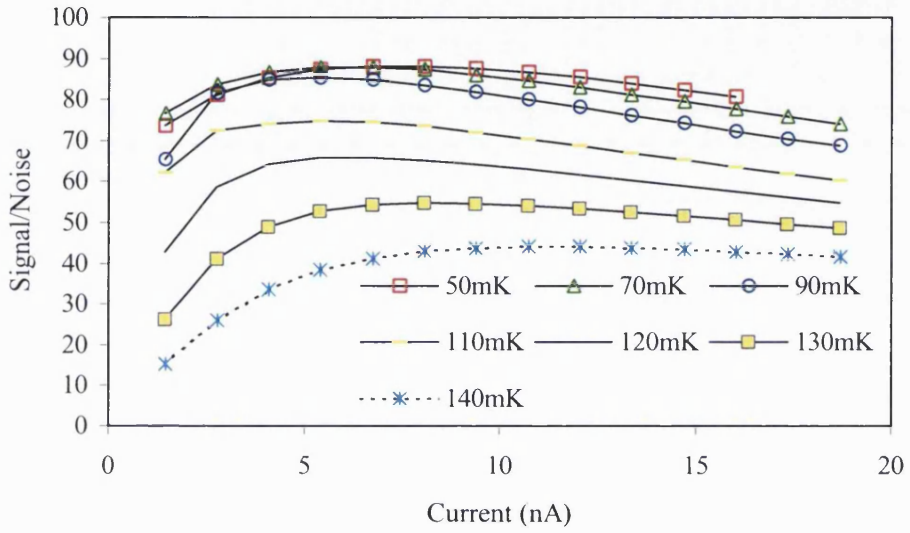

Figure 4.1 The predicted signal to noise response of the system defined in tables 4.1 and 4.2 with an NTD Ge No6 crystal to 5.89keV x-rays.

The initial predictions of the attenuation model for the baseline system to 5.89keV x-rays, at a range of heat sink temperatures, are shown in figure 4.1. The figure shows that at each heat sink temperature the response has a peak at some bias current corresponding to a working temperature $T_{max\text{-}response}$. When the expected thermodynamic response for this temperature is calculated from equation 2.6 and compared to the modelled response it was evident why previous detectors run at MSSL had failed to achieve resolutions close to the ideal thermodynamic response.

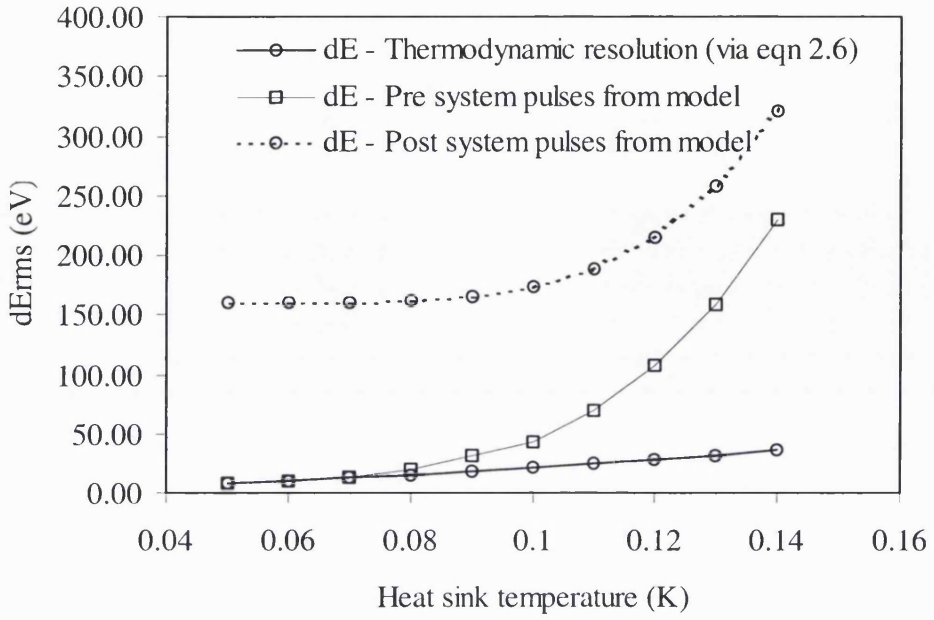

Figure 4.2 Comparison of the maximum FWHM resolution of the modelled system used to create figure 4.1 along with the corresponding ideal thermodynamic prediction.

In Figure 4.2 a plot of the comparison is shown. The ideal FWHM thermodynamic resolution for $T_{max\text{-}response}$ is compared to the corresponding model predictions as a function of heat sink temperature. The FWHM thermodynamic resolution from the model is estimated from both the attenuated and unattenuated case. From the plot, three features are evident.

- The operational temperature of the maximum response $T_{max\text{-}response}$ is significantly greater than the heat sink temperature. For example the model predicts for a heat sink temperature of 40mK the maximum response is observed at a detector temperature of 94mK.
- The thermodynamic response of the system approaches the ideal thermodynamic resolution only at low heat sink temperatures.
- The overall system response defined by the attenuated pulses is offset above the thermodynamic response.

As the noise estimates are the same in the pre- and post-attenuation cases, the entire offset is attributable to attenuation of the pulses. The system response flattens earlier than the thermodynamic response due to the increased detector resistance. The modelling indicates that there is a trade off between the increased thermodynamic resolution and the decreased system bandwidth, imposed by the increasing detector resistance, when working at lower

temperatures. These two effects conspire to define an optimal operating temperature range over which the response for any single NTD Ge in a specific system effectively reaches a maximum. This temperature range will vary for different NTD Ge since they all have different resistances.

This is the reason why previous detectors run at MSSL have failed to achieve resolutions close to the ideal thermodynamic response. The detectors had been operated at temperatures beneath their optimum range and this provides little or no increase in resolution.

4.2.2 Improving the bias and pre-amp circuit

Having defined the basic detector system, and used the attenuation model to define the magnitude and trend of the system response over a wide temperature range, ways of improving the resolution were modelled. There are two ways to improve the resolution: modifications to the microcalorimeter itself or the bias readout circuit. The initial modelling concentrated on improvements to the bias and pre-amp circuit.

A key lesson from section 4.2.1 was just how detrimental attenuation is to the response of the system, imposing a factor of ~15 degradation on the ideal thermodynamic resolution of the detector. This attenuation is inversely dependent on the resistance of the detector. It also has an inverse dependence on any parasitic capacitance within the system. The dependence is linear; by halving the capacitance, the bandwidth of the system is doubled. For the baseline system a parasitic capacitance ~16pF was assumed. This is the normal level of parasitic capacitance observed in the typical detector set-up at MSSL. However, in the past it proved possible to reduce this to ~7pF [68]. This was achieved by placing the readout wires and load resistor on quartz blocks to minimise the parasitic capacitance induced by having the wires in close contact with the heat sink surface, which acts as a common system ground.

Another baseline system parameter that could be improved was the level of voltage noise assumed for the JFET pre-amp. The JFET noise value used in table 4.2 assumes the use of a warm IFN140 source follower JFET. When operating at a temperature of 140K it was found that these had an input short noise of ~ 5.7nV/Hz. Prior to the modelling work these were the lowest noise JFETs used at MSSL. Experimental work was carried out to investigate the noise performance of some modern IFN140 source follower JFETs.

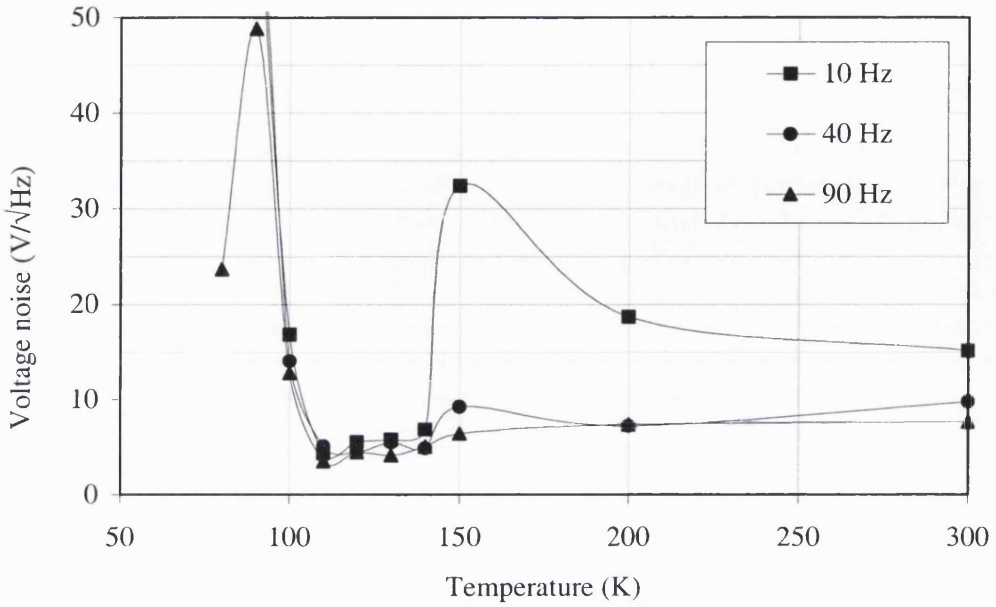

Figure 4.3 The noise performance of an optimally selected IFN140 JFET. Operating at 110K the noise is~3nV/(√Hz) and is found to be spectrally flat.

It was found that new models, operated at 110K, have a superior noise performance to their older counterparts. Of the 20 JFETs tested the best had an inherent noise of ~3nV/√Hz. The experimentally obtained response of the best selected JFET is shown in figure 4.3. This figure can now be used in the models. The baseline system can be updated to that shown in table 4.3

PARAMETER	VALUE	UNITS
Parasitic capacitance	7	PF
Pre-amp noise	3	NV/√Hz
Load resistor	240	MΩ

Table 4.3 Improved bias system

An additional parameter not related to the NTD Ge crystal is the amount of H_{20} epoxy assumed for the baseline system in table 4.1 for the initial models was an overestimate. This is important since the major component to the detector heat capacity is the H_{20} epoxy. The initial values were chosen from experience, however at the time of the modelling work, a new micro-manipulator facility at MSSL made it possible to bond the detector components using much smaller amounts of epoxy. It was considered that a $(0.02x0.02x0.02)mm^3$ volume of

epoxy would be sufficient to bond a single thermal link to the detector. Using published values [51] the heat capacity of two such volumes of H_{20} at 50mK is estimated to be 3.042×10^{-14} J/K.

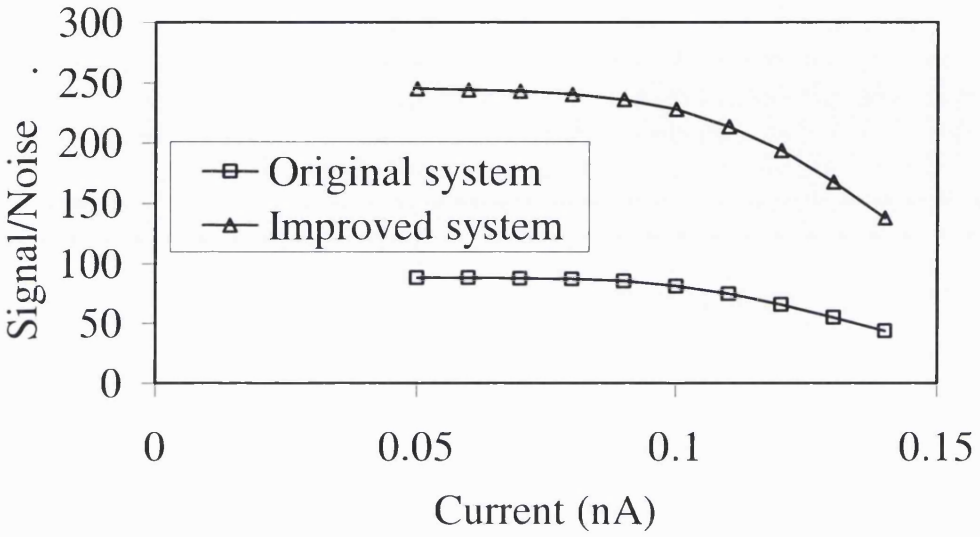

Figure 4.4 The original system response compared to the improved system response. The response is simulated for 5.89keV x-rays. The system is defined in tables 4.3 and 4.1, but with the epoxy volume reduced to $2x(0.02x0.02x0.02)mm^3$.

Taking the changes shown in table 4.3, along with the reduced epoxy volumes, the attenuation model was re-run. The improvement to the system response is shown in figure 4.4; the response has increased by a factor of ~2.5. This is because the thermodynamic resolution has increased slightly due to the reduced heat capacity of the epoxy. However, the system is now operating closer to its ideal thermodynamic resolution because of the reduced attenuation and pre-amplifier noise. As shown in figure 4.5 the degradation incurred by the system now only factor ~6 above the thermodynamic resolution.

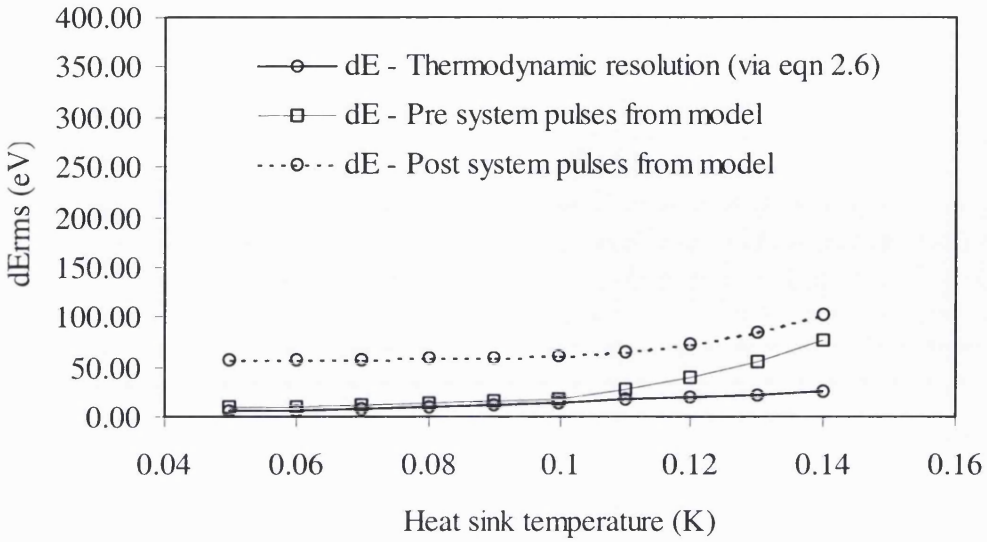

Figure 4.5 Comparison of the FWHM resolutions predicted by the model for the improved system in figure 4.4 with the ideal thermodynamic equivalent.

4.2.3 Possible Improvements to the NTD Ge crystal detector

Having identified practical ways to improve the bias system, modelling was carried out to assess what practical changes in the detector would improve the performance of the overall system. Three essential areas to investigate were identified

- Choice of doping level and operating temperature
- Minimisation of detector heat capacity
- Optimising the thermal links for the best system response

4.24 Choice of NTD Ge thermistor

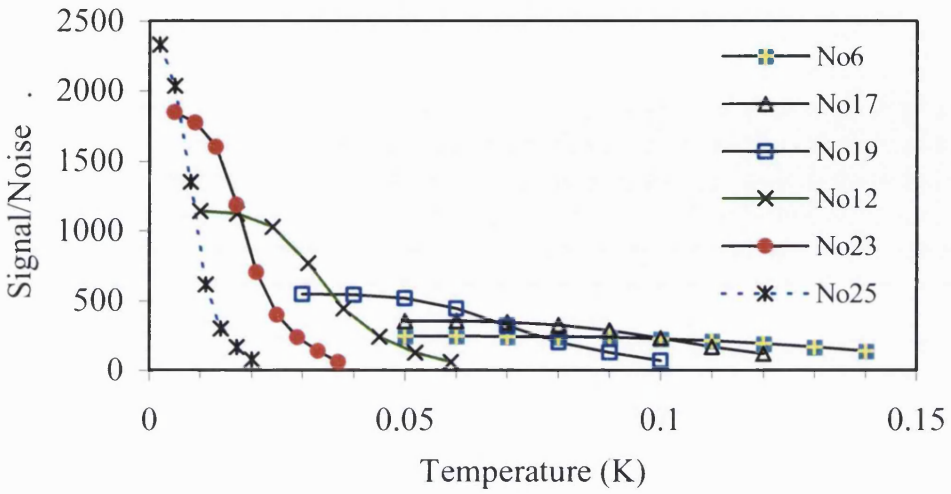

Figure 4.6The predicted system response to 5.89keV x-rays using different NTD Ge crystals. Other system values are taken from the improved system used to generate figure 4.4.

In this section the effect of using NTD Ge crystals with different doping levels on the system resolution are investigated for the general bias system as defined in table 4.3, and the detector geometry from table 4.1. The system also incorporates the reduced epoxy volume suggested in the last section.

The system attenuation model was run using different values of ρ_o and T_g corresponding to NTD Ge crystals with different doping levels. The values of ρ_o and T_g chosen for the modelling were taken from published values for different NTD Ge crystals [52]. The published resistivities are given in figure 2.5 and table 2.1.

The modelled signal to noise as a function of heat sink temperature is shown in figure 4.6 for different NTD Ge detectors. Each NTD exhibits an optimal heat sink temperature; running the system below this temperature produces a minimal increase in system resolution. A comparison of this plot with table 2.1, shows the relationship between doping level and operating temperature. Those NTD Ge detectors with low a T_g value (higher doping level) have lower optimal operating temperatures. For each NTD Ge a definite transition temperature exists below which the resolution of the system cannot be greatly improved. In this temperature region the attenuation by the decreased system bandwidth (induced by the increasing detector resistance) offsets any subsequent thermodynamic increase.

As the value of T_g drops, the magnitude of the system response becomes markedly increased. Of the NTD Ge detectors modelled in the temperature regime 5mK to 100mk, NTD Ge No.23 has the best performance. The reason for considering this temperature range in the modelling is that it should be accessible by future space borne cryogenic systems. It should be possible to reach a temperature in the region of 10mK using a small ADR tailored for use on space craft [69,70]. Below 5mK NTD Ge No 25 has a higher response than No 23. However achieving temperatures lower than 5mK on a space craft with reasonable hold times is technically very difficult and would give a relatively small improvement in resolution. From figure 4.6, the response from an NTD Ge No23 thermistor flattens at 5-10mK where it is predicted to have a resolution of 7.4eV FWHM to 5.89keV x-rays. To go to an operating temperature below 5mk, NTD Ge No 25 is necessary; its responsivity increases to below 1mK where it is predicted to give 5.9eV FWHM for 5.89keV x-rays.

4.2.4 Minimising the detector heat capacity

The previous section identifies the best type of NTD Ge to achieve the maximum system response in a given temperature range. The next topic addressed in the modelling was to look at the feasibility of reducing the heat capacity of the detector element. By minimising the heat capacity of the detector, the thermal responsivity is increased (equation 2.6). The system attenuation model was used to examine the merits of reducing the size of different detector components when detecting a wide range of x-rays. An examination of the heat capacity presented in table 4.1 reveals that the dominant contribution to the heat capacity of the detector modelled thus far is due to the NTD Ge crystal itself. (Providing we assume the reduced amount of H_{20} epoxy is used to bond the links as suggested earlier.)

To model the effect of reducing the size of the crystal, the width t, between the detector terminals was successively reduced leaving the contact area A, the same. By reducing the crystal in this dimension the resistance is reduced. This minimises the effect of attenuation by the system bandwidth, since the resistance is reduced leaving dR/dT the same. The downside of thinning the crystal is that the electric field across the detector is increased, making the detector more susceptible to electric field effects. However, as shown later in section 4.3.1 the E-field is not predicted to be a large problem for these crystals at temperatures in the 10mK region. Thinning the crystal should therefore be beneficial.

Taking the values presented in table 4.2 and assuming the reduced epoxy case, the

attenuation model was rerun for different crystal thicknesses and at several x-ray energies. The result is shown in figure 4.7. It is found that there is an optimal crystal thickness of 40µm for 6 to 12 keV x-rays. Figure 4.8 shows the corresponding FWHM resolution of the system in eV. From the plot 20µm and 40µm thick crystals have almost equivalent resolution for 6KeV x-rays, For 12KeV x-rays the 40uM thick crystal has a higher resolution, because it suffers less from a non-linear heat capacity. For the 40µm case, the simulation predicts a system resolution in the range 3.7-9.2eV over 0.5-12keV x-rays range.

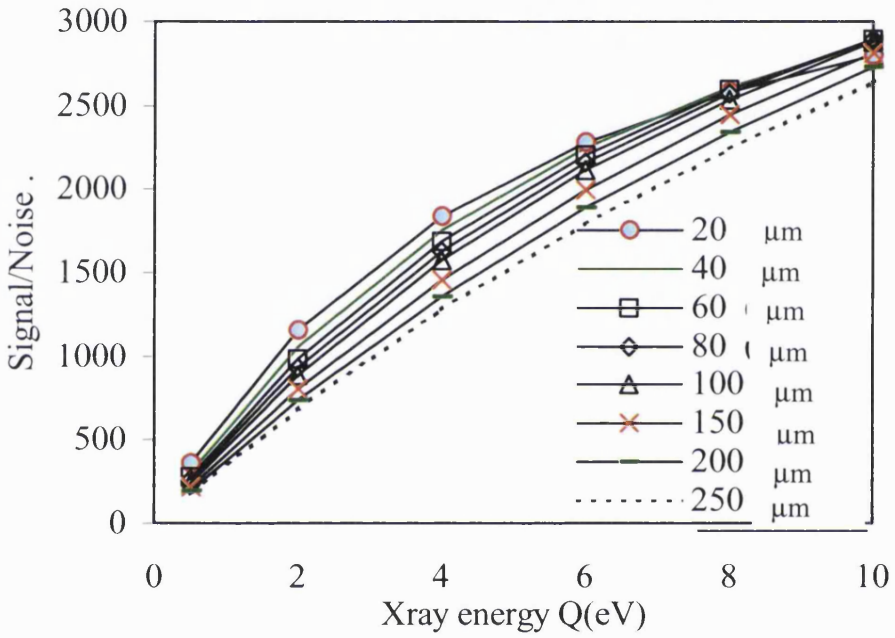

Figure 4.7. The non-linear system response as a function of crystal thickness and x-ray energy. The system is as for figure 4.6.

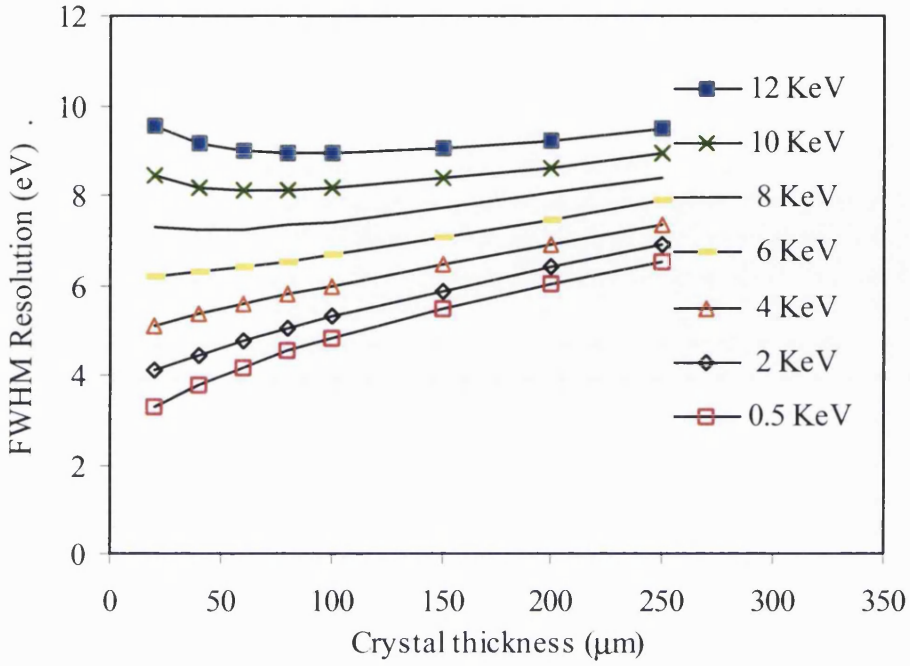

Figure 4.8 The corresponding FWHM energy for different x-ray energies corresponding to figure 4.7.

4.2.5 Improvements to the thermal links

So far, the system optimisation process has indicated that the system, as presented in table 4.4, can attain a FWHM resolution of 6.2eV for 6keV x-rays. It has also shown that there is no benefit to reducing the size of the crystal much below 40μm. We can now optimise the thermal links. The thermal link assumed in the modelling is based on previous experimental detectors and has not been optimised to suit the preamplifier circuit. An optimal thermal link will match the detector time constant to the preamplifier circuit and allow the detector to bias at more favourable operating temperatures.

COMPONENT	DIMENSIONS (mm)	HEAT CAPACITY (J/K)
NTD Ge Crystal (x1)	(0.20x0.20x0.04)	$2.25X10^{-14}$
Palladium (x2)	(0.20x0.20x0.00002)	$1.76X10^{-14}$
Gold (x2)	(0.20x0.20x0.0004)	$2.24X10^{-14}$
Boron ion layer (x2)	(0.20x0.20x0.001)	$8.00X10^{-17}$
tin absorber (x1)	(0.50x0.50x0.015)	$5.67X10^{-17}$
H_{20} Epoxy (x2)	(0.02x0.02x0.02)	$6.08X10^{-15}$
brass wire (x2)	Radius=0.004, Length=0.6	$1.62X10^{-14}$

Table 4.4 Improved detector format. The heat capacities of the components are evaluated at 10mK.

The ideal response of the microcalorimeter given by equation 2.6 is a function of heat capacity and temperature, independent of the conductivity G(T), of the thermal link. Whilst this is true for the detector it is not true of the entire system. Changing G(T) changes the temporal profile of an x-ray pulse and consequently its spectral profile. For a fixed system bandwidth, a smaller G(T), will generate a slower pulse, which will contain fewer high frequency components, reducing the attenuation by the pre-amp system. This is a simplified picture. The exact response of the system is more complicated since the detector at some working temperature will have a complex impedance $Z(\omega)$ as shown in equation 2.26 ($Z(\omega)$ is a function of the conductance G(T)). Changing the thermal link will change the equilibrium temperature at which the detector biases, effectively shifting the detector load curve and modifying the overall system response for a given bias current.

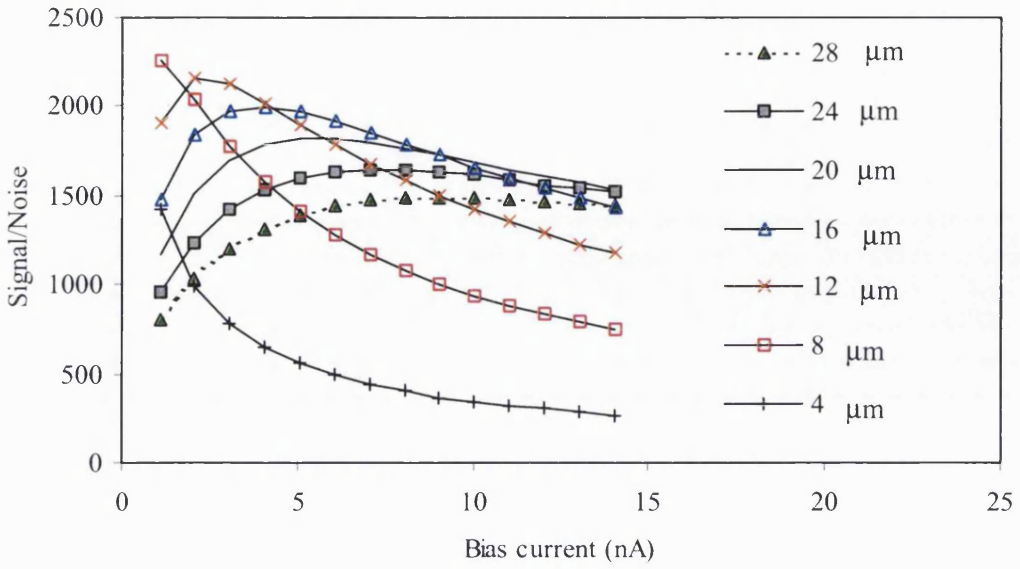

Figure 4.9 The response of an No23 crystal at a heat sink temperature of 10mK to 5.89keV x-rays. The system is specified in tables 4.3 and 4.4. The response is given for different brass link diameters as shown. All cases have a link length of 0.6 mm

The brass wires defined in table 4.4 were taken as a starting point for the optimisation of the thermal link. The effect of changing first the length and then the cross-sectional area of the wire was investigated. The results of the simulation are shown in figures 4.9 and 4.10. The model indicates that the optimal brass link for the system is 8µm in diameter and 0.3mm long giving a FWHM resolution of 6eV to 6keV x-rays.

What do these results imply generally, about the optimisation of the thermal links for a typical system? For a thermal link, increasing the cross sectional area A of the link increases the heat capacity of the detector, since $C \propto AL$. It also increases the conductance as $G \propto A/L$. Thus, the speed of the detector response given by its time constant C/G remains unchanged implying the speed of the detector is insensitive to the cross sectional area of the link. This change has done nothing to improve the throughput of the system. It seems undesirable, since the inherent thermodynamic response of the detector is decreased, by the increasing bulk heat capacity C. Contrary to expectations the model indicates that this is not the case. The increased G allows the detector to bias at a lower operating temperature closer to the heat sink temperature. This gives the detector a higher α and on balance, actually improves the system response. Conversely decreasing the cross sectional area lowers the response of the system.

The benefits of continually increasing the cross sectional area of the link are limited, since the working temperature of the detector may only approach T_O. Before this happens a point is reached where the increasing heat capacity of the link begins to dominate and the response of the detector turns over, we see this in figure 4.10 for link diameters greater than ~ 8μm.

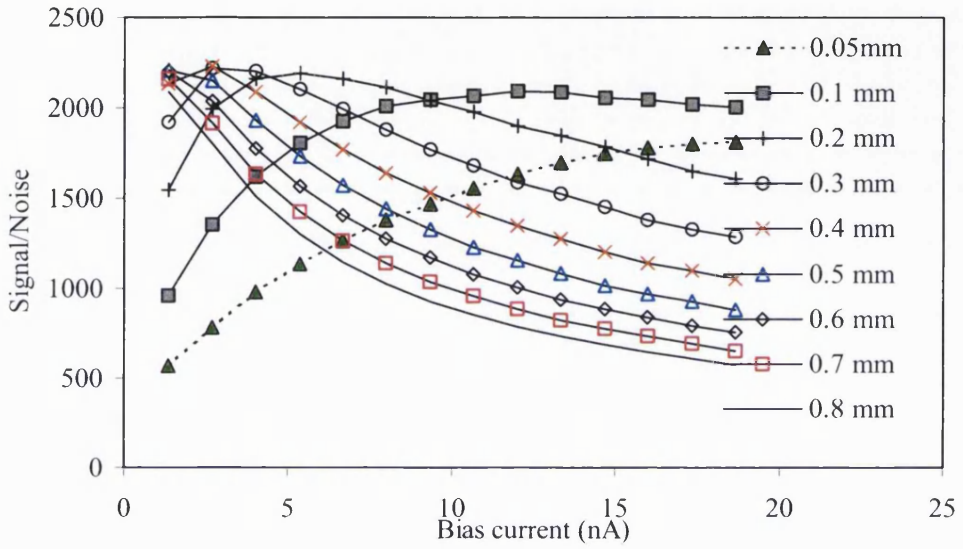

Figure 4.10 The simulated response of the system to varying link geometry's. The modelled system is as in figure 4.9. All the curves have a cross-sectional diameter of 8μm. Each case represents a different link length as shown.

If the length L is increased, C increases, thereby reducing the magnitude of the detector thermodynamic response. Additionally G is decreased causing the detector to bias at a higher working temperature. Both these effects degrade the thermodynamic response of the detector. Shortening the link causes the opposite to occur. For shorter links the responsivity of the detector is increased and the detector biases at a lower working temperature because of the increased G. Again, the greater conductivity improves the system response. Because of the increased G, the pulses are now faster and thus more susceptible to attenuation by the system bandwidth. This eventually limits the improving response and is seen for the modelled case in figure 4.10, where the response turns over for lengths less than 0.3mm long.

To summarise, the model indicates that the most important characteristic of a low temperature link is that it has a high conductivity. This allows the detector to benefit from a low heat sink temperature, which increases its responsivity. It is important that the conductivity is not too high as this will decrease the time constant and generate faster pulses, which will suffer greater attenuation in the bias and pre-amp circuit. The modelling indicates that the system can attain a resolution of 6eV FWHM to 5.89keV x-rays with the links optimised. The optimised links are two 8μm diameter, 0.3mm long brass wires.

4.3 Other Non ideal factors

The attenuation model used in sections 4.1 and 4.2 to model system improvements predicts that a FWHM resolution of 6eV at 6KeVis potentially attainable, using a typical detector in the MSSL detector system. The attenuation model does not account for electron-phonon decoupling, the electric field and thermal boundary resistances inside the detector. This section will address these points. Published data is used to estimate the effects of these on the system resolution.

4.3.1 Electric field effect

The modelling in section 4.2 indicates that NTD Ge No23 gives the best system resolution. We can take this model and calculate the effect of the electric field on this resolution. No data are available on the intrinsic hopping length in NTD Ge No23 at 5mK. However, for NTD Ge detectors having impurity concentrations lying in the range from $3.8x10^{16}$ cm^{-3} to $5.6x10^{16}$ cm^{-3}, the hopping length L_o is accepted to be ~450Å [42]. This range includes NTD Ge No's 6, 17 and 19. NTD Ge No12, No23 and No25 are more heavily doped. Since the intrinsic hopping length drops as the impurity concentration increases (see section 2.4.3.1), these NTD Ge suffer less from E-field effects. The E-field model (section 3.4) was run using a hopping length L_o=450Å indicative of NTD Ge with lower doping levels giving an upper bound to the degradation.

The basic system was assumed to be the optimal system presented in tables 4.3 and 4.4 with 8μm diameter, 0.3mm long brass wires. NTD Ge No 23 was used in the simulation since this provides the highest resolution. The results of the simulation are shown in figure 4.11. From this, it can be seen that the E-field has a relatively small effect on the resolution of the system. For this example, the R_o and T_g were those for NTD Ge No 23, but the hopping length used was 450Å. This gives a pessimistic estimate of the degradation. The model predicts that the resolution is reduced by ~15%, thus the likely degradation on an NTD Ge No 23 crystal will be less than 15%.

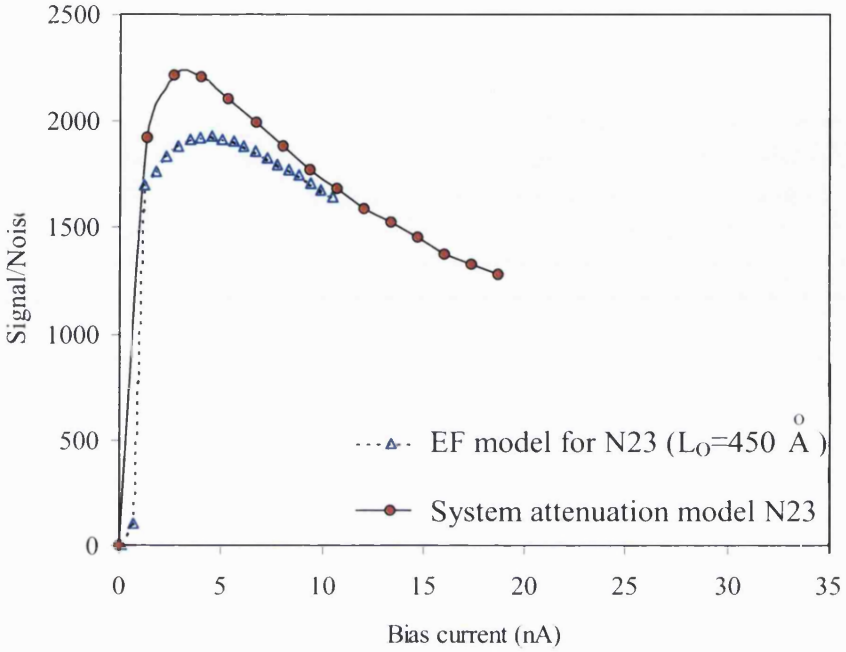

Figure 4.11 The effect of the electric field on the system resolution .The system is given in tables 4.3 and 4.4 except the wires 8μm diameter and 0.3mm long. The prediction of the attenuation model is shown with the corresponding E-field model prediction. The response was calculated for a 5.89 keV x-rays. L_o is given in Angstroms.

4.3.2 Electron-phonon decoupling

It is expected that electron-phonon decoupling will also reduce the responsivity of the ideal system of 6ev for 6keV x-rays as given in section 4.2.5. The level of decoupling for NTD No 23 has been experimentally found to be $0.09W/K^6$ with $\alpha'=5$ at 20mK [40]. The electron-phonon decoupling model described in section 3.5 was run using the system values for the ideal case, predicting that the responsivity of the system will be markedly reduced as shown in figure 4.12. The resolution of the system is now a factor of ~ 5 lower than predicted by the system attenuation model of section 4.2 giving a RMS response of ~17ev to 5.899keV x-rays which is equivalent to a FWHM resolution of 40eV.

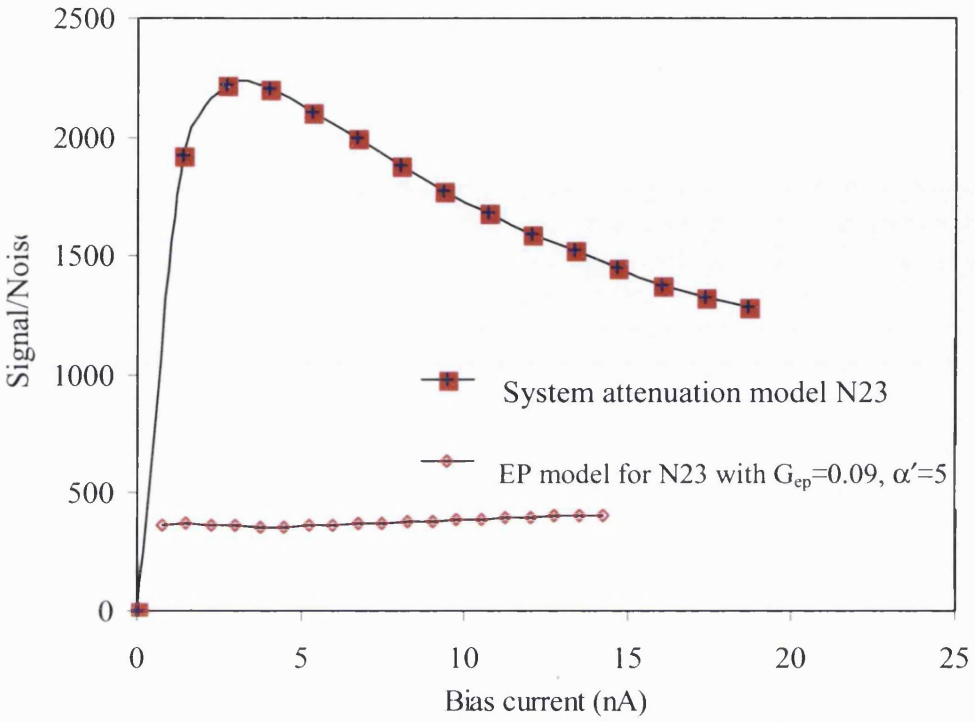

Figure 4.12 Electron-phonon decoupling model predictions for the system in tables 4.3 and 4.4 (filled symbols). The wires were set to be 8μm diameter and 0.3mm long. The NTD Ge modelled was No23 operating at 5mK.Corresponding attenuation model predictions are also shown. The assumed decoupling values of α′ and G_{ep} ($W/K^{\alpha'+1}$) are as shown on the plot. The response was calculated for 5.89keV x-rays.

The initial decoupling modelling assumes that the high conductivity links, indicated by the system attenuation model, are still applicable with high levels of decoupling. This is not entirely true, with high levels of decoupling, the high conductivity of the links limit the resultant pulse height registered in the electron population. This is because the phonons will leak away to the sink far too quickly to be registered in the electron population. To investigate this effect the electron-phonon decoupling model was rerun for the same levels of decoupling with an NTD Ge No23 crystal, but having different wire lengths. The results are shown in figures 4.13, which show the response at 5mK. There is an obvious correlation between the length of the link and the level of decoupling. Higher levels of decoupling require longer optimal link lengths. The optimal length of the link for NTD Ge No23 at 5mK was found to have increased to 1-2mm giving an RMS system resolution of 7.4eV for 5.89keV x-rays and a FWHM response of ~ 17eV. The modelling indicates that it is possible to limit the effect of decoupling in crystals by reoptimising the length of the thermal links for the presence of decoupling. However, it cannot be eliminated and thus it still has a significant effect on the resolution of the system.

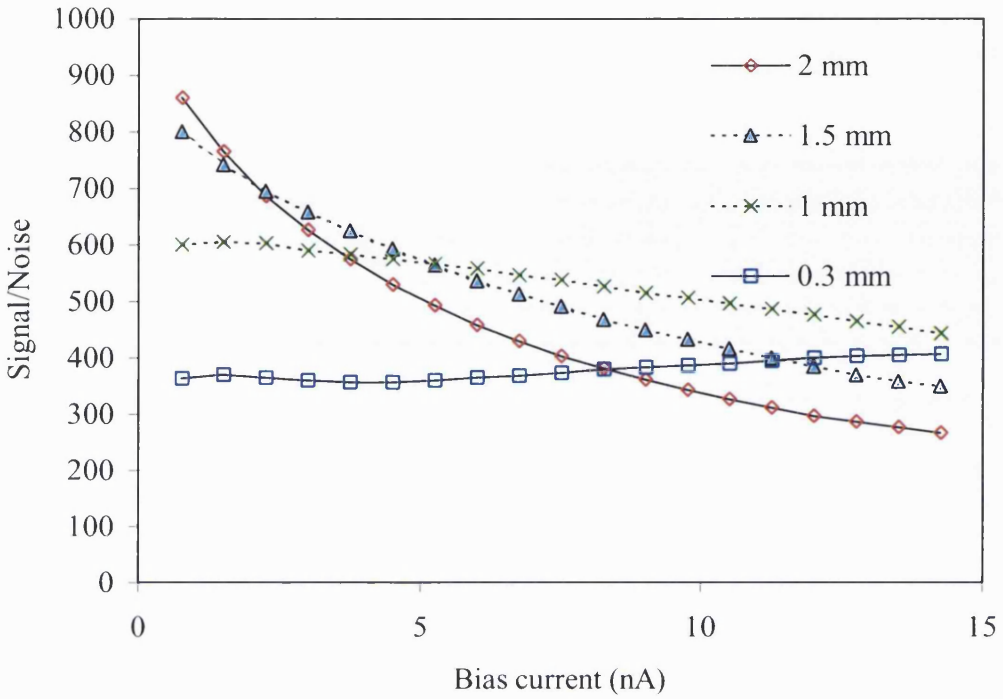

Figure 4.13 The modelled decoupled response of an NTD Ge 23 crystal to 5.89 keV x-rays. Model parameters are given in tables 4.3 and 4.4. Different lengths of 8μm-∅ brass wire were simulated. Decoupling parameters used were $G_{ep}=0.09(W/K^{\alpha'+1})$ and $\alpha'=5$.

4.3.3 Thermal boundary resistance

Thermal boundary resistances exist at all material boundaries within the detector [71]. The thermal models used to generate the pulses in the system attenuation model and E-field model, along with the electron-phonon decoupling model, are simplifications of the actual detector thermal circuit (as mentioned in section 3.2). These models ignore the boundaries. Whilst this is a reasonable assumption at temperatures above 100mk it may not be the case at lower temperatures since boundary resistances typically have a $1/T^3$ dependence.

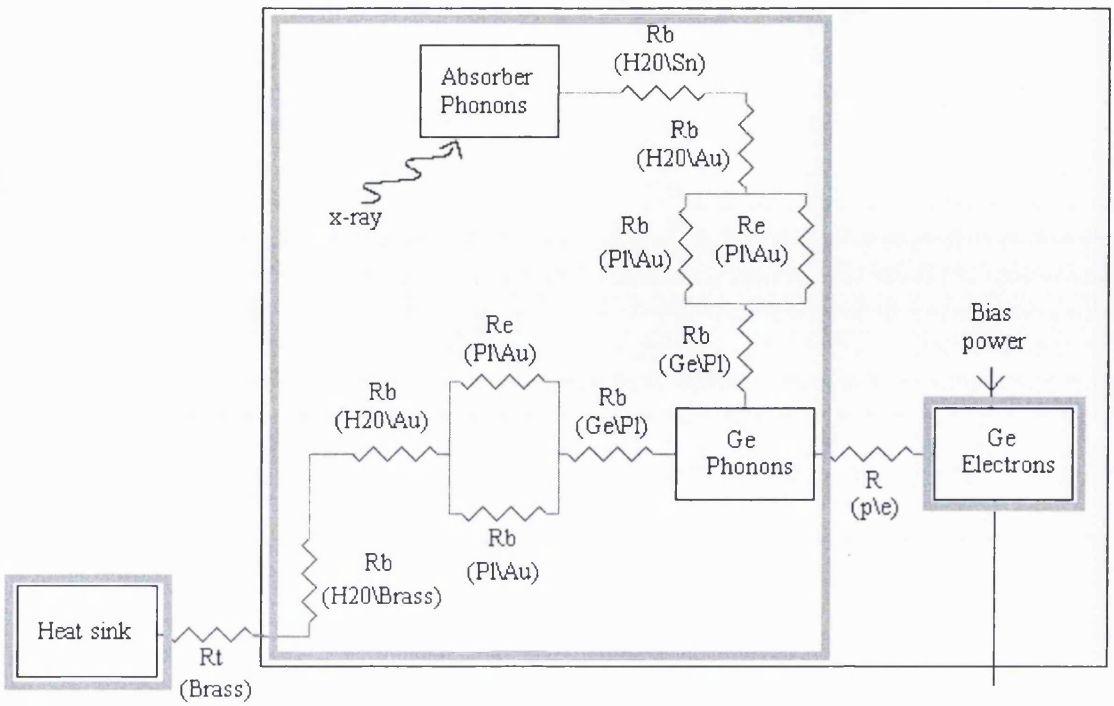

Figure 4.14 A complete detector thermal circuit for the detector shown in figure 3.1. It includes all the major thermal boundary resistances.

A more complete thermal model of the MSSL detectors would have a form shown in figure 4.14. In the diagram, all the likely thermal resistances within the detector are outlined. The black line indicates the elements within the simplified thermal model and the grey line surrounds the elements considered by the electron-phonon decoupling model. When the thermal resistivity of the links, R_t, exceeds all other thermal resistances the model reverts to the attenuation thermal model. When the resistivity imposed by electron-phonon decoupling R(p\e) becomes comparable to R_t the EPD model becomes relevant. Whether the assumptions in these models are valid at 10mK needs to be assessed in light of the additional boundary resistances.

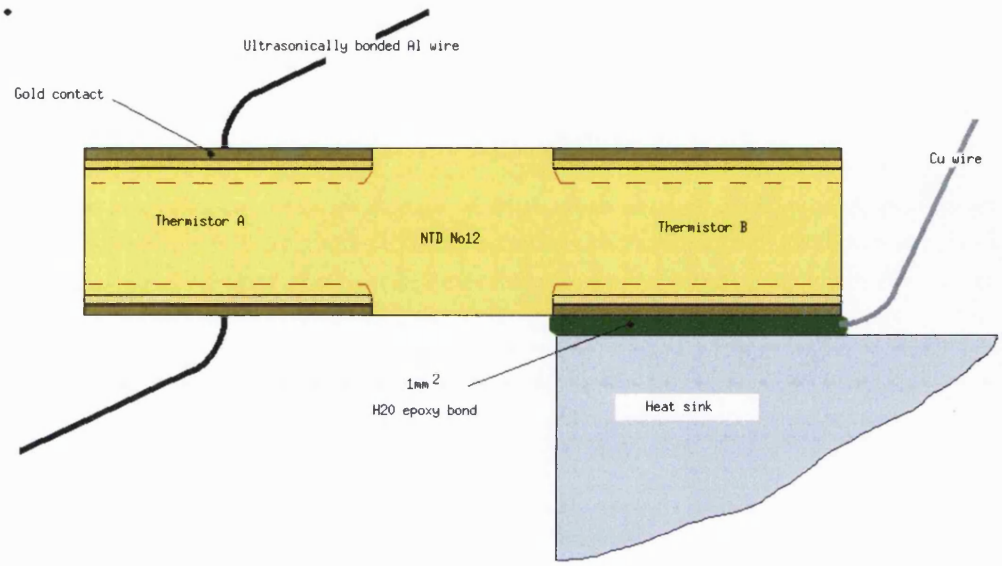

Figure 4.15 A schematic of the experiment by Wang to measure the boundary resistance of H_{20} epoxy. (Adapted from [60])

Ideally, all the boundary resistances within the system need to be quantified. This is not possible since there is very little published data available on these types of interfaces in the sub 100mK region. However, an experiment has been carried out at UCLA to measure the thermal conductivity of a H_{20} epoxy bond; using two NTD Ge No12 crystals with metallised contacts [60]. The two NTD Ge crystals, used as thermistors, have a very similar form to the modelled MSSL microcalorimeters. The experimental set-up used for the UCLA experiment is shown in figure 4.15.

In the experiment, one thermistor acted as a sensor and the other as a heater. The Kapitza conductivity for a 1mm bond area of H_{20} epoxy was estimated to be 6.8×10^{-5} $(W/K^{(\beta+1)})$[60], where β was found to be 3.2 (+/- 0.1). This value was obtained at both 18mK and 27mK indicating they had the same linear temperature dependence in this range. It was noted that by switching the roles of temperature sensor and heater the same result was obtained. This indicates that there was no discernible temperature gradient across the chip; this would only have been the case if all the internal boundary resistances were less than the boundary resistance at the H_{20} epoxy bond.

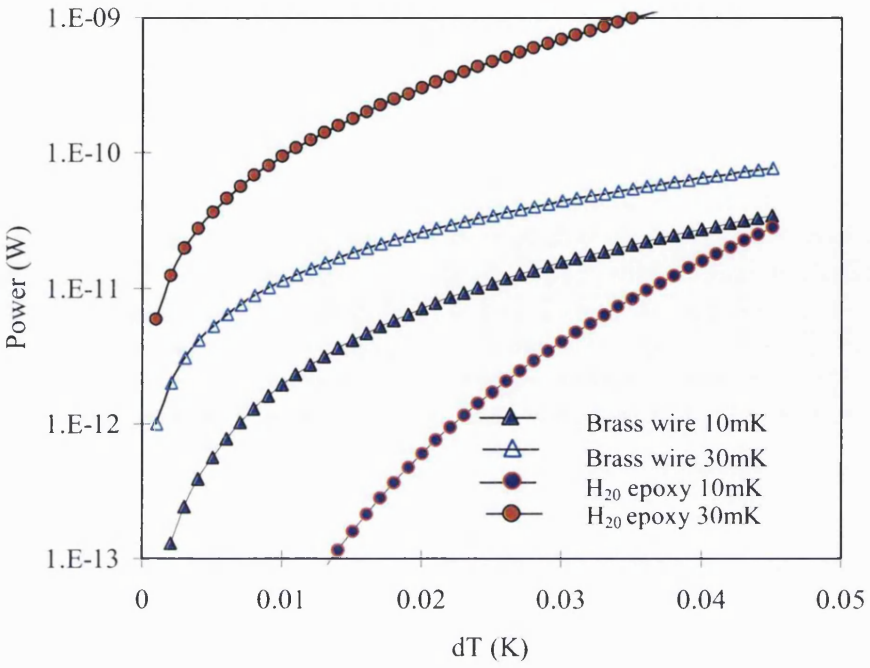

Figure 4.16 A comparison of the thermal power transmitted by a 1mm^2 H_{20} boundary compared to a 1mm long 8μm diameter brass wire as a function of the temperature difference dT across the link. The curves are plotted for heat sink temperatures of 10mk and 30mK.

From the above experiment it may be assumed that the same is likely to be true of the modelled detectors, since they also use a H_{20} bond to fix the thermal links. However, the brass\H_{20} epoxy boundary of the modelled detectors, not the thermal resistance of the brass wires, may provide the dominating thermal resistance. Using the results from the above experiment, the thermal power across a 1mm^2 H_{20} epoxy\metal boundary, can be estimated and compared to that through a 1mm long, 8μm diameter brass wire to see which will dominate at 10mK. Such a comparison is shown in figure 4.16. The figure shows that the thermal power through such an H_{20} epoxy bond (with a 1mm^2 contact area) exceeds the power through the modelled link at 30mK (i.e. the thermal resistance of the wire dominates). However, at 10mK, the power through the link exceeds that through the H_{20} epoxy for small thermal gradients across the links. This implies that the thermal conductivity of the H_{20} bonds used in the model may not be an adequate representation of the physical system at low bias currents in the 10mK region.

In spite of this the overall model is a reasonable representation of the system. For low bias currents, at 10mK the model would be more applicable to a system that used a higher thermal conductivity epoxy.

4.4 Pre-amplifier noise in the 10mK region

Using equation 2.6 for the detector given in table 4.4 at 10mK, a FWHM resolution of 0.47eV is estimated. The attenuation model predicts a resolution of 6eV for 6keV x-rays at 5mK. The degradation here arises from attenuation, a non-linear response and self heating of the detector. The addition of decoupling and the electric field as shown will degrade the resolution further. However, at 10mK these are not the only potential problems in the system. In the region of 10mK, for a low R_o and T_g thermistor (heavily doped e.g. NTD Ge No 23) a significant part of the degradation in resolution comes from the pre-amp voltage noise. In fact at these temperatures, this is found to dominate the system noise.

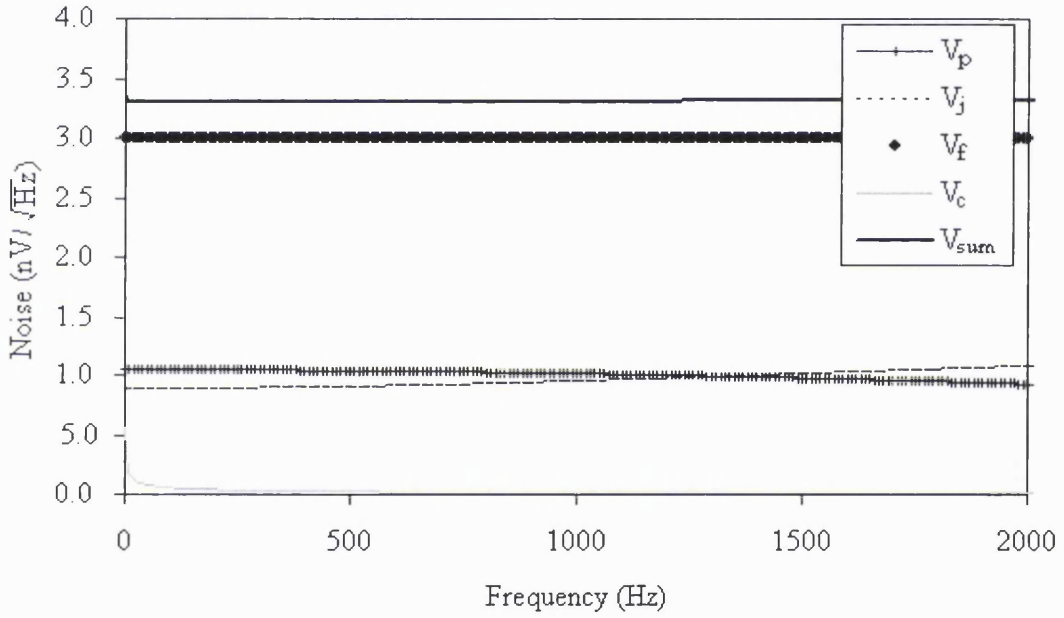

Figure 4.17 A plot showing the contributions to the system noise at 10mK. This has been calculated for the 1.5nA point on the 0.5 mm long link curve shown in figure 4.10.

Figure 4.17 shows the predicted contributions of different noise components to the system noise for a No23 detector at 10mK. Because the system is dominated at this point by pre-amp voltage noise, any improvement in this parameter will result in large improvements in the system response. This highlights a need to develop a better preamplifier; for example a preamplifier with an input short noise of 1(nV/√Hz) would increase the system resolution by ~150%. The JFET pre amps currently used at MSSL have a voltage noise of 3nV/√Hz these JFETS are selected on the basis of heritage; it is not known if there are others available which have improved noise levels.

4.5 Limiting resolution

The work presented here set out to address whether an NTD Ge detector can fulfil the energy resolution required by future x-ray spectroscopic detectors. The ideal attenuation and E-field models indicate that NTD Ge microcalorimeters operating in the region of 10mK can certainly get close. The EPD model predictions are slightly more pessimistic but indicate that it may be possible to mitigate the effects of decoupling by tailoring the thermal link. The most damaging effects are system limiting effects i.e. attenuation of the pulse and noise from the pre-amplifier. Due to the lack of experimental data, it is not possible to be definitive about what resolution will ultimately be attainable. The estimates given here are estimates based on limited physical data, for instance the EPD simulations are subject to considerable variations due to uncertainties in the values of electron-phonon conductivity G_{ep} ($W/K^{\alpha'+1}$) and the power law exponent α'. Published values of G_{ep} and α' for the same NTD Ge No 12 crystal are considerably different [60]. It is very likely therefore, that the published values of $G_{ep}=0.09(W/K^{\alpha'+1})$ and $\alpha'=5$ measured for a single NTD Ge No23 crystal (which was used in the modelling) will be subject to a similar variability. This would have a big effect on the predicted system resolution and it seems possible that No23 crystals could be selected with more favourable values of G_{ep} and α'.

The effect of this variability on the resolution can be illustrated by taking the system used to generate figure 4.14 and rerunning the model for an NTD Ge crystal, having a similar variations to those found in NTD Ge No12. If we apply a similar variation to NTD Ge No23 crystal for example it would have a range of values from $G_{ep}=0.2(W/K^{\alpha'+1})$ $\alpha'=4.5$ to $G_{ep}=0.1(W/K^{\alpha'+1})$ $\alpha'=4.75$. The difference in response given these variations is shown in figure 4.18. The two cases give FWHM resolutions of 7.2eV and 6.1eV for 5.899KeV x-rays. This is a considerable improvement on the previous prediction of FWHM 17eV using $G_{ep}=0.09(W/K^{\alpha'+1})$ $\alpha'=5$. It indicates that a favourable choice of crystal could be used to allow the realisation of resolutions close to the attenuation model predictions.

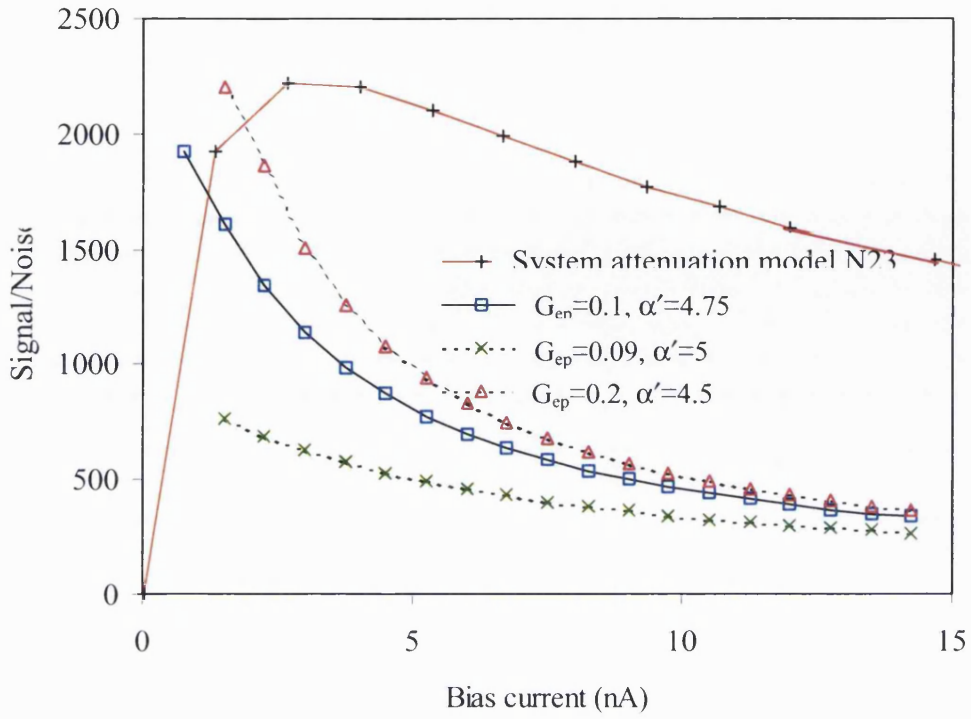

Figure 4.18 The modelled decoupled response of NTD Ge No 23 to 5.89 keV x-rays For a 1.5mm wire length with different wire lengths, with a $G_{ep}=0.2(W/K^{\alpha'+1})$ and $\alpha'=4.5$.

4.6 Conclusion

To summarise, the optimisation process indicates that it is probable that NTD Ge detectors can achieve a resolution comparable to that required for future x-ray spectroscopy. The optimisation exercise has not provided a definitive answer of how good a resolution can be achieved: this will require further experimentation. However, the optimisation process has proved valuable in determining the essential characteristics to achieving a high-resolution microcalorimeter.

Such characteristics are

- Low temperature operation in excess of that predicted by the figure of merit resolution typically close to 10mK.
- Very low noise JFETs ~ 3(nV/$\sqrt{Hz}$) voltage noise, preferably less.
- Low parasitic capacitance comparable to 7pF, preferably less.
- High conductivity thermal links.
- Small crystals ~20-40μm thick.
- The use of NTD Ge No 23 crystals preferentially selected to have low levels of decoupling.

It is expected that an FWHM resolution range of 3.5-10eV over a range 0.5 to 12 keV x-rays is possible.

5 Large format high resolution NTD Ge arrays

5.1 Introduction

The system optimisation exercise in chapter 4 indicated that it is theoretically possible to fabricate a comparatively high-resolution single NTD Ge microcalorimeter. Future x-ray missions will require large format arrays of such detectors. This is possibly the biggest drawback to using single NTD Ge crystals to create the pixel elements of such arrays. Such fabrication does not readily lend itself to the mass production of pixels. Another problem with SM in general is that the classical readout format requires that each individual pixel have an independent set of bias and readout electronics. For a large array, the number of wires necessary for the bias and readout electronics will place a prohibitive load on any potential cooling system. In this chapter the problems of translating the optimal high-resolution detector format into a reproducible pixel element, which can be readout in large numbers, are addressed.

5.2 New thermal link schemes

To create a high resolution detector the modifications indicated by the optimisation process need to be physically implemented. A corollary to this is that the final detector should be in a form that is conducive to the construction of a large array. In general, the modifications implied by the modelling process are straightforward. The biggest problem to overcome in the creation of a high resolution pixel will be the construction of an optimal thermal link. If 8μm diameter brass wires are used then the optimal link size will be typically 0.3 to 2mm long. These links must be capable of thermally isolating the detector whilst supporting it. In addition, they must provide the electrical link to the thermistor and not be dominated by the thermal boundary resistance. For array pixels, each detector would have to be created and installed manually. Previous experience at MSSL indicates that this would be technically very difficult. To address these problems two suggestions for alternative thermal links were investigated. These are a composite thermal link and a link utilising the thermal boundary resistance of the detector bonded directly to the heat sink.

5.2.1 Composite links

Composite thermal links have the obvious benefit that the thermal properties and the physical dimensions of the link can be tailored with greater flexibility. In this case the goal is to produce a composite link that will have a thermal conductivity comparable to that of two 0.2mm long, 8μm diameter brass wires in the 10mK region. It is subject to the constraints that the link does not significantly increase the heat capacity of the detector and is appreciably easier to manipulate.

The scheme chosen for the composite link was to use graphite as a low thermal conductivity core. At 10mK graphite has the lowest thermal conductivity of all elemental materials (3 orders of magnitude lower than that of brass[54]). A thin coating of metal could then be sputtered on to the graphite providing the thermal and electrical link to the detector. The graphite would provide the mechanical support; the choice and thickness of the metal film could be selected to give the link the desired thermal properties whilst providing electrical conductivity through the link. If copper is used as the sputtered coating, a relatively high conductivity link with small heat capacity can be created. It was found that a $200x600x1\mu m^3$

strip of graphite with a 5nm thick coat of copper on one side, has the equivalent thermal conductivity of a 0.2mm long, 8μm diameter, brass wire. Figure 5.1 shows a comparative plot of the modelled thermal power through a brass wire and composite link at a heat sink temperature of 10mK. The reason for choosing the particular size of graphite is that it allows the maximum bond area between the gold contact and thermal link to be realised.

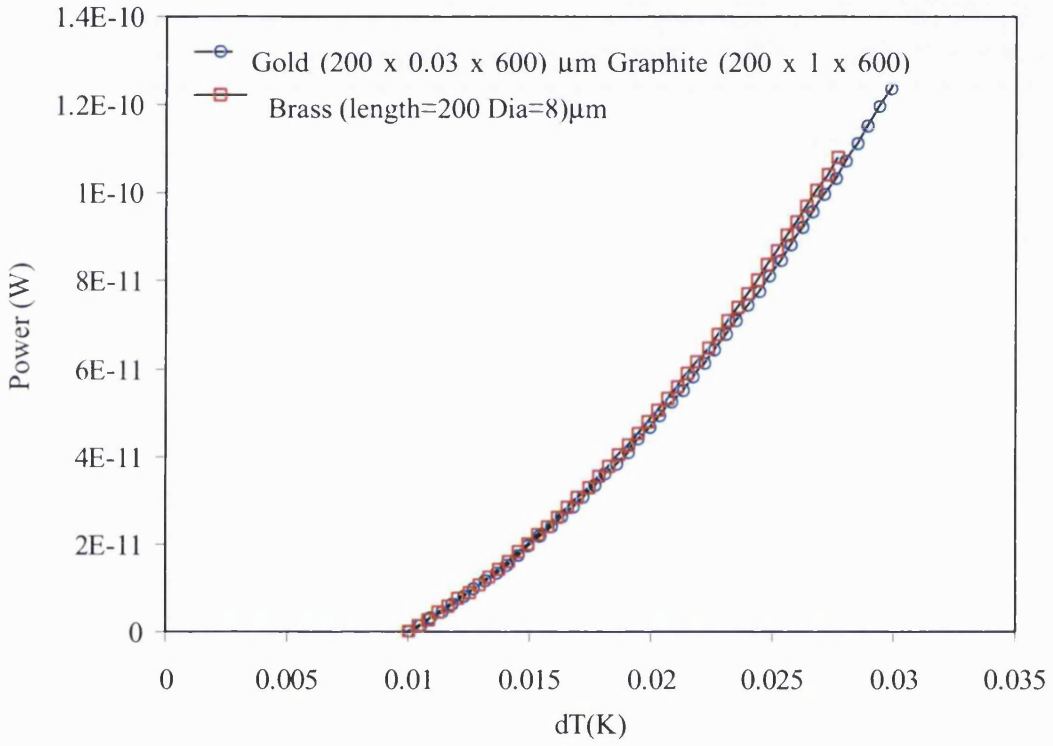

Figure 5.1 The expected thermal power across a composite thermal link compared to a 0.2mm long, 8μm diameter, brass link at 10mK. The composite link consists of a graphite strip with a layer of copper on one side.

The thickness of the link was dictated by the desire to keep the contribution to the overall heat capacity low whilst allowing the link to be reasonably robust. A schematic of the intended scheme is shown in figure 5.2. Electrical contact is made through the copper coating. The heat capacity of the links for the above case is estimated to be 3.99×10^{-15}J/K at 10mK. This is an improvement on the equivalent brass wire case having ~1/3 its heat capacity.

The problem with this scheme is the use of the H_{20} epoxy; at very low temperatures, metal filled epoxies like H_{20} actually impede the flow of phonons. At mK temperatures they behave as high pass filters to phonons because of their matrix like structure [72]. The metal grains in

the epoxy effectively increase the overall thermal resistance of the epoxy. The reverse is true at higher temperatures where the metal grains actually improve the thermal conductivity. This effect in H_{20} at 10mK was seen in figure 4.16, for a 1mm^2 contact area, its thermal resistance dominated the detector response at low bias currents. Here the maximum contact area achievable is the surface presented by the gold contact, in this case 200x200 μm^2. Both contacts provide a surface area of ~ 1/10 mm^2 giving a boundary resistance 10 times greater than that shown in figure 4.16. Effectively, the H_{20} epoxy will dominate the detectors thermal response out to high bias currents at 10mK.

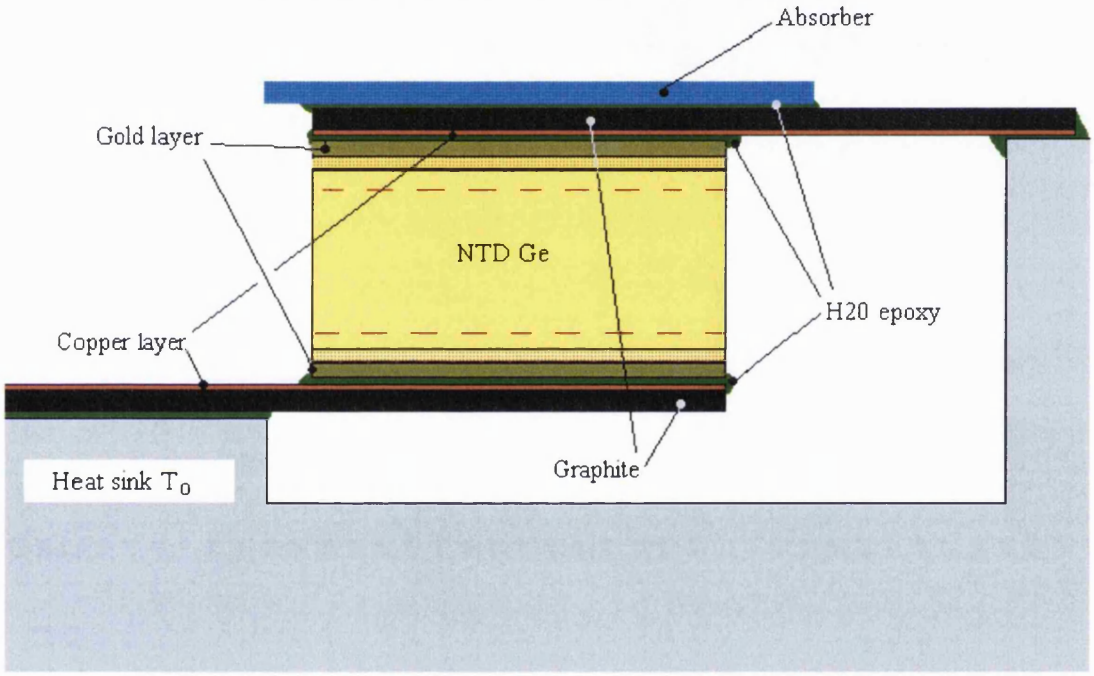

Figure 5.2 A schematic diagram of the intended composite link scheme. The links are shown edge on and are intended to extend as far back as the gold contact, maximising the contact area.

To eliminate this problem we must dispense with the use of H_{20} epoxy. A possible way to do this is to use gold for the metal coating on the links. Generally, the use of gold is less favourable than copper since it has a lower thermal conductivity and higher heat capacity. To achieve the same thermal response the link would require a 30nm thick coating of gold. This would increase the heat capacity of the link to 5.09×10^{-15} J/K at 10mK. This is still less than the brass wire case. However, since both the surfaces of the link and crystal are now gold it is possible to bond the link using a eutectic bond. This should be much more thermally transparent than the silver filled H_{20} epoxy bond. This needs to be verified experimentally.

The composite thermal link scheme, although increased in complexity should make the creation of a single detector easier in terms of manipulation. However, it does little to facilitate the production of a large array, since the elaborate thermal links still need to be incorporated into an array.

5.2.2 Boundary resistance

The goal of the modelling was to reproduce a link, thermally comparable to two 0.2mm long 8μm diameter brass links, but making the detector much easier to fabricate and place in an array. A second way to achieve this is to dispense with the thermal links altogether, and use the thermal boundary resistance of detector bonded directly to the heat sink as the thermal link. As mentioned above we cannot use a H_{20} epoxy bond to do this. This creates a problem since using a metal filled epoxy is an easy way to make thermal and electrical contact to the thermistor.

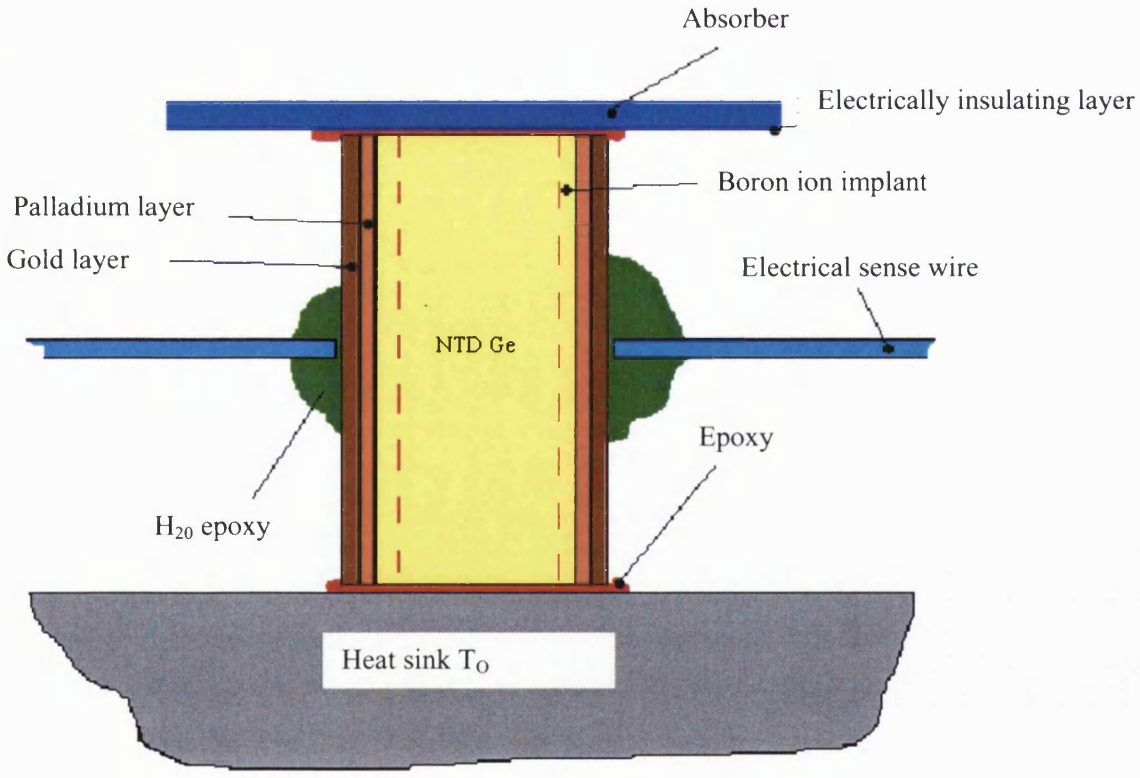

Figure 5.3 A modified detector in which the roles of sense wire and thermal link have been separated. This scheme uses a high thermal conductivity epoxy bond to provide the thermal link between the absorber, detector and heat sink. Low thermal conductivity electrically conducting wires bonded to the electrical contacts as sense wires.

A way around this problem is to separate the roles of thermal link and electrical sense wires. This technique has been used before [21]. The scheme envisioned here differs in the nature of the thermal links used and is shown in figure 5.3. It is assumed the electrical contact is a thin electrically conducting strip having a low thermal conductivity and heat capacity and thus plays no thermal role in the detector. A small amount of H_{20} epoxy is used to make electrical contact between the detector and contact strip. A non-metal filled epoxy is chosen to bond the absorber, detector and link to the heat sink. These joints need to have a low thermal boundary resistance. For this reason a non metal filled high thermal conductivity epoxy can be used, for example Epibond-121. No data are available on the thermal resistance of a specific {NTD Ge\Epibond-121} interface at 10mK. However, there is data on a range of {metal\Epibond-121\ Mylar\Epibond-121\Mylar\metal} interfaces down to 50mK [66]. These interfaces give a range of boundary resistances, and since the {Epibond-121\Mylar} interface is common to all the bonds tested, any change must be attributable to the {metal\Epibond-121} region of the bond. The different metals in the bond alter its thermal conductivity.

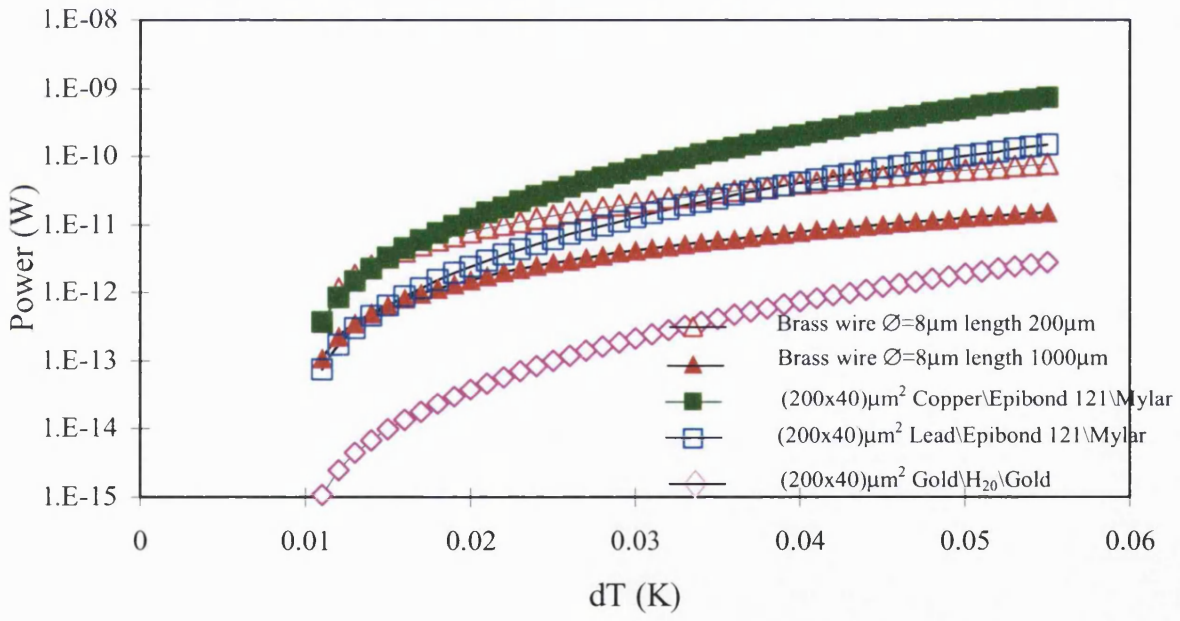

Figure 5.4 The expected power across the thermal boundary resistances of high conductivity epoxy interfaces. Compared to brass wires and the thermal boundary resistance of a H_{20} epoxy bond. All calculated as a function of the temperature difference dT across the link at 10mK.

If the 50mK values are extrapolated to 10mK as shown in figure 5.4, an idea of the expected power through a {NTD Ge/Epibond-121} joint can be obtained. In the figure these values are

compared with brass wires having lengths, 0.2 and 1mm long (these lengths are close to the optimal range of values indicated by the optimisation models). The thermal power through such interfaces is found to be comparable to that through the wires. The area of the Epibond 121 bond has been scaled for the area presented by the detector to the heat sink $40x200\mu m^2$, shown in figure 5.3. The values are also compared with the extrapolated values for gold\H20\gold bond of the same area, the conductivity of this bond is much lower then the Epibond 121 joints.

The conclusion is that an Epibond 121 (or another high conductivity epoxy) bond can be tailored to have thermal conductivity comparable to that of an ideal thermal link. This scheme has advantages that make it much simpler to create a single detector and construct large arrays. This scheme is described in section 5.4.2. Overall the boundary resistance link looks favourable from the initial modelling results and needs experimental verification. It may prove very hard to manufacture a consistent thermally specific boundary resistance, since the exact thermal properties of any boundary resistance are related to the surface properties of the interface [71].

5.3 Standard microcalorimeter array format

The typical method to connect an array of microcalorimeters is to wire each detector as an independent entity. The largest x-ray microcalorimeter array that has been produced using this method has been an array of 2 rows of 18 pixels as shown in the schematic on figure 5.5. This is the array designed by GSFC group. Two versions of it were created; one was successfully flown on a sounding rocket flight to observe the diffuse x-ray background, the other was flown as the detector array for the XRS instrument on the ill fated Japanese x-ray mission Astro-E that was launched in February 2000.

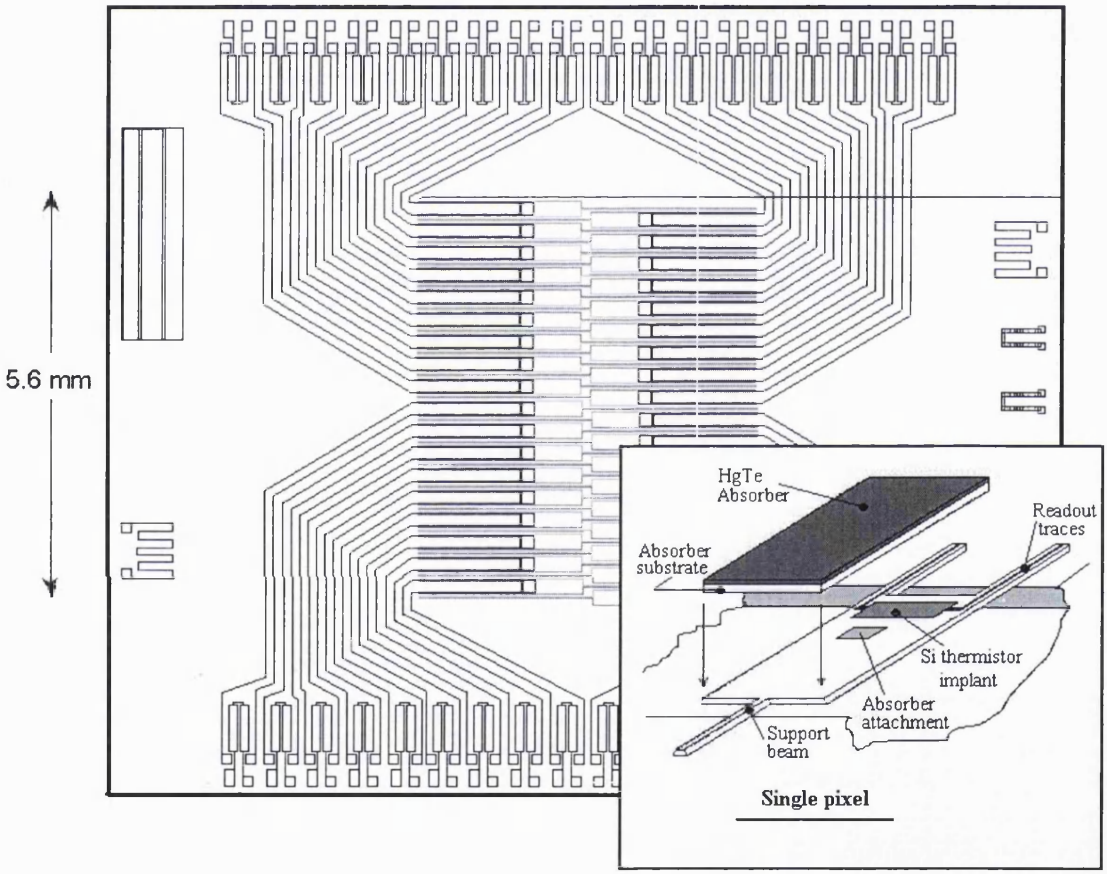

Figure 5.5 A schematic of the 36 element, GSFC bilinear microcalorimeter array (Adapted from [73])

Some of the limitations inherent in creating microcalorimeter arrays using the standard array formats are visible in the diagram. To ensure that each pixel is thermally independent an elaborate thermal link scheme needs to be accommodated. This reduces the filling factor of

the final array and complicates the assembly process. To accommodate the wiring necessary and simplify the readout, the array has an elongated shape two rows deep. It is unlikely this scheme can be extended to a larger array, more than three rows deep along one of the array axes. An additional problem with this array format is that the number of wires needed to connect to the cold stage in order to bias and readout each pixel places a large thermal load on the cooling system. This is not a big problem with the GSFC bilinear array because of its limited size, future arrays are likely to contain of the order of 100 x 100 pixels. Arrays of this size using the above scheme will need at least (100 x 100 + 1) independent bias wires and (100 x 100) readout wires connected to the array.

An estimate of the heat load can be made assuming conventional 10μm Constantan wires. Constantan is a commercially available low thermal conductivity wire commonly used in cryogenic applications. Its conductivity spans ~ $9x10^{-3}$– $9x10^{-2}$ (W/cm K) for the temperature range of 0.01-4.2K. If we assume that these wires are independently heat sunk at 4.2 K and travel a distance of 10cm to the array, at 10mK then each wire will contribute a thermal load of ~ 6nW. The entire wiring of a future array could have a parasitic heat load of 124μW on the cold stage. It is not possible to sustain this load with current cooling technologies. A space borne ADR, for example could theoretically sustain a heat load of 1μW for 2 hours or 100nW for 20 hours [74]. This is a pessimistic example, more exotic composite wires could be used, which would reduce the thermal load. Nevertheless, this example still illustrates the importance of the need to reduce the number of wires into the array.

5.4 New array readout scheme

If a large array of NTD Ge detectors is to be manufactured, a new simplified readout scheme has to be adopted, grouping detectors to minimise the number of readout channels. A scheme similar to that employed to read CCD arrays could be used. CCD arrays store charge, allowing the array to be readout along common row and column lines by accessing the charge at a later time and reconstructing the original image, by recording the position of the read charge.

5.4.1 Reduced readout channel format.

The CCD type readout cannot be implemented in a straightforward manner for microcalorimeters. By coupling the detector outputs in rows and columns the entire detector outputs end up connected together. This means we lose the spatial information contained in any detected pulse, essentially creating a single detector.

By introducing diodes into the standard picture, it is theoretically possible to create a readout scheme similar to that of CCD. The diodes can be used to control the directions of voltage pulses from individual detectors and constrain them to remain within a given row and column. The basic scheme is shown in figure 5.6. From the figure, any voltage pulse registered in any detector is prevented from contaminating the outputs of other detectors by diodes. This makes it possible to read events in any row or column using a single preamplifier stage, greatly simplifying the readout electronics.

Unfortunately, because of carrier freeze out, diodes will not operate at very low temperatures, therefore they cannot be sited on the array substrate. They should be able to operate at 110K since this is the temperature at which JFET preamplifiers operate. This has an unfortunate consequence in that the number of wires into the cold stage of the array must remain the same as in the conventional case. However, such a scheme will reduce the number of readout channels needed to access the array simplifying the wiring of later stages.

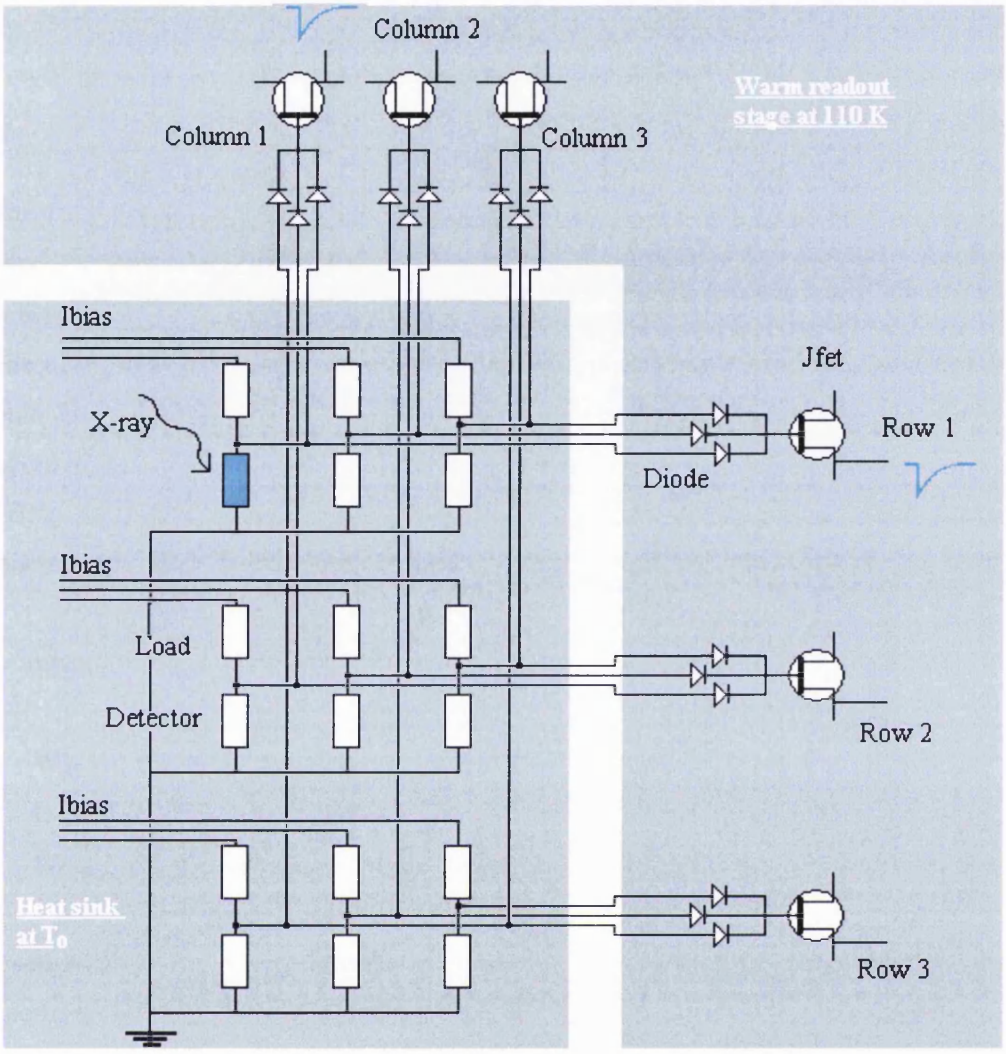

Figure 5.6 A schematic of a 3x3 array utilising the proposed reduced readout channel scheme.

We can estimate the noise from such a scheme, assuming the diode adds no significant noise, since the noise at the preamplifier input of a pixel consisting of a detector load pair V_{pixel} is given by

$$V_{pixel} = \sqrt{\left(V_P^{\,2} + V_{JD}^{\,2} + V_{JL}^{\,2}\right)} \qquad \text{- 5.1}$$

where V_P is the phonon noise, V_{JD} the detector Johnson noise and V_{JL} the load Johnson noise. These noise components are defined in equations 2.32 2.33 2.34 respectively. For N pixels in the same line the noise at the preamplifier input will be given by

$$V_{Line} = V_{pixel}\sqrt{N} \qquad \text{- 5.2}$$

Hence the degradation from using the proposed scheme is that the Johnson noise and phonon noise increase by a factor $\sqrt{N}$ for N pixels, compared to the single detector case. As shown in section 4.4 at 10mK the dominant noise component of the system is the JFET voltage noise. This is ~ 3 times greater than the other noise components. This implies that such a scheme could be used to readout 9 pixels using a single JFET without suffering significant noise degradation. For example, a (90x90) array each row and column would need at least 10 JFETs. This would give (10x90+10x90) or 1800 readout channels to access the entire array. This is a significant saving on the (90x90) or 8100 required using the conventional method.

To implement this scheme there are a number of issues which need to be addressed:

- Will a diode operate at 110K?
- Is it possible to bias a JFET through a diode?
- Would the diodes contribute significantly to the system noise?

A series of experiments was performed on a selection of typical diodes in an attempt to experimentally address these questions. The diodes tested were a JPAD5, IN4942GP and the gate\source junction of an IFN140 JFET.

5.4.1.1 Diode operation at 110K

All the diodes were mounted on an independent temperature stage inside a cryostat, which was held at 110K. The VI characteristics across the diode were plotted and it was found that all the diodes tested exhibited typical diode VI's with the conclusion that all the diodes could operate at 110K.

5.4.1.2 JFET biasing through the diodes

Some experiments were run to test the feasibility of biasing a JFET through a diode at a temperature of 110K. The biasing scheme was compatible with that intended for use on the

array readout described above and shown in figure 5.6. Examining the figure, we see that the leakage current from a diode would follow the same route to ground through the detector as the bias current. This was initially a matter of concern. If the leakage current were comparable to the bias current, it could affect the detector operation.

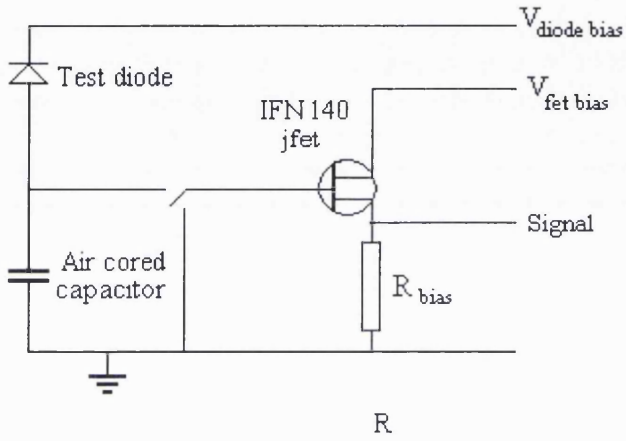

Figure 5.7 Leakage experiment run at 110K to measure the leakage current of the diode.

To assess this, the leakage current of the diodes was measured as follows. Using the circuit shown in figure 5.7, the JFET input was switched to ground to allow the JFET to bias. Once the JFET had stabilised (typically this was a few minutes), the Input Short (IS) noise was recorded at the output using a spectrum analyser. The IS noise is the noise at the JFET output with the input shorted to ground. The input was then switched to the diode capacitor line and the output noise recorded. By doing this the leakage current, I_L from the diode and JFET produce a spectral voltage across the impedance of the known capacitance, C, that rolls off as

$$V_L=I_L/j\omega C \qquad \text{- 5.3}$$

At the signal output, this noise voltage V_L adds in quadrature with the IS noise from the JFET, to give a final noise profile. By recording the IS noise prior to each test, it could be extracted later allowing the leakage current to be estimated. A recording of a leakage current trace for an IFN140 JFET gate\source junction 'diode' is shown in figure 5.8.

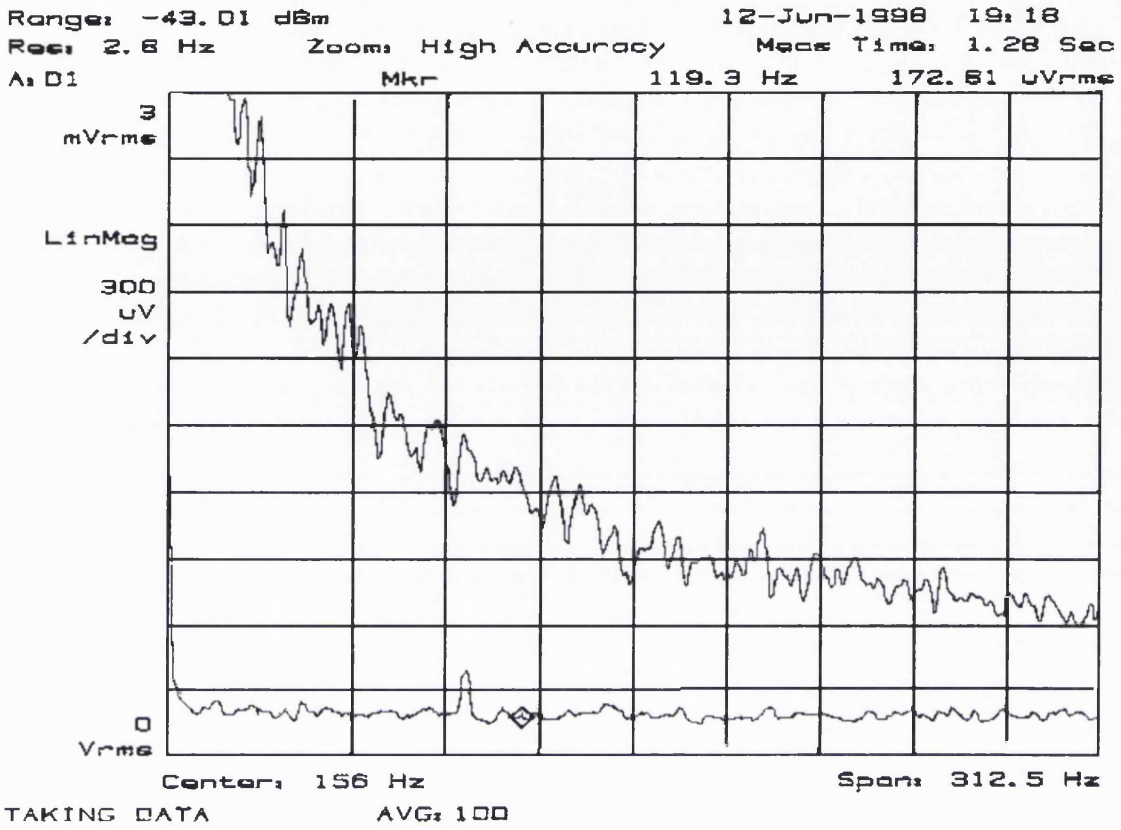

Figure 5.8 Spectrum analyser output from the leakage current tests. The diode was the gate source junction of an IFN140 JFET. The lower trace is the JFET IS-noise and the upper the Quadrature sum on the JFET IS-noise and leakage voltage V_L from the diode and JFET leakage currents. The results of the leakage current experiment for the tested diodes are shown in figure5.9.

The experiment was then repeated without the diode present allowing the leakage current from the JFET to be estimated. The test was repeated for all the diodes selected. The results of these tests are shown in figure 5.9. Each plot has been corrected for JFET IS noise and JFET leakage current.

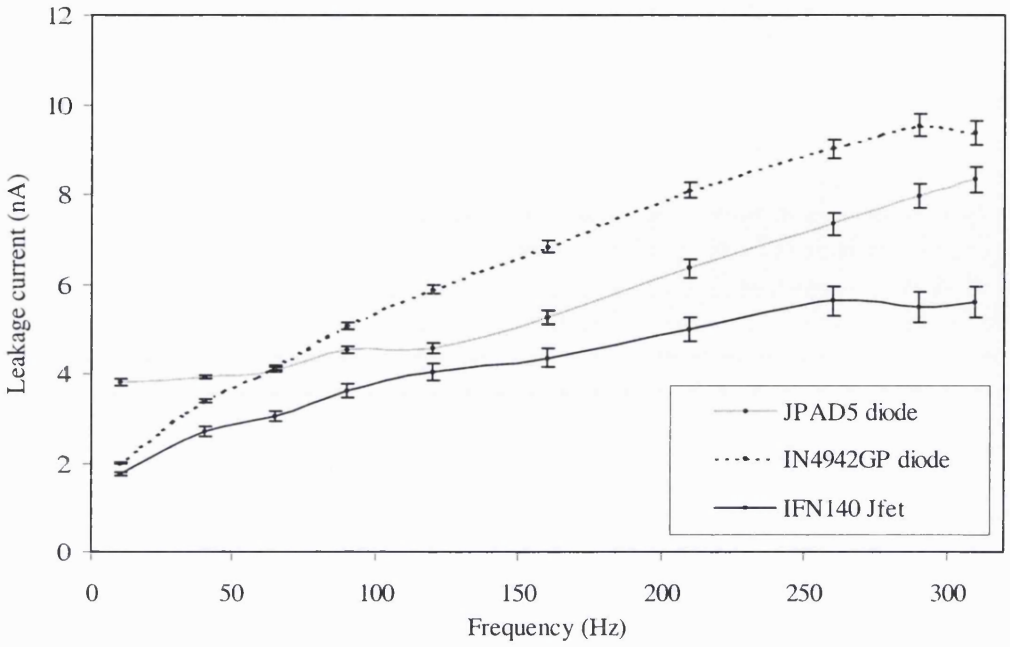

Figure 5.9 Experimentally determined diode leakage currents at 110K. The errors are estimated from the local noise spread evident on the spectrum analyser voltage traces.

Once the leakage currents of the diodes had been measured, a test was run to assess the feasibility of biasing a JFET through a diode as the scheme outlined in figure 5.6 requires. The experimental circuit used is shown in figure 5.10.

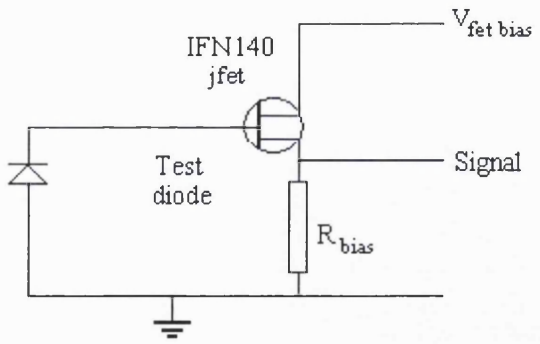

Figure 5.10 The circut of the diode biasing and noise experiment. The diode was run at 110K.

This experiment found it was possible to bias the JFET through a diode, but only with the IN4942GP diode: both others failed. The reason suspected for this was their lower leakage current. The JFET gate/source diode by its nature will have a leakage current comparable to the JFET, and on figure 5.9 we see that the JPAD5 diode has a leakage current close to this. It is thought that there was a build up of charge at the gate of the JFET because the JFET

leakage current had to flow through the reversed junction diode. For this to succeed the leakage current of the diode must be at least equal to the leakage current of the JFET. If this is not the case the charge will build up at the JFET input, leaving the JFET with a floating gate, which switches the JFET off. The leakage current measured for the IN4942GP diode was the largest of those measured and allowed the JFET to bias through the diode without switching the JFET off.

5.4.1.3 Additional diode noise

Having confirmed the feasibility of biasing the JFET through the diode; the test was rerun with the JFET biased in this manner. This was to assess the extent of any additional noise at the JFET output caused by the inclusion of the diode.

The experimentally obtained noise was compared to the JFET IS noise; the result is shown in figure 5.11. It was found that the IN4942GP diode added significant 1/f noise to the JFET output. The diode 1/f noise dominates the system noise out to ~ 0.7KHz where the diode noise dropped below the input noise of the JFET. Four different IN4942GP diodes were re-tested to eliminate the possibility that the tested diode was anomalous. All the diodes exhibited similar 1/f noise levels. The noise performance of the diode was expected to be small, clearly this was not the case. However, the scheme is still promising and requires more tests to see if a low noise diode can be found.

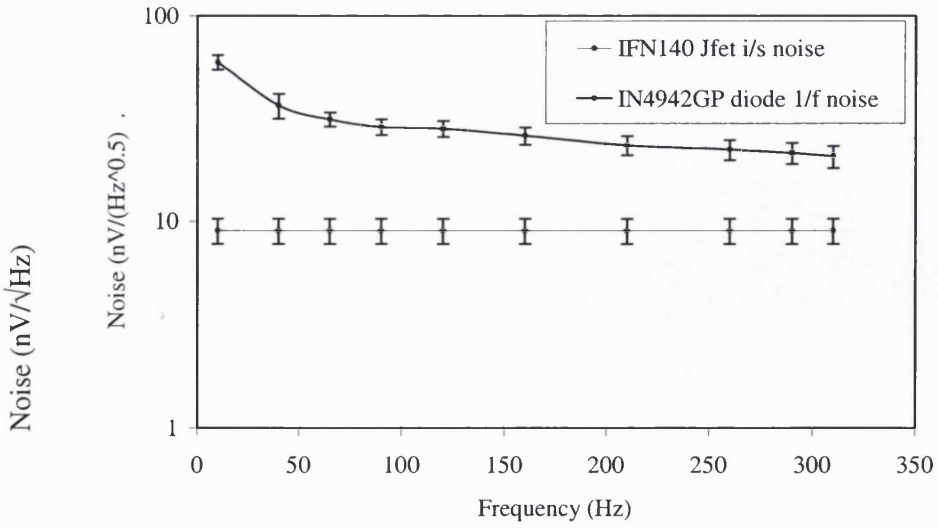

Figure 5.11 Additional 1/f noise from IN4942GP diodes at 110K. The lower trace is the JFET IS noise.

5.4.2 Multiplex readout scheme proposal

A second array readout method was investigated. The scheme offers true multiplexed readout, which reduces the number of wires into the array itself. The scheme is shown in figures 5.12 and 5.13. The intention is to utilise the separated roles of electrical and thermal links presented in section 5.22 and shown in figure 5.3, for the pixel element, to effect a new readout scheme.

Since the thermal and electrical roles are separated, it is now possible to use two thermistors with a common absorber. Now both thermistors can thermally sense an x-ray event. Electrically one thermistor of each pixel is wired in series with the corresponding thermistor on all other pixels in that row. This provides a continuous path along each row and column of the array. The bias current I_b is continuous throughout each row and column. Any x-ray event sensed in a thermistor inducing a resistance change dR will, in the usual manner, create a corresponding voltage change $dV=I_b.dR$ at the row or column output.

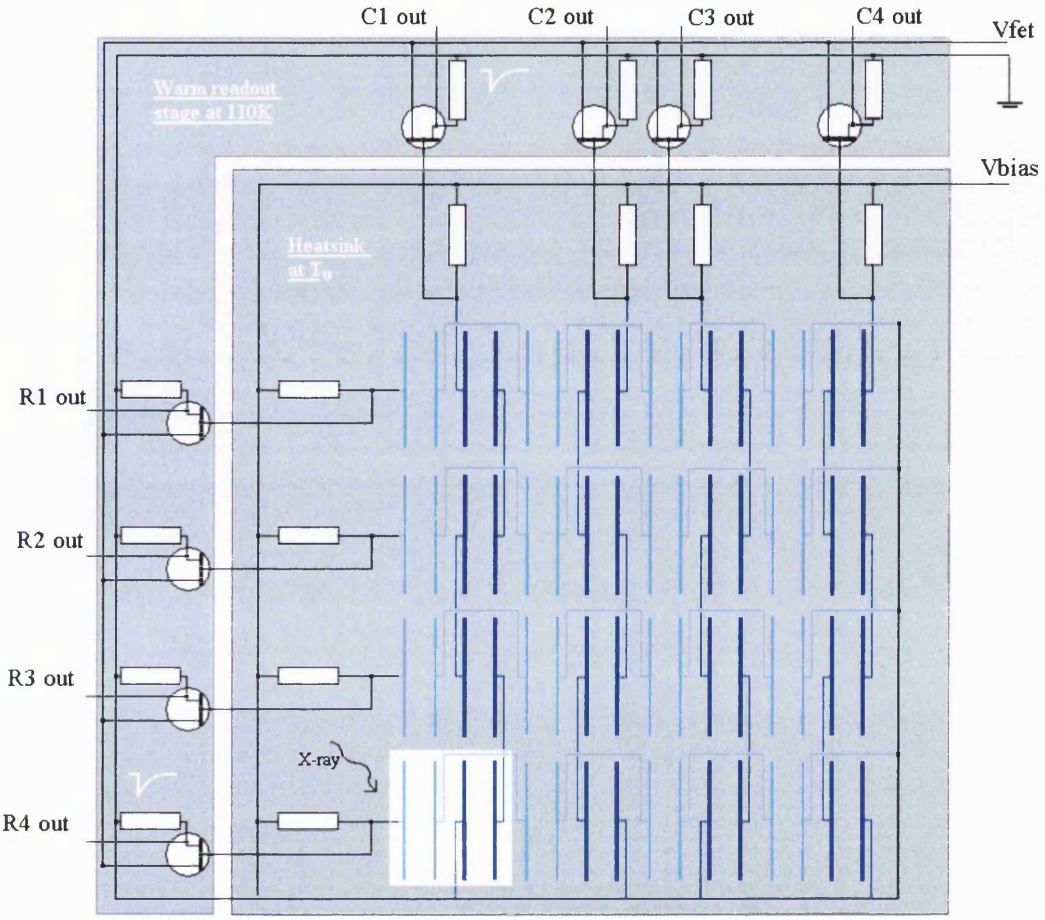

Figure 5.12 Intended wiring format of multiplexed array showing x-ray position sensing. The intended pixel is showed in figure 5.13.

As there are two thermistors only one needs to be spectroscopically accurate, the other only has to provide the spatial information for the event. For example, all the rows could be constructed to have low noise a JFET at their outputs. Within the row, thermistors in each pixel are selected to have particularly low decoupling levels and low values of R_o and T_g. This would allow the pulse to be accurately sampled giving a high resolution. The column thermistors need not be very accurate as they just have to sense the event and spatially tag it. Accordingly, the column JFET need not have a high noise performance. Combining the data, we have an accurate x-ray pulse along with its X and Y co-ordinates. There is a penalty from having two thermistors, the heat capacity is increased which reduces the responsivity. However this may be offset by using two thinner crystals, giving an overall heat capacity equivalent to one 40μm thick thermistor, which was the optimal thickness arising from the modelling of crystal size in section 4.2.4.

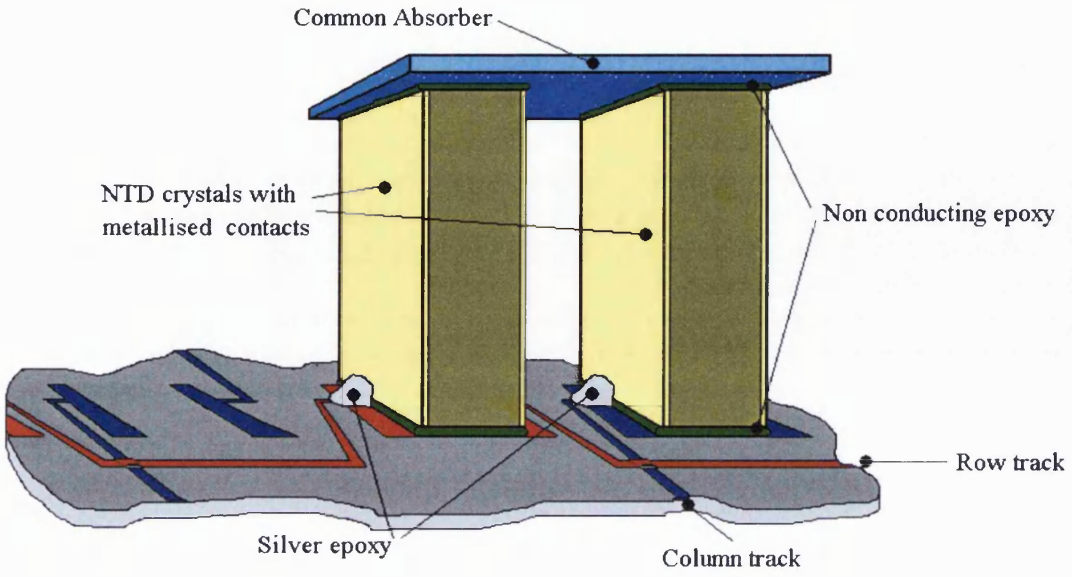

Figure 5.13 Intended format of multiplexed pixel. Array wiring is shown in figure 5.12.

Another penalty from running detectors like this is an increased level of noise. This occurs since at the input of each JFET a line of N detectors will have a resultant noise voltage given by

$$V_{Line} = \sqrt{N\left(V_P^{\,2} + V_{JD}^{\,2}\right) + V_{JL}^{\,2}} \qquad \text{- 5.4}$$

If we are to simulate a constant bias current comparable to the single microcalorimeter case then the value of R_L needs to be scaled appropriately i.e. by a factor N for N detectors in series. This means the load noise is the same as for the reduced readout scheme presented earlier, since V_{JL} is N times greater as R_L is increased to $R_L=NR_L$. So the overall effect is to increase the phonon and Johnson noise by a factor $\sqrt{N}$. As pointed out earlier, at 10mK the JFET voltage noise dominates the other noise sources by a factor of 3. This implies that 9 detectors can be wired in series with out any major degradation in the resolution. Longer lines of pixels can be readout by segmenting them into 9 pixel lengths, with an appropriate increase in the numbers of JFET. The spatial thermistors, in which resolution is not important, can be wired in much longer segments.

The (90x90) element array could be readout along its columns by 3 JFETs with each column segmented into three lengths of 30 pixels. The rows would require 10 JFETs with each row being broken up into ten segments of 9 pixels. The result is that there are (10x90+3x90) or 1170 JFETs, 900 of which need to have a good noise performance. The thermal load into the array is dramatically reduced from the standard case. Taking the example given in section 5.3, the estimated load of 124μW can be considerably reduced using this scheme. If we assume the array is readout as 100 separate rows of 11 individual 9 pixel spectroscopic segments (the last spectroscopic pixel is omitted for simplicity) and 100 columns, of say 3 individual 33 pixel spatial segments. This gives (100x11+100x3) lines to the array with a heat load of ~1μW. Which is compatible with the cooling power expected for future ADRs on spacecraft.

5.5 Future for large format NTD Ge arrays.

The work presented in this chapter has shown that it is may be possible to achieve considerable savings on the conventional techniques used to build microcalorimeter arrays. The savings are both in terms of thermal load and construction effort. It implies that a 100x100 element array of NTD Ge microcalorimeters is capable of being cooled by a space based ADR to 10mK, giving a hold time of ~2 hours, for a pessimistic case using Constantan wire. A more suitable choice of wires and optimal set up could improve the hold time considerably. In terms of array manufacture, the dual thermistor readout scheme is expected to be much simpler to create. The pixels simply need to be bonded to the prelaid tracks on the substrate and the absorbers bonded to the tops of the thermistors. One can imagine the possibility of semi-automating this process.

The greatest problem may not be the construction of the actual array, but obtaining crystals to make it. This is because of electron-phonon decoupling, which means that each spectroscopic crystal may have to be selected for low levels of decoupling before it is incorporated into the array. A 100x100 array would require the individual selection of 10000 spectroscopic grade crystals. This would require a vast effort. To take a conservative example if it is possible to record the VI of 10 crystals at one time in a cryostat, it would take at least 1000 cool downs to find enough good crystals to create the array. Ultimately, it may not prove possible to create very large arrays of NTD Ge microcalorimeters. However, NTD Ge may still prove invaluable in the fabrication of small to mid sized arrays with less than 1000 elements.

6 Conclusion

The work presented in this thesis set out to address whether a NTD Ge SM could be used to create the pixel element of a high resolution x-ray spectroscopic imaging array.

Numerical modelling was used to predict the resolution attainable from a complete microcalorimeter system subject to;

- Attenuation from the electrical system,
- Non-linear detector response during the detection of energetic x-rays,
- Electron-phonon decoupling in the thermistor,
- Modified hopping conduction due to the electric field across the thermistor.

All these effects conspire to prevent a semiconductor detector from achieving its theoretical resolution. Using the models ways of achieving an optimal system resolution in light of these effects were investigated.

The optimisation process predicted that NTD Ge detectors can achieve resolutions comparable to that required for future x-ray spectroscopy. A resolution in the range of 3.5eV to 10eV, over the 1 to 10 keV x-ray range, is expected. This resolution is comparable to the 2eV goal expected from future detectors. To achieve such resolutions with NTD Ge SM optimisation indicates the following characteristics need to be implemented

- Low temperature operation in the region of 10mK,
- A low noise preamplifier with an input short noise $\leq 3(nV/\sqrt{Hz})$,
- A low parasitic capacitance in the system preferably $\leq 7pF$,
- High thermal conductivity links,
- Small size: crystals $200\mu m^2$ and 20-40μm thick,
- The use of preferentially selected NTD Ge No 23 crystals.

Novel ways of creating large arrays of NTD Ge SM were investigated. In particular methods to help reduce the large number of readout channels and the thermal loads imposed by these future arrays were investigated. It was shown that it is theoretically possible to create a large array, which is capable of being cooled with the typical power provided from a future space borne ADR cooler. In addition, it is shown that the number of readout channels needed for these arrays is considerably reduced, creating a fully multiplexed readout.

The multiplexed readout is created by separating the role of electrical readout and thermal link within each pixel. By using two thermistors per pixel, each bonded to the heat sink to provide the thermal link, each row and columns of the array may be electrically wired in series creating the multiplexed readout. This scheme has an additional benefit, it addresses some of the fabrication problems created by the monolithic nature of NTD Ge SM, the amount of manipulation needed to create the pixels using this method is much less than conventional means.

7 References

[1] K. O. Mason: "The Next Generation of X-Ray Observatories: Workshop Proceedings", Leicester England , (10-12 July 1996), P21.

[2] A. C. Fabian: "The Next Generation of X-Ray Observatories: Workshop Proceedings", Leicester England , (10-12 July 1996), P15.

[3] Science with the Constellation-X Observatory: Editors: J. Bookbinder, H. Tananbaum, P. Tyler, A. Valinia, K. Weaver, and N. White. Jan 1999. At http://constellation.gsfc.nasa.gov in pdf .

[4] At http://heasarc.gsfc.nasa.gov/docs/rosat/rosgof.html

[5] At http://heasarc.gsfc.nasa.gov/docs/asca/

[6] At http://asc.harvard.edu/

[7] At http://sci.esa.int/xmm/

[8] At http://chandra.harvard.edu/

[9] The Basic Design Goals Of The XEUS Observatory: At http://astro.estec.esa.nl/SA-general/Projects/XEUS/, Last update: June 01 17:11 1999 by M. Bavdaz.

[10] N. E. White, H Tananbaum, S. M. Kahn, "The Next Generation of x-ray Observatories: Workshop Proceedings", Leicester England, (10-12 July 1996), P173.

[11] High throughput x-ray spectroscopy mission, Technology roadmap, Compiled by HTXS Mission Study Team, P13-21: At http://constellation.gsfc.nasa.gov/roadmap/part2b.pdf

[12] The Next Generation x-ray Observatory High Throughput Spectroscopy: At http://lheawww.gsfc.nasa.gov/docs/xray/ngxo/figure2.html.

[13] D. McCammon, M. Juda, J. Zang, S.S Holt, R.L Kelley, S.H Moseley and A.E Szymkowiak: Japanese Jrnl Appl Phys Suppl, Vol 26 (1987),P2084

[14] S.H. Mosley, R.L Kelley, R.J Schoelkopf, A.E Szymkowiak, D McCammon and J. Zang: I.E.E.E. Transactions on nuclear science, Vol 35 No1 (1988), P59

[15] S.H. Mosley, M Juda, R.L Kelley, D McCammon, C.K Sthale, A.E Szymkowiak and J. Zang: Proceedings of an E.S.A Symposium on photon detectors for space instrumentation at Noordwijk, E.S.A SP_356 (1992), P13

[16] D. McCammon, W. Cui, M Juda, J Morgenthaler, J. Zang, R.L Kelley, S.S. Holt, G.M Madejski, S.H. Mosely and A.E Szymkowiak: Nucl Instr and Meth, Vol A326 (1993), P157

[17] C.K. Stahle, R.L Kelley, D. McCammon, S.H. Mosely and A.E Szymkowiak: Nucl Instr and Meth, Vol A370 (1996), P173

[18] D. McCammon, R. Aluvy, S. Deiker, J Morgenthaler,R.L Kelley, F.J Marshall, S.H Moseley, C.K Sthale and A.E Szymkowiak: Nucl Instr and Meth, Vol A370 (1996), P266.

[19] S.Deiker, R. Kelley, A. Lesser, D. McCammon, F.S. Porter, W.T. Saunders C.K. Sthale and A.E. Szymkowiak: "Proceeds 7th Int Workshop on Low Temp Detectors", Munich Germany, (27 July-2 Aug 1997), P108.

[20] E. Silver, S. Labov, F. Goulding, N. Madden, D. Landis, J. Beedman, T. Pfafman, L. Melkonian, I. Millet and Y.Wai: S.P.I.E "Proceedings of EUV,X-Ray and Gamma-Ray Instrumentation for Astronomy and Atomic physics". San Diego, California, Vol 1159, (1989), P423.

[21] M. Legros, E. Silver, N. Madden, J. Beeman, F. Goulding, D. Landis, E. Haller: Nucl Instr and Meth, Vol A345(1994), P492.

[22] I.D. Hepburn ,P.A.R Ade, M.J. Griffin, W.S Holland, J.L. Culhane, R. Kessel and D.M Walton; In Low temperature detectors for neutrinos and dark matter - II, ed L.Gonzales-Mestrees and D. Perret-Gallix, Frontieres (May2-6 1988),

[23] R. Kessel, D.M Walton, J.L Culhane, I.D. Hepburn , P.A.R Ade, M.J. Griffin W.S. Holland : "S.P.I.E Proceedings of x-ray instrumentation", San Diego California, Vol 1140, (1989) P423.

[24] F.V. Feilitzsch, T. Hertrich, H. Kraus, Th. Peterreins, F. Probst and W. Seidel: Nucl. Instr. and Meth. A271 (1988), P332.

[25] D.Twerebold: Europhys. Lett. 1 (1986), P109.

[26] P. Verhoeve, N. Rando, P. Videler,A. Peacock, A Van Dordrecht: SPIE x-ray and UV Spectroscopy and polarimetery, Vol 2283 (1994), P172.

[27] N.E Booth: Appl Phys Lett. 50 (1987), P293.

[28] M. Frank, C.A. Mears, S.E Labov, F. Azgui, M.A Lindenman, L.J. Hiller,H. Netel, A.T Barfknecht: Nucl Instr and Meth. A 370, (1996), P41.

[29] Roland den Hartog, P. Verhoeve, A. Peacock, A. Poelaert, N. Rando Applied Superconductivity Conference, Palm Desert, CA, (13-18 Sept 1998), Submitted.

[30] C. Erd, A. Poelaert, P. Verhoeve, N. Rando, A. Peacock: SPIE x-ray and UV Spectroscopy and polarimetery, Vol 2518 (1995), P268.

[31] U. Nagel, A. Nowak, E. Kellner, H.J. Gebauer, P. Colling, S. Cooper, D. Dummer, P. Ferger, M.Frank, G. Forster, J. Igalson, A. Nucciotti, F. Probst, A. Rulofs, W. Seidel and L. Stodolsky: Jrnl of Low Temp Phys,Vol 93, Nos 3-4 (1993), P543.

[32] F.V. Feilitzsch,T. Hertrich, H.Kraus,T.H. Peterreins, F.Pbrost and W.Seidel: Nucl Instr and meth, Vol A271 (1988), P332.

[33] F, Probst, S. Cooper, D. Dummer, W. Seidel: Low temp Particle detectors for Neutrinos and Dark matter IV, Oxford, England, (Sept4-7 1991), 193-201

[34] K.D Irwin, G.C. Hilton, D.A Wollman and J.A. Martinis: Appl. Phys. Lett., Vol 69 (13) (1996), P1945.

[35] D. A. Wollman, K. D. Irwin, G. C. Hilton, L. L. Dulcie, D. E. Newbury and J. M. Martinis. Journal of Microscopy 188(3) (December 3, 1997), P223.

[36] K. D. Irwin, G. C. Hilton, D. A. Wollman, and J. M. Martinis, Journal of Applied Physics 83(8), (April 15 1998), P3978

[37] D. A. Wollman, K. D. Irwin, G. C. Hilton, L. L. Dulcie, N. F. Bergren, D. E. Newbury, and John M. Martinis, to be published in Proceedings of the 14th International Congress on Electron Microscopy.

[38] S.H Moseley, M. Juda, R.L Kelley, D. McCammon C.K. Stahle, A.E Szymkowiak, J.D Zhang: Proceeds of an ESA Symposium on Phonon Detectors for Space Instrumentation, ESTEC Noordwijk, Netherlands (10-12 Nov 1992), P13.

[39] B.I. Shklovskii and A.L. Efros ; Electronic properties of doped semiconductors, Solid state sciences Vol 45, Springer and Verlag (1984)

[40] E. Auborg, A Cummings, T. Shutt, W. Stockwell,P.D Barnes, A Da Silva, J Emes, E.E Haller,A.E, Lauge, R.R Ross, B. Sadoulet, G. Smith, N. Wang, S. White, B.A. Young, D. Yvon: Jrnl. of Low Temp. Phys. Vol 93 No 3-4 (1993), P289.

[41] K.M. Ioth, W.L. Hansen, J.W. Beeman, E.E. Haller, J.W. Farmer and V.I. Ozhogin: Jrnl. of Low Temp. Phys. Vol 93 No 3-4 (1993), P307.

[42] S.M Grannan, P.L Richards, M.K Hase: Int. Jrnl. of IR. and mm. Waves, Vol 18 (1997),P319

[43] E.E. Haller: Instrumentation in Astronomy VIII SPIE Proc. 2198 (1994), P630.

[44] E. Auborg, A Cummings, T. Shutt, W. Stockwell,P.D Barnes, A Da Silva, J Emes, E.E Haller,A.E, Lauge, R.R Ross, B. Sadoulet, G. Smith, N. Wang, S. White, B.A. Young, D. Yvon: Jrnl. of Low Temp. Phys. Vol 93 No 3-4 (1993), P289.

[45] K.M. Ioth, W.L. Hansen, J.W. Beeman, E.E. Haller, J.W. Farmer and V.I. Ozhogin: Jrnl. of Low Temp. Phys. Vol 93 No 3-4 (1993), P307.

[46] S.M Grannan, P.L Richards, M.K Hase: Int. Jrnl. of IR. and mm. Waves, Vol 18 (1997),P319

[47] E.E. Haller: Instrumentation in Astronomy VIII SPIE Proc. 2198 (1994), P630.

[48] E. Auborg, A Cummings, T. Shutt, W. Stockwell,P.D Barnes, A Da Silva, J Emes, E.E Haller,A.E, Lauge, R.R Ross, B. Sadoulet, G. Smith, N. Wang, S. White, B.A. Young, D. Yvon: Jrnl. of Low Temp. Phys. Vol 93 No 3-4 (1993), P289.

[49] K.M. Ioth, W.L. Hansen, J.W. Beeman, E.E. Haller, J.W. Farmer and V.I. Ozhogin: Jrnl. of Low Temp. Phys. Vol 93 No 3-4 (1993), P307.

[50] S.M Grannan, P.L Richards, M.K Hase: Int. Jrnl. of IR. and mm. Waves, Vol 18 (1997),P319

[51] E.E. Haller: Instrumentation in Astronomy VIII SPIE Proc. 2198 (1994), P630.

[52] R.C. Jones ; Jrnl. Optical Soc. of America, Vol 43 No1 (1953), P1

[53] J.C. Mather ; Appl. Optics, Vol 21 No 6 (1984), P1125

[54] M.J. Griffin and W.S Holland: Int. Jrnl. of IR. and mm. Waves, Vol 9 No. 10 (1988),P861

[55] G. Chanin and J. P. Torre: J. Opt. Soc. Am, Vol 1 No4 (1984), P12

[56] T.W. Kenny, P.L. Richards, I.S. Park, E.E. Haller, J.W. Beeman: Phys Rev B Vol 39 No 12 (1989), P8476.

[57] T.F. Rosenbaum, K. Andres and G.A. Thomas: Solid State Comms. Vol 35 (1980), P663.

[58] N. Wang, F.C. Wellstood, B. Sadoulet, E.E. Haller, J. Beeman: Phys Rev B, Vol 41 No6 (1990), P3761.

[59] S.M. Grannan and P.L. Richards: "Proceeds 7th Int Workshop on Low Temp Detectors", Munich Germany, (27 July-2 Aug 1997), P160.

[60] N. Wang: PhD thesis University of California at Berkley (April 1991)

[61] R.N. Bracewell; The Fourier Transform and its Applications 2nd Edtion, McGraw-Hill, ISBN 0-07-066454-4, Chpt 18.

[62] A.B. Carlson; Communication Systems An introduction to Signals and Noise in Electrical Systems, McGraw-Hill, ISBN 0-07-009960-X, Chpt 5.

[63] F.N.H Robinson; Noise and Fluctuations in electronic devices and circuits, Monographs in electrical and electronic engineering, Clarendon press, Oxford 1974, ISBN 0 19 859319 8, chapters 3 and 4.

[64] W.S. Holland, P.R. Ade, M.J. Griffin, I.D. Hepburn , D.G. Vickers, C.R. Cunnningham, P.R. Hastings, W.K. Gear, W.D. Duncan, T.E.C. Baillie, E.E. Haller and J.W. Beeman: Int. Jrnl. of IR. and mm. Waves, Vol 9 No. 10 (1996),P861

[65] H.R. O'Neal and N.E. Phillips: Phys Rev Vol 137 No 3A (1965), P A748.

[66] O.V. Lounasmaa : Experimental principles and methods below 1k, Academic Press Inc. (1974), P280.

[67] C.K. Stahle, R.L. Kelley, D. McCammon, S.H. Moseley and A.E. Szymkowiak Nucl Instr and Meth, Vol A370 (1996), P173.

[68] I.D.Hepburn at Mullard Space Science Laboratory, University College London: (Private communication)

[69] P.A. Bromiley, J.H. Rochford, I.D. Hepburn, A. Smith, W.Duncan, N.Kerley: : "Proceeds 7th Int. Workshop on Low Temp Detectors", Munich Germany, (27 July-2 Aug 1997), P201.

[70] I.D. Hepburn; Adiabatic Demagnetisation Refrigeration in Space , ESA Contract, Final Report April 1996. ESA Purchase Order 153018. (Available from I.D. Hepburn, Mullard Space Science Laboratory.)

[71] E.T. Swarthz and R.O.Pohl: Rev. Mod. Phys. Vol. 61 No.3 (1989), P605.

[72] D.S. Matsumoto, C.L. Reynolds Jr. and A.C Anderson: Phys. Rev. B Vol. 16 No.8 (1977), P3303.

[73] At http://constellation.gsfc.nasa.gov/review/rk/rk.html

[74] I.D. Hepburn at Mullard Space Science Laboratory, University College London: (Private communication)

[75] S.H. Mosely,J C Mather, D. McCammon : Jrnl of Appl Phys,Vol 56, Nos 5 (1984), P1257.

[76] Federick Reif; Fundamentals of Statistical and thermal physics, McGraw Hill 1985, ISBN 0 07 085615-X, page 242.

[77] G. Angloher et al; Nuclear Instruments and Methods in Physics Research Section A: Accelerators, Spectrometers, Detectors and Associated Equipment
Volume 444, Issues 1-2, 7 April 2000, Pages 214-219